POLITECNICO DI MILANO

DEPARTMENT OF ENERGY
Doctoral Program in Energy and Nuclear Science and Technology

Catalytic systems for on board applications with renewable fuels

PhD Candidate: Vittoria Troisi

Supervisor: Prof. Gianpiero Groppi
Tutor: Prof. Gianpiero Groppi
Co-Supervisors: Prof. Alessandra Beretta, Prof. Alessio Frassoldati
The Chair of the Doctoral Program: Prof. Vincenzo Dossena

2023 - XXXV CYCLE

Acknowledgements

नमस्ते (Namasté)

List of publications

- **V. Troisi**, V. Piazza, A. Stagni, A. Beretta, A. Frassoldati and G. Groppi, H_2 from biofuels and carriers: a concerted homo-heterogeneous kinetic model of ethanol partial oxidation and steam reforming on Rh/Al_2O_3, International Journal of Hydrogen Energy, April 2023
- **V. Troisi**, A. Beretta and G. Groppi, Low temperature oxidation of methane over Pd-based catalysts: new insights on the axial evolution of methane consumption rate through the spatially- resolved sampling technique, in preparation.
- **V. Troisi**, A. Mostafa, A. Stagni, A. Beretta, A. Frassoldati, G. Groppi, Distributed hydrogen production via bioethanol autothermal reforming on structured catalysts, in preparation.

Scientific communications

- **V. Troisi**, V. Piazza, A. Mostafa, R. Batista, A. Stagni, A. Frassoldati, G. Groppi, A. Beretta, 12th International Conference on Hydrogen Production, 19th -23rd September 2021, Development of a small-scale biofuel processor: modelling of autothermal ethanol reforming (oral presentation).
- V. Piazza, A. Mostafa, **V. Troisi**, R. Batista, D. Gazzoli, G. Groppi, A. Beretta, 12th International Conference on Hydrogen Production, 19th -23rd September 2021, Ethanol-to-H_2 processes on Rh/Al_2O_3: kinetic study in annular reactor with insight on surface C-formation (oral presentation).
- **V. Troisi**, V. Piazza, A. Mostafa, R. Batista, A. Stagni, A. Frassoldati, G. Groppi, A. Beretta, 43rd Meeting of the Italian Section of the Combustion Institute, 4th-6th October 2021, Development of a small-scale biofuel processor: modelling of autothermal ethanol reforming (oral presentation).
- **V. Troisi**, V. Piazza, A. Mostafa, R. Batista, A. Stagni, A. Frassoldati, G. Groppi, A. Beretta, HYPOTHESIS, 16th Hydrogen Power Theoretical & engineering Solutions International Symposium, 8th -10th November 2021, Development of a small-scale biofuel processor: modelling of autothermal ethanol reforming (poster presentation).
- V. Piazza, A. Mostafa, **V. Troisi**, R. Batista, D. Gazzoli, G. Groppi, A. Beretta, HYPOTHESIS, 16th Hydrogen Power Theoretical & engineering Solutions International Symposium, 8th -10th November 2021, Ethanol-to-H_2 processes on Rh/Al_2O_3: kinetic study in annular reactor with insight on surface C-formation (oral presentation).
- **V. Troisi**, V. Piazza, A. Mostafa, R. Batista, A. Stagni, A. Frassoldati, G. Groppi, A. Beretta, CATENERCHEM winter school, 14th -18th March 2022, Distributed hydrogen production via bioethanol autothermal reforming on structured catalysts (poster presentation).
- **V. Troisi**, G. Groppi, A. Beretta, NAM27, The 27th North American Catalysis Society Meeting, 22th-27th May 2022, Low-temperature oxidation of methane on Pd-based monolith catalysts for efficient ICE emission control (oral presentation).
- **V. Troisi**, V. Piazza, A. Mostafa, R. Batista, A. Stagni, A. Frassoldati, G. Groppi, A. Beretta, NAM27, The 27th North American Catalysis Society Meeting, 22th - 27th May 2022, Distributed hydrogen production via bioethanol autothermal reforming on structured catalysts (poster presentation).

Table of contents

Abstract

The original concept of sustainability can be emphasized integrating social goals with responsible resource management and environmental preservation. Today, sustainability is seen as a driver of innovation, which is crucial for competitiveness in a changing world.

Catalysis has historically helped address environmental challenges, such as control of vehicle emissions. The adoption of sustainable renewable biofuels poses new challenges to the development of efficient catalytic technologies for vehicle emission aftertreatment.

This PhD study focuses on two processes: a Rh-based biofuel processor for hydrogen production and a Pd-based system for reducing emissions from a biomethane engine. The study was carried out combining experimental tests performed in rigs equipped with spatially resolve set up, able to collect axial temperature and concentration profiles within catalytic honeycombs, with mathematical model analysis of the experimental data. Such an approach was adopted to gain insight on the evolution of the reacting systems across the catalyst bed aiming at fully comprehending the reactor behavior and validating the developed models.

On-board production of H_2 from liquid fuels represents a valuable solution to enhance the vehicle energy efficiency and improve the performances of aftertreatment systems. Catalytic partial Oxidation (CPO) on Rh-catalysts is an attractive technology for the on-board H_2 production. Because of the high exothermicity of the process, the reaction can be conveniently carried out in adiabatic reactors of compact size and fast response to variable loads. In view of zero-emission strategies, bio-ethanol represents a promising model fuel as its combustion does not increase the net amount of greenhouse gas emissions.

In this work, a significant step forward has been done towards the development of an engineering tool that can capture all the relevant features of bioethanol CPO over Rh-based catalysts; a combined homo-heterogeneous kinetic scheme is developed and validated against experimental data, informative of the catalytic and thermal activation of the C_2-alcohol.

In particular, a 36-species reduced homogeneous scheme is developed, able to capture observed trends with a limited computational load. On the other side, a macro-kinetic heterogeneous scheme with six molecular reactions (ethanol oxidative dehydrogenation, total oxidation, decomposition, dehydrogenation, steam reforming and acetaldehyde post-reforming) is tuned to accurately describe ethanol/O_2 and ethanol/H_2O reacting systems. The so derived combined homogeneous and heterogenous kinetic scheme is implemented in a mathematical model able to predict the performance of a Rh/Al_2O_3 coated monolith as a catalyst for the CPO. The model is validated against axially-resolved experimental data collected from a lab-scale autothermal reformer. The

results show that the heterogeneous oxidative chemistry activates gas-phase pyrolytic routes with formation of intermediate hydrocarbon species, which are rapidly consumed by surface reactions downstream the hotspot.

To further support the decarbonization efforts in the transportation sector, an experimental investigation is conducted to assess the effectiveness of a commercial Pd-based monolith catalyst in reducing methane emissions. Various feed conditions, representative of natural gas vehicle exhaust, are tested. Concentration and temperature profiles are collected using spatially resolved technique. The experiments are carried out under lambda sweep conditions, examining feeds with both excess and deficient oxygen levels. This innovative approach allows for a detailed examination of the kinetic regimes associated with declining oxygen concentrations across the monolith channel, which can hardly be analyzed using integral reactor data.

To maintain catalyst stability, a protocol is established that periodically shifts to richer compositions for a specified duration, resulting in nearly constant methane conversion downstream.

The bulk of data show that the rate of methane conversion is highly sensitive to the local concentration of O_2 and a critical oxygen concentration exists for each reacting temperature below which the conversion rate changes abruptly and increases by almost one order of magnitude.

1. Introduction

1.1 Background

The research work of this interdisciplinary PhD thesis is in the framework of decarbonisation and sustainable mobility.

Currently, the transport sector is responsible for approximately 25% of global CO_2 emissions: road transport accounts for almost 75% of these emissions and aviation and deep-sea shipping for more than 10% each.

In order to meet the proposed targets of the Paris Agreement, CO_2 emissions from transport will have to be reduced approximately 95% by 2050 compared to 1990 levels [1].

Multiple strategies are available to reduce the end-of-pipe emissions in the mobility sector:

1) lowering the amount of distance travelled per capita (e.g., smart mobility, working from home);

2) increasing the energy efficiency of vehicles and vessels operated under fossil energy carriers;

3) electrification of vehicle power systems;

4) using non-fossil-based fuels for the classical internal combustion engines (ICE): either biofuels or e-fuels.

In a perspective where new cars and vans should be zero-emissions by 2035, since the first two strategies are not sufficient, governments are increasingly prioritizing the goals of enhancing energy efficiency and reducing vehicle-related greenhouse gas (GHG) emissions and air pollution.

Electrifying the transport sector offers substantial environmental benefits and long-term cost savings, but it also presents challenges related to infrastructure, limited battery lifespan, upfront costs, and driving range limitations [2]. This has led the technical and scientific community to actively explore alternatives to petroleum-based fuels, which currently dominate the transportation sector [3].This has led the technical and scientific community to actively explore alternatives to petroleum-based fuels, which currently dominate the transportation sector [3].

In this context, catalysis plays a crucial role in the emission control and the development of advanced strategies of fuel conversion to improve vehicle energy efficiency.

1.2 The role of catalysis in decarbonising transport sector with alternative fuels

The original concept of sustainability emphasized the need to integrate social goals (such as health, quality of life, and employment) with the responsible management of limited resources (such as energy and raw materials) and the preservation of the natural environment. This included actions like adopting cleaner processes, recycling waste, and reducing pollutant emissions to protect biodiversity. Today's understanding of sustainability goes beyond this, recognizing it as a driver for innovation.

In facing rapidly changing socioeconomic and geostrategic conditions, society must adapt and prioritize innovation to remain competitive and economically viable. Catalysis has historically played a significant role in promoting sustainability by improving the feasibility, eco-efficiency, and economics of over 90% of chemical processes.

Moreover, catalysis has been crucial in addressing environmental challenges, such as reducing emissions from vehicles. For instance, catalytic converters introduced in the 1960s helped mitigate the rising levels of pollutants like NO_x, CO, and hydrocarbons from the global expansion of the automotive market. Without these converters, it would have been impossible to reduce NO_x emissions to levels sustainable for society, preventing issues like smog formation, acid rain, and increased health problems due to pollution.

In the last few decades sustainable mobility has been based on constant development of catalytic converters with enhanced performances for various vehicles, including cars, buses, and trucks. Catalysis remains a key factor in addressing new challenges and will play a pivotal role in the evolving landscape of vehicle emissions regulations, including stricter CO_2 limits.

This research work focused on the improvement of the operative efficiency of the aftertreatment section of a vehicle by employing catalytic systems according to two strategies: Rh-based monolithic on board biofuel processor to produce H_2 for the reduction of the catalytic converter or as a feed for auxiliary power unit; and Pd-based monoliths for low-temperature abatement of the exhaust gases coming from a biomethane fuelled engine.

1.2.1 Hydrogen from bioethanol

The growing environmental concerns and the strict regulations regarding vehicle emissions are pushing the automotive sector towards the employment of cleaner fuels. As a matter of fact, a reduction in transport emissions is necessary to meet the climate neutrality targets set by the most recent European policies [4].

Hydrogen has recently emerged as one of the most promising alternatives to decarbonize the mobility sector [5]. The use of hydrogen in fuel cell vehicles (FCVs) has attracted substantial attention and has been introduced recently as a commercial application by several manufacturers [6]. Additionally, several studies have been devoted to exploring methods for improving the performance of internal combustion engines using hydrogen, where blending hydrogen with carbon-based fuels creates a more efficient mix. This process increases the flammable limit and reduces pollutant emissions while also improving the performance of thermal efficiency, power, and torque [7]–[10].

Numerous technologies have been studied for on-board hydrogen storage as reviewed by Hassan et al. [11]. However, an interesting path for the delivery of H_2 to the power unit is the onboard processing of liquid hydrogen carriers, either through steam reforming or catalytic partial oxidation (CPO) [12], [13].

Structured catalysts have been proposed for the application of the small-scale fuel processors and several studies have been conducted using octanes [14], liquified petroleum gas [15], methanol [16], and ethanol [17]. Partial oxidation of ethanol was demonstrated in milliseconds contact time using noble metal catalysts [18]. Among the tested metals tested, Rh was reported to have the highest syngas selectivity and has shown the highest stability.

In previous works at LCCP labs noble metals-based structured catalysts for the small-scale production of hydrogen in a lab-scale adiabatic fuel processor were studied using several hydrocarbons as feed [19]–[22]. Recently this work was extended to include oxygenated components where the CPO and the autothermal reforming of ethanol [23], [24] were tested.

The consolidated role of bioethanol in the transportation sector makes it an interesting choice for stationary and on-board applications, because of its abundant availability from inedible biomass such as energy crops, agricultural or forest waste and residues. A recent study of ethanol CPO and SR on Rh/Al_2O_3 catalyst [25] the combination of catalytic testing, Raman spectroscopy, *operando* FTIR and TPO analyses allowed to reveal the full complexity of this reacting system, composed of multiple reaction pathways; herein H_2 production routes are hindered by the strong adsorption of surface C-species at temperatures below 500°C, but above this threshold surface reactions gain a high temperature sensitivity and H_2 production becomes highly selective.

Previous studies have addressed the development of heterogeneous kinetic schemes of ethanol partial oxidation or steam reforming on noble metal-based catalysts like Rh/Al_2O_3, that are preferred candidates for process intensification and on-board applications due to their higher activity when compared to transition metals; additionally, noble metals have shown a higher resistance to C-deposition, a key property when oxygenates are involved [26]. Vaidya et al. studied

ethanol reforming on a commercial Ru/Al$_2$O$_3$ in a traditional fixed bed reactor over a narrow temperature range (600-700 °C), estimating an apparent activation energy of 96 kJ/mol [27]. Görke and co-authors carried out their investigation on ethanol reforming in a microreactor and were able to extend the temperature window of analysis (350-660 °C) [28]; they used Rh/CeO$_2$, a catalyst characterized by a low acidity that inhibited the onset of coking. Graschinsky et al. showed that the rate-determining step (RDS) of ethanol steam reforming on Rh(1%)MgAl$_2$O$_4$/Al$_2$O$_3$ involves two sites of the same type [29]. Furthermore, it was seen that in the presence of O$_2$ co-feed, oxidation reactions prevail in the inlet part of the reactor and at low temperatures [30]; as a general consequence, the increase in oxygen-to-ethanol ratio in the feed lowers the selectivity to H$_2$ and CO in favour of CO$_2$ [31]. An equivalent behaviour was observed in [32], where a detailed reaction mechanism for ethanol CPO on Pt-Rh supported catalysts is proposed.

Surprisingly, in-depth studies on the effect of C-poisoning on ethanol reaction kinetics remain extremely scarce. Moreover, literature studies do not account for the possible ignition of homogeneous reactions, that can occur in the high temperature range and can compete with catalytic pathways: while studying the CPO of ethanol, Hebben et al. [33] and Diehm et al. [34] found that homogenous gas phase reactions result in the formation of by-products, namely acetaldehyde, methane, and ethylene.

Several detailed homogenous kinetic mechanisms are available in literature. Nowadays, it is recognized that the information contained in detailed chemistry is necessary to guarantee the accuracy of large-scale simulations [35]. Yet, it is often not applicable "as such" in multidimensional simulation tools due to the number of species to be transported. Most of the CPU time in the integration of the ordinary differential equations (ODEs) describing a reacting system is spent in the factorization of the associated Jacobian matrix [36]: the time complexity of this step scales with n^p, with n being the number of equations, and $p = 3$ for several adopted algorithms [37]. For this reason, mechanism reduction is a suitable approach to facilitate practical simulations using realistic chemistry with modern computational tools, as it reduces the number of species to be transported, thus the resulting size of the Jacobian.

1.2.2 Emission abatement from biomethane fuelled vehicles

The obvious solution for the decarbonization of the energy sector is an extensive electrification of the passenger cars and light duty vehicles. However, the transformation requires time, and electrifying heavy duty transport - notwithstanding current discussions on overhead wiring

highways- is not an easy task. In contrast, biofuels could share the existing distributing infrastructure with little modification [38].

Among biofuels, biomethane, or upgraded biogas, is currently emerging as one viable solution for the heavy-duty transport sector, trucks, buses as well as marine transport [3]. It has the same advantages as natural gas (lower emissions of particulate matter, NO_x and SO_x) - being its main component -, but it is more friendly for the environment from a sustainable point of view. In fact, it is characterized by higher reduction of GHG emissions and positive contribution to waste management [39]. Several European projects (GasHighWay [40], Biogasmax [41], Biomaster, etc.) have showed that biomethane produced and used locally has a positive impact on local sustainable development (reduction of negative issues linked to transport sector like smog, creation of new markets, generation of news jobs, etc.). Nevertheless, the presence of unburnt methane in the exhaust is a concern due to its global warming potential (28 times higher than CO_2 over a period of 100 years) [42].

Stoichiometric combustion systems are commonly used in natural gas (NG) vehicles; they include a three-way catalyst (TWC) [43] where palladium is mainly added, being the most active noble metal for CH_4 oxidation [43]–[46]. In lean conditions methane exhibits low conversion also due to high water concentration in the exhausts, which exerts a strong inhibition effect [47], [48]. Instead, high abatement performance is obtained by dithering lambda conditions [49]. The complex surface chemistry behind this behaviour is still under discussion. Indeed, several studies have addressed the activity of metallic palladium and palladium oxide as active sites for methane oxidation [50], [51]. It has been found that the mixed Pd-PdO species (PdO_x) are more active than PdO [52], [53], and that cyclic lean/rich O_2 pulses would be responsible for the sustained formation of active Pd species [45], [54], [55].

Many studies have focused on the impact of lambda, dithering amplitudes and frequency [46], [49], [54], [56]. Among them, Bounechada et al. [56] addressed a systematic study of the oscillating operation of the catalyst bed and has identified optimal values of lambda.

A major challenge for the application of Pd-based catalysts is related to their sensitivity to water vapor, which constitutes around 10 - 15 % of the exhaust gases from NG vehicles [57]: water tends to create stable surface hydroxides which inhibit the active sites by shifting the activity towards higher temperatures [58], [59]. Two water deactivation routes have been distinguished: blockage of active PdO sites [60] and decreased surface oxygen mobility resulting in less Pd re-oxidation and consequently less PdO sites [61], [62]. Which still relates to the importance of the surface balance between metal and oxidized sites.

The great majority of the application-oriented studies have been based on the integral approach, where conversion measurements are obtained from the outlet product composition and are thus the result of the evolution of temperature and gas composition along the monolith. Integral data are extremely useful for the assessment of the catalyst performance under relevant conditions; however, given the high sensitivity of the surface to the axially evolving gas-phase conditions, they cannot provide fundamental understanding of the process kinetics. In this respect, the possibility to combine experiments at the monolith scale (providing the overall converter performance) with a detailed monitoring of temperature and composition across the reactor offers in principle an important advancement of the experimental investigation. This objective can be pursued by the application of the spatially-resolved sampling technique, where sliding probes enable the measurement of axial concentration and temperature profiles under working conditions, ultimately providing the tools for estimating how the reaction rate evolves from the inlet to the outlet of the monolith [63].

1.3 Objectives of the thesis work

This research work focuses on the improvement of the operative efficiency of the aftertreatment section of a vehicle by investigating two strategies:

a) The development of a small-scale biofuel processor through the modelling of an autothermal ethanol reforming. Catalytic partial oxidation (CPO) technology is suitable to small-scale processes such as fuel processors for stationary applications (fuel cells or combined heat and power systems), and on-board syngas generators serving a variety of uses such as H_2 injection in the combustion chamber or fuelling of Auxiliary Power Units. Noble metal-based catalysts like Rh/Al_2O_3 represent the best candidates for process intensification and on-board applications that must be operated at high space velocities: by assuming a gas hourly space velocity of 50000 Nl/h/kg$_{cat}$, a cost of Rhodium of 396 €/g and a cost of bioethanol of 2 €/l, the high cost of Rhodium catalyst for a fuel processor is expected to be equalized by bioethanol operating costs in less than one week. Moreover, the higher resistance to C-deposition justifies the choice of Rh-based catalyst with respect to transition metals like Nickel.

Many researchers have been focused on the study of the mechanism and reaction pathways of ethanol activation on metal catalysts, but the development of a mathematical tool able to model the kinetics evolution is still less advanced.

Starting from this background, the main objective of this work is to develop both a reduced homogeneous and a lumped heterogeneous kinetic scheme of the ethanol conversion routes on Rh, thus setting the engineering tools necessary for the design of catalytic reactors and the development of ethanol-to-H_2 technologies.

The newly developed combined homogeneous and heterogenous kinetic scheme will be implemented in an existing model able to simulate the performance of a Rh/Al_2O_3 coated monolith as a catalyst for the CPO and the autothermal reforming of ethanol. The model be used to analyse experimental spatially resolved temperature and concentration profiles collected using a lab-scale adiabatic rig present in the LCCP labs, aiming at gain insight on the complex behaviour of ethanol autothermal reforming;

b) The low-temperature oxidation kinetic study of methane on Pd-based monolith catalysts for efficient ICE emission control. Methane molecule is highly stable and it is recognized as the most refractory hydrocarbon to oxidation. Due to its high GWP, uncontrolled emissions may outweight the environmental benefits of biomethane fuel.

It is widely accepted that the oxidation state of palladium - the most common noble metal used as active component of the catalyst - plays a major role on methane oxidation activity. However, there are limited studies about the CH_4 oxidation mechanism and kinetics on Pd-based TWCs: the active sites of the catalysts (metallic Pd, PdO or a mixed Pd/PdO) are still under debate [46].

In this work, the axially resolved sampling technique was applied to gain a deeper insight of the complex kinetics of CH_4 oxidation over Pd, looking for correlations between outlet performances and the kinetic phenomena occurring within the channel. At this scope a wide range of conditions was explored with focus on temperature and O_2 feed content, after the results of our previous investigations with respect to a peculiar trend of methane conversion as a function of the feed oxygen content: in the lean region it decreased when approaching the stoichiometric lambda, then a steep increase was observed as the rich window was entered and finally it decreased again towards even lower feed oxygen concentrations [64].

In the following chapters the investigation methods and the results obtained in this thesis work are described in detail. Specifically in Chapter 2 the adopted experimental and theoretical methods are reported and discussed in the framework of the current literature. In Chapter 3 the derivation of kinetic scheme (gas phase and catalytic) for the ethanol CPO over a Rh based catalyst is reported. Chapter 4 focuses on the results of the analysis of experimental spatially resolved profiles collected in an adiabatic catalytic rig by means of a mathematical model implementing the kinetic schemes

developed in Chapter 3. Chapter 5 reports on an experimental investigation on CH_4 oxidation over a Pd based commercial honeycomb.

2. Methods

2.1 The kinetic investigation of catalytic reactions in fixed bed reactors and the evolution of spatially-resolved techniques

Measurements play a crucial and pivotal role in comprehending, developing, optimizing, and modeling catalytic processes. Advanced techniques that can measure the spatial and temporal distribution of reactions within a catalyst under realistic operating conditions offer significant advantages over conventional integral measurements, making considerable advancements in catalysis research.

To achieve optimal advancements in gas-phase heterogeneously catalyzed continuous processes, a profound understanding of the kinetics of surface reactions is crucial, particularly when dealing with complex reactant mixtures. The conventional test involves loading the catalyst into a controlled reactor with regulated pressure and temperature, allowing the reaction gas mixture to flow through the reactor. Figure 2.1 illustrates a common setup where reactants are introduced into the reactor, flowing through the catalyst bed where the reaction takes place, and then the reactor effluent downstream of the catalyst bed is analyzed. The only available data pertains to the concentration difference between the known inlet and the measured outlet [65].
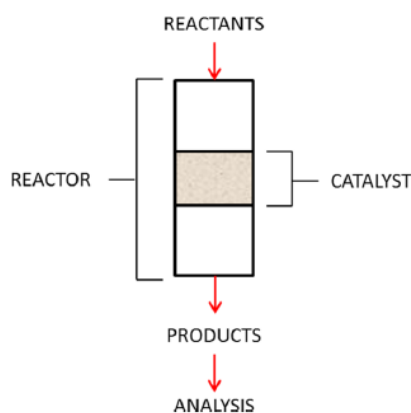

Figure 2.1 End-pipe sampling operates based on the following principle: the concentrations of reactants are established, and once products are formed, they exit the reactor.

This analysis method, commonly known as integral, "tail pipe end," or "catalyst effluent" analysis, has been widely utilized in the majority of experimental kinetic studies. It involves using tail-pipe-end/catalyst-effluent techniques such as gas chromatography (GC), Fourier Transform Infrared (FTIR) spectroscopy or mass spectrometry (MS), which employ a probe positioned at the downstream end of the reactor (after the catalyst bed) to sample the gases exiting the system. The reactants are introduced into the reactor, passing through the catalyst bed where the reaction takes place, and are then analyzed in the effluent flow downstream of the catalyst bed. In order to gather data about kinetics, the reaction conditions, including reactor temperature, pressure, space velocity, and feed composition, are varied. This allows for the observation of catalyst performance based on measurements taken at the end of the process.

In plug flow reactors, two scenarios arise:

1. Differential conditions (i.e., low conversions) assume a uniform environment across the catalyst bed, allowing for reaction rate calculation from activity data. Nevertheless, these conditions do not represent the real industrial operations, and the differential conditions only represent a narrow range of the interplay between environment and structure, ending up in a limited applicability of the relations deduced beyond this analytical range;

2. Integral conditions (i.e., high conversions) involve significant reactant and product concentration changes between reactor inlet and outlet, impacting data interpretation. Without intra-catalyst spatially resolved characterization, relating structural data to activity/selectivity is challenging.

However, these methods only provide information about the difference in concentration between the known inlet and the measured outlet. In end-pipe sampling analytical methods, the catalyst bed is regarded as a "black box" since the techniques do not directly access the chemical interaction between the reactants and the catalyst occurring within the catalyst bed. Under integral conditions this gap can be covered only by a suitable reactor model which will provide the computed trends of concentration and temperature profiles throughout the reactor; however, when complex reacting systems are involved, direct pieces of evidence on the evolution of the reacting systems across the catalyst bed would be extremely useful for fully comprehending the reactor behavior and validating the developed models.

In recent years, *operando* characterization techniques, such as XRD (X-ray diffraction), XAFS (….), Raman and diffuse reflectance infrared fourier transform spectroscopy (DRIFTS) have been developed to collect more information about the state of the catalyst active sites and adsorbed

species under working conditions, whose populations evolve with evolving conditions of the gas-phase.

More relevant to the characterization of the evolving gas-phase composition are the techniques that different research groups have developed for spatially resolving the chemical species concentration and temperature distributions within a reactor during the operation of an integral reactor. These techniques aim to gain detailed insights into phenomena occurring on the catalyst surface and inside the catalytic reactor under operando conditions.

A first attempt to collect temperature profiles during dynamic experiments was made in 1985 by Baiker et al. [66]: a fixed-bed pilot reactor was equipped with a network of thermocouples and IR analyzer probes were used to measure the temperatures. However, limitations lied to the invasiveness of the probes and to the low spatial resolution, characterized by a probe every 10 cm.

Advancements have been made since then to improve spatial and temporal resolution and reduce the invasiveness of physical probes. New and improved equipment, along with more accurate and powerful techniques, now allow for spatially resolved profiles of gas concentrations and temperatures, especially within structured catalyst beds. These improvements have contributed to advancing catalysis research and knowledge, crucial for designing reactors and optimizing operating conditions.

In the late 1990s, Partridge et al. [67] at Oak Ridge National Laboratory (ORNL) developed the spatially resolved capillary-inlet mass spectrometer (Spaci-MS) technique in collaboration with Currier et al. [68] at Cummins Inc. Although the technique has been extended and developed for broader research purposes, such as engines, fuel cells, and catalytic partial oxidation (CPO) of methane and propane, its primary emphasis remains on comprehending the network and sequence of reactions taking place within fully formulated and model-formulation automotive catalysts coated on honeycomb monoliths. It allowed for quantitative and high temporal response measurements under operando conditions using real engine exhaust. The Spaci-MS approach was minimally invasive, utilizing a thin fused silica capillary to sample small quantities to a fast time response mass spectrometer for analysis.

The Spaci-MS technique was further improved to obtain simultaneous spatially and temporally resolved information by allowing movement of the capillary within the catalyst monolith. This provided spatial resolution along the full length of the catalyst bed. The technique has been used in various applications, including studying $Pt/K/Al_2O_3$-based catalysts, lean NO_x Trap (LNT) catalytic monoliths, and N_2O formation.

Further developments by ORNL and Queen's University Belfast (QUB) incorporated an automated multiport valve and translation system with a network of capillaries and thermocouples. This

second-generation Spaci-MS allowed for automated axial and radial mapping of composition and temperature throughout a catalyst monolith.

Additionally, an imaging technique based on infrared thermography was designed by Epling and coworkers [69] to spatially and temporally resolve temperatures within a catalytic monolith. This noninvasive technique allowed for the measurement of monolith surface temperature using an IR camera. It was later combined with Spaci-MS functionalities to add spatial resolution of gas composition within the monolith.

Overall, these advancements in spatially resolved analytics have significantly contributed to understanding complex reactions and phenomena occurring within catalysts under various operating conditions.

The Spaci-type measurements have been widely used in various applications, including studying reforming and oxidation catalysts. For example, Bugosh et al. [63] conducted a Spaci-MS study to investigate methane oxidation over a $Pt/Pd/Al_2O_3$ catalytic monolith. The results revealed that complete methane oxidation can occur in both lean and rich conditions, with distinct zones of oxidative and partial oxidation/reforming reactions.

Similar techniques have been employed to study the CPO of methane using Pd/Al_2O_3 and Rh/Al_2O_3-coated monoliths. The findings indicated differences in the effectiveness of Pd and Rh for reforming reactions and the mechanisms involved in syngas formation [70].

Additionally, at first Lanny Schmidt at University of Minnesota and then Horn et al. at the Fritz-Haber Institute, developed a Spaci-like approach to obtain gas concentration and temperature profiles from fixed catalyst beds. This technique has been utilized to study drilled foam catalysts and investigate various catalytic reactions, including methane CPO and oxidative dehydrogenation of ethane to ethylene [71].

Schmidt, Horn, and co-workers [72] have significantly contributed to the development of spatially resolved techniques for characterizing catalyst supported on foam monoliths and bead beds; in the bead-bed applications, the support-bead OD (1 mm) was similar to that of the sampling capillary (0.70 mm). In these applications, the sampling probe was not considered to be invasive due to the strong radial mixing in foam-monolith and bead-bed catalysts.

The recent improvements in this technique include the collection of spectroscopic data from the catalyst surface using Raman optical fiber probes, allowing for simultaneous gas composition and surface C-accumulation measurements.

These spatially resolved techniques have significantly contributed to understand catalytic reactions and mechanisms in different catalyst systems, particularly those supported on foam monoliths and

bead beds. However, their applicability is limited to specific catalyst configurations, and they may not be well-suited for powder-catalyst applications due to their invasive nature.

Donazzi et al. [22] developed a technique for spatially resolved surface temperature measurements within structured catalysts like honeycombs and drilled foams. The method uses a side-looking optical fiber connected to a pyrometer to measure wall temperature distributions within a honeycomb catalyst. The technique is noninvasive for honeycomb-monolith applications and does not resolve gas composition profiles within the monolith. The invasiveness of the sampling capillaries within catalytic monolith channels was investigated using computational fluid dynamics (CFD) by Sà et al. [73]. The study employed a 3D fluid flow and mass transfer model, comparing cases with and without a probe capillary. It was deduced that with a cross sectional area of the capillary probes equal to 4.9% of the channel - under the investigated conditions - a negligible invasiveness in terms of flow and mass transfer was detected. The research highlighted the influence of catalyst, reactor and probe characteristics on the invasiveness of spatially resolved intra-catalyst measurements. Smaller probe diameters and sampling rates were recommended for higher monolith densities and space velocities to achieve less invasive measurements. The findings were later challenged by Deutschmann and co-workers [74], who argued that the probes were more invasive due to discrepancies in boundary conditions and differences in flow rates. However, a critical analysis of the comparison showed that practical configurations were not considered in the worst-case scenarios presented by Deutschmann's team. The placement of the capillary within the channel was in fact influenced by gravity, and alternative configurations showed reduced probe impact.

Hettel et al. [75] investigated the impact of the capillary positioning, both axial and radial, inside the catalyst channel. It was shown that, regarding the radial coordinate, the probe influences more the flow field when situated in the centre of the channel. Concerning the axial position, the influence of the sampling grows with the probe length inserted into the monolith. This is because the capillary tends to introduce a pressure drop: as a result, in the individual catalyst channel, flux reduces, and residence time is increased.

Choi et al. [76] applied phosphor thermography to resolve spatiotemporal transient temperature distributions within an operating honeycomb-monolith-supported catalyst. This technique is based on the temperature-dependent excited-state lifetime of a phosphor transducing material and provides accurate temperature measurements with low thermal conductivity and high sensitivity.

Optical fiber techniques, such as fiber Bragg gratings (FBG) and optical frequency domain reflectometry (OFDR), allow for directly resolving temperature distributions along the fiber's length. These methods use spectral analysis of backscattered light to provide multipoint or

continuously distributed temperature measurements. OFDR has shown potential for transient distributed temperature studies in catalyst systems.

In this thesis work, spatially resolved technique has been adopted along the lines of Donazzi et al. [22] to predict products distribution in autothermal reformer of ethanol on Rhodium catalysts and gain new insights on methane oxidation on a commercial Pd-based catalyst in a wide range of feed conditions.

The experimental set up adopted in this thesis work -schematized in Figure 2.2 - is equipped with a linear stage actuator (Zaber® T-LA) allowing to collect spatially resolved concentration and temperature profiles by displacement of deactivated fused silica capillaries in a central channel along the axis of the monolith. A first capillary (ID 530 μm, OD 670 μm) sealed at one end was used to host a K-type thermocouple or an optical fiber connected to a narrow-band infrared pyrometer. The optical fiber, whose tip is 45° ground, measures catalyst temperature, while the gas-phase temperature is measured through the thermocouple. Another capillary (ID 200 μm, OD 360 μm) opened at its tip allows to withdraw and analyze gas samples through the measurements of a microGC.
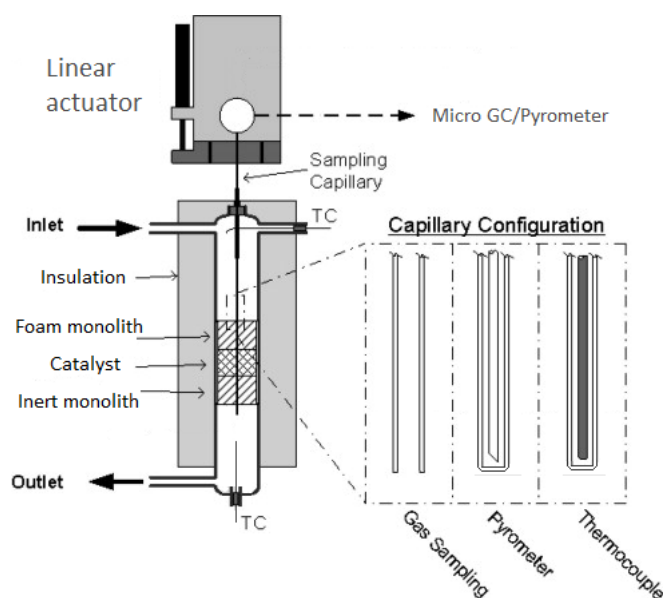

Figure 2.2 Schematic representation of the system for resolving species and temperature distributions within a monolith catalyst showing the location of the different elements of the system.

The invasiveness of the probe was accurately monitored by comparing experimental profiles of the species with calculated data obtained through a modeling tool in mass transfer regime.

2.2 Lab scale reactors applied in the kinetic investigations

In this work, different reactor configurations have been adopted in order to meet the proposed targets.

In view of a dedicated modelling analysis for the optimization of H_2 production from ethanol in an autothermal reformer, a kinetic study of ethanol CPO was performed in an annular integral micro-reactor, then the process was studied in more realistic operative conditions an adiabatic lab-scale reformer where the axially resolved sampling technique allowed to follow the evolution of the by-products with respect to the temperature.

Besides, in order to contribute to the active debate about CH_4 oxidation mechanism on supported Pd, this work exploits the axially resolved sampling technique to provide a more detailed focus in an isothermal reactor, under a wide range of feed conditions.

2.2.1 Annular micro-reactor for the development of a complete ethanol - CPO scheme

The Rh/α-Al2O3 ethanol catalytic partial oxidation (CPO) kinetics was investigated using a structured reactor with an annular configuration [77]–[80]. Previous studies [81]–[83] have demonstrated that the annular reactor is a versatile tool for studying fast reactions, such as the CPO of natural gas and light hydrocarbons.

The reactor consists of a quartz cylinder tube with 5 mm O.D. – schematized in Figure 2.3 - in which catalyst-coated alumina tubes or bare tubes can be inserted. Details about this annular microreactor configuration are given elsewhere [77]–[80].

Figure 2.3 Scheme of the quartz reactor.

In this way, annular flow can be obtained in the reactor, and this guarantees different benefits compared to traditional packed bed reactors:

• less diffusive limitations both intra-phasic (the catalytic layer is thin) and inter-phasic (the thickness of the annular section is reduced to about 0.5 mm);

• the possibility to use higher spatial velocities, or Gas Hourly Space Velocity (GHSV), and studying fast reactions limited by equilibrium;

• possibility to measure directly the temperature of the catalytic layer since it is very thin, and it is possible to consider it in thermal equilibrium with the alumina tube;

• high capacity for heat dissipation by irradiation combined with the high dilution in nitrogen (90-95% N_2) with the advantage of the possibility to conduct experiments that allows limited axial temperature gradients; the reactor can be considered substantially isothermal.

A tubular Carbolite oven was used to heat the quartz reactor at the desired temperature.

Gases (Air, N_2, H_2) were fed with mass flow controllers (Brooks), while a saturator with bubbling N_2 was used to feed ethanol. For experiments with H_2O co-feed, water was instead synthesized in an upstream Pt/Al_2O_3 reactor, by sending a diluted mixture of H_2 (in 5% v/v excess) and stoichiometric O_2. Composition measurements of inlet and outlet mixtures were carried out in an online micro-GC (Agilent Technologies, 3000 A), provided with two capillary columns (Molecular Sieve for H_2-O_2-N_2-CH_4-CO, PoraPlotU for CO_2-ethylene-H_2O-acetaldehyde-ethanol) and TCD detectors.

In this work, catalytic experiments were carried out by inserting the catalyst-coated alumina tubes into the quartz reactor, whereas homogeneous experiments were performed by using bare tubes.

Catalytic experiments were performed on 2 wt% Rh/α-Al_2O_3 catalysts, which were prepared following a procedure developed in previous works [81]–[83]. α-Al_2O_3 powders were obtained by calcining commercial γ-Al_2O_3 (SASOL PURALOX SCFa 140 or SBa 200) in air at 1100 °C for 10 h. Rhodium was added via incipient wetness impregnation, using an aqueous solution of $Rh(NO_3)_3$ and then catalytic powders were dried in oven at 120 °C for 3h. Superficial area of 8 m^2/g and pore volume of 0.21 cm^3/g were measured via BET (TriStar Micrometrics 3000) and Hg-porosimetry (MicroActive AutoPore V), while ICP-MS (X Series II by Thermo Fisher) and H_2-chemisorption (ThermoQuest TPD/R/O1100) analyses revealed a real Rh load on the support of 2.3 wt% and 30% dispersion, respectively. Previous XRD and FESEM studies exhibit the presence of Rh nanoparticles dispersed on Al_2O_3 with a diameter in the range of 2-25 nm [25]; further analyses on spent catalytic samples also confirm that these Rh particles are not subjected to sintering in the explored operating conditions.

A slurry was then prepared by dispersing catalytic Rh/α-Al_2O_3 powders in an acidic solution (HNO_3/powder = 1.7 mmol/g, H_2O/powder = 1.4 mL/g) and by a 24h-milling treatment, where

zirconia balls were used [80]. For testing in annular reactor, this slurry was deposited through a dip-coating procedure around dense-alumina tubular supports (O.D. 3.96 mm, 35.5 cm length), in the form of micrometric-thin layers. These alumina tubes present an inner cavity (I.D. 1.98 mm) for the insertion of a thermocouple. Washcoated tubes were subjected to a flash drying in air at 280 °C for 10 minutes.

Catalytic layers with different lengths (2-6 cm) and washcoat mass (15-60 mg) were prepared and tested for the present work. Before catalyst deposition, a boehmite primer was deposited on the tubular supports to enhance the adherence of the support.

Each Rh/Al_2O_3 coated tube was subjected to a conditioning procedure before ethanol experiments, aiming to lead the catalyst to a stable behaviour. The conditioning procedure, consisting of repeated tests of CH_4 CPO, has been described in a previous study [82].

All the ethanol experiments were run at atmospheric pressure between 150 and 800 °C, following a stepwise temperature increase (maximum 50 °C). At each temperature, three composition measurements were collected and averaged: moreover, temperature axial profiles were measured by sliding a K-thermocouple inside the inner cavity of alumina tubes, and the average temperature of the catalytic bed was estimated. To illustrate the results in the present work, composition measurements in terms of reactants conversion and products molar fractions are plotted against the average catalyst temperature.

Ethanol CPO experiments were run with inlet ethanol concentration of 1.5% and O_2 concentration of 1.68%, while using N_2 to balance and varying GHSV between 5·105 and 9·105 $NL/kg_{cat}/h$. Ethanol SR tests were carried out at 0.9-1.5·106 $NL/kg_{cat}/h$, feeding 1.5% ethanol and 3% H_2O. Similarly, homogeneous ethanol oxidation tests were run with 1%-1.5% ethanol and 0 or 1.68% O_2, respectively; the total inlet flowrate was varied in an interval (225-1354 NmL/min) corresponding to the range of flowrate investigated in catalytic experiments.

Experiments involving CPO and steam reforming were conducted across a wide range of temperatures, space velocities, and feed compositions. The kinetic parameters were determined by fitting the experimental data using a one-dimensional mathematical model of the annular reactor.

Gas-phase experiments under similar feed and flow conditions were also performed by replacing the catalytic tubes with inert tubes; experiments were performed to tune and validate the homogeneous kinetic scheme of ethanol oxidation, as described in Chapter 3.

2.2.2 Adiabatic lab-scale reformer for ethanol - CPO testing and model validation

Catalytic partial oxidation of ethanol was studied on $Rh/\alpha\text{-}Al_2O_3$ catalysts deposited on honeycomb cordierite monoliths in a laboratory scale reactor allowing to work in adiabatic conditions and gather data to validate the simulation tool.

Starting with a commercial $\gamma\text{-}Al_2O_3$, 2% $Rh/\alpha\text{-}Al_2O_3$ powders were prepared through calcination at 1100 °C for 10 hours with a heating rate of 1 °C/min and a cooling rate of 2 °C/min. This thermal treatment resulted in a BET surface area of 8 m^2/g and a porous volume (Hg porosimetry) of 0.21 mL/g.

Then Rh was added via incipient wetness impregnation technique using a $Rh(NO_3)_3$ solution (Chempur, 15.11 % wt. Rh). After impregnation, the powders were dried overnight at 110 °C. For the preparation of the slurry, the impregnated powders were mixed in a PTFE jar with H_2O, HNO_3 as dispersant and zirconia balls and the system was ball-milled for 24 h at constant rotational speed of 60 rpm. The amounts of H_2O and HNO_3 per mass of catalyst powder were equal to 1.4 mmol HNO_3/g_{powder} and 1.7 mL H_2O/g_{powder}. At the end of the ball-milling, a homogeneous and stable suspension was obtained.

In this work, catalytic monoliths were prepared using cordierite ($2MgO\cdot2Al_2O_3\cdot5SiO_2$) 400/7 honeycomb monoliths cut in the shape of cylinders with 1-inch diameter and about 4 cm length; the monoliths were dipped into the slurry, then removed, and the remaining excess of the latter was blown away with compressed air (p =7 bar). The monoliths were finally flash-dried in an oven at 280 °C for 20 s. A certain length of the monolith was left uncoated, acting as a back heat shield (BHS). The same arrangement was used elsewhere [24].

Details about the tested monolith are given in Table 2.1.

Table 2.1 Catalyst properties

Monolith	L_{CAT} [cm]	L_{BHS} [cm]	m_{cat} [g]	ρ_{cat} [g/cm^3]	ε [-]
NE6	2.2	2.1	1.29	1.38	0.653

The layout of the reactor, represented in Figure 2.4, includes a quartz tube hosting a honeycomb catalytic monolith, aside from an upstream FeCrAlloy foam and a downstream uncoated honeycomb monolith, acting respectively as a flow pre-mixer and thermal radiation shield. The quartz pipe (ID =1 inch, length =12 cm) is then loaded in an AISI 316 L stainless steel tube, thus

protecting flowing gases from contact with the metallic shell; the thermal insulation is achieved by wrapping the reactor with a thick layer of quartz wool.
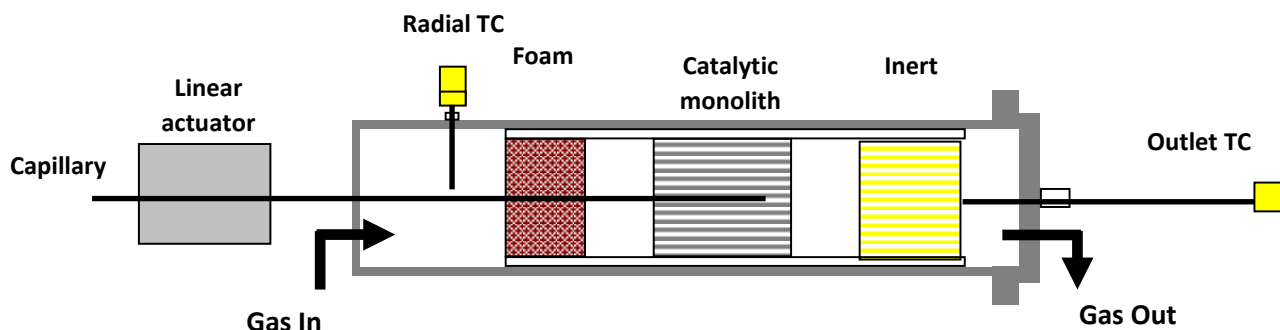

Figure 2.4 Quartz tube reactor assembly.

It is possible to evaluate the thermal efficiency β as an indication for the extent of adiabatic operation of the reactor as follows:

$$\beta = \frac{T_{exp}^{out} - T_{exp}^{in}}{T_{ad}^{out} + T_{exp}^{in}} \qquad (2.1)$$

with T_{exp}^{in} the temperature measured by a thermocouple located at the inlet of the reactor, T_{exp}^{out} the temperature measured by a thermocouple at the outlet of the catalytic channel and T_{ad}^{out} the adiabatic temperature calculated with the inlet composition, inlet temperature, and the outlet composition.

The thermal efficiency measured in this work was always higher than 0.98.

The experimental set up was equipped with the previously described linear stage actuator (Zaber® T-LA) allowing to collect spatially resolved concentration and temperature profiles by displacement of deactivated fused silica capillaries in a central channel along the axis of the monolith. Gas samples were analysed through the measurements of a microGC (Inficon), equipped with two columns: Rt®-Molsieve 5A, which uses argon as carrier gas, and Rt®-Q-Bond which uses helium.

At each axial position, three samples were analyzed, and the mass balances - evaluated on atom basis for carbon, oxygen, and hydrogen - typically closed between 0.95 and 1.05. Since oxygen consumption is assumed to be governed by mass transfer limitations [84], a comparison of its experimental profile with calculated trends proved the reliability of the sampling technique.

All the CPO experiments were carried out at atmospheric pressure, with 10 NL/min flow rate and C/O ratio of 0.65.

The reactor was fed with a mixture of ethanol, air and nitrogen to balance. Ethanol - or a mixture ethanol/water - was delivered by a Gilson Minipuls 3 peristaltic pump to a temperature-controlled evaporator, where it was mixed with an inert gas flow.

To ignite the process in the absence of a heating source, the procedure adopted in previous works was followed [24]: the reactor is preheated with hydrogen (6%) and oxygen (3%) and nitrogen to balance, with a flow rate of 5 Nl/min. Then, the feed mixture is switched to ethanol/oxygen/ nitrogen. Results were collected at steady state, at least 30 min after feeding the CPO mixture.

2.2.3 Isothermal catalytic converter for the abatement of methane emissions

Methane oxidation was studied in isothermal conditions in a stainless steel reactor (L = 38.5 cm, I.D. = 1.63 cm) positioned centrally inside a 30 cm tube Carbolite furnace. The reactor was used to house a 39 mm long monolithic sample, and the monolith was wrapped by a quartz wool tape then located in an ad-hoc designed holder able to host square shaped honeycomb samples with a defined number of channels and to avoid by-pass phenomena, as showed in Figure 2.5.

Figure 2.5 6x6 channel monolith placed in holder.

A FeCralloy foam of 2 cm was placed upstream the catalyst in order to promote the reactant mixing. A 400 CPSI inert cordierite monolith of 1.6 cm length was located upstream before the catalyst to act as a guide for the probing capillary. A schematic representation of the reactor configuration is reported in Figure 2.6.
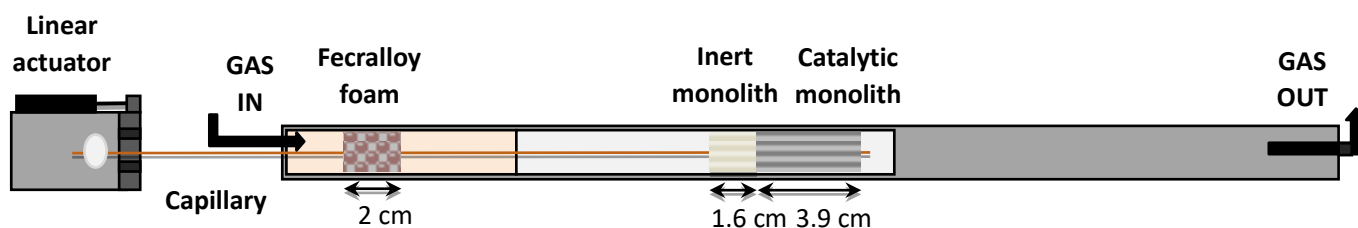

Figure 2.6 Stainless steel reactor loading configuration.

A commercial Pd-Rh based catalyst was used in this study in the form of a 400 CPSI/6 mils washcoated ceramic honeycomb containing 7.1 g/l of Pd:Rh (39:1 of loading) [24]. The washcoat material content referred to the geometric area of the catalyst was 50 g/m^2 and consisted of stabilized Al_2O_3. Ce –Zr mixed oxide (Zr/Ce = 3.5) are also present to improve the oxygen storage capacity (OSC) of the catalyst and transition metal compounds were used as stabilizers and promoters.

The test facility for reaction experiments consists of 4 lines for the individual feeding of a multicomponent mixture (composed of 3 vol.% CH_4, 12 vol.% CO, 2 vol.% H_2 in N_2), air, carbon dioxide and nitrogen. Gases are fed through programmable mass flow controllers.

Furthermore, a Gilson piston pump/evaporator system is used to feed H2O. Water concentration is continuously monitored by means of a humidity sensor (Vaisala HUMICAPP – HMT334).

The micro-GC is equipped by TCD detectors, a Molecular Sieve 5 Å column for separation of N_2, H_2, O_2, CH_4 and CO (Ar carrier) and a Plot Q column for separation of CO_2 and H_2O.

The experimental set up was equipped with the previously described linear stage actuator (Zaber® T-LA) allowing to collect spatially resolved concentration and temperature profiles by displacement of deactivated fused silica capillaries in a central channel along the axis of the monolith. Three samples were analysed for each axial position, and the mass balances typically closed between 0.95 and 1.05. Being three minutes the duration of one analysis, the total time required for the acquisition of the entire concentration profile was around 6 hours. A mass spectrometer, Balzer QMS 200 model, was also used to analyse dynamically the composition of outlet gases.

Experiments were accomplished in lambda sweep conditions, where lambda is defined as the ratio between the actual air flow rate and the theoretical one required by the stoichiometry for complete fuel oxidation in the engine, according to the following expression (2) derived from stoichiometric mass balances on a natural gas engine [85]:

$$\lambda = \frac{y_{O_2,air}}{2} \cdot \frac{4 \cdot y_{CH_4} + 3 \cdot y_{CO} + 3 \cdot y_{H_2} - 2 \cdot y_{O_2} - 4}{(y_{CO} + y_{H_2} - 2) \cdot y_{O_2,air} + (2 \cdot y_{O_2} - y_{CO} - y_{H_2} - 4 \cdot y_{CH_4})} \quad (2.2)$$

with λ = equivalence ratio [–]; y_i = i-species molar fraction at the ICE outlet (i.e. catalytic converter inlet) [-].

When $\lambda < 1$, the feed is rich, whereas when $\lambda > 1$ lean conditions are attained.

The effect of lambda was investigated solely by varying O_2 concentration with N_2 to balance, while the remaining inlet gas mixture - representative of the typical exhausts composition from stoichiometric CNG [86] (0.15 vol.% CH_4, 0.6 vol.% CO, 0.1 vol.% H_2, 10 vol.% H_2O, 10.7 vol.%

CO$_2$) - was fixed. After mixing of the individual gas streams with steam, immediately upstream the reaction section, the lambda value is monitored by an ETAS LA4-4.9 Lambda Meter.

Moreover, the effect of water was studied by varying its content between 2 and 10 %. The gas hourly space velocity (GHSV) was kept constant at 50000 h^{-1} referred to the honeycomb volume.

2.3 Mathematical methods: modelling of ethanol-CPO in isothermal micro-reactor and in adiabatic reactor

A one-dimensional, heterogeneous model was adopted at first to derive a macro-kinetic heterogeneous model through fitting of experimental data collected in an annular reactor as described elsewhere [87], then to simulate the performances of a Rh/Al$_2$O$_3$ coated monolith as a catalyst for the CPO and the autothermal reforming of ethanol.

The mathematical model was developed in a previous work [88]. It includes mass and energy balances for both solid and gas phase, accounting for convection axial diffusion, gas-solid transport, conduction and radiation on the solid. It can work in both isothermal and adiabatic conditions; heat and mass transfer coefficients are calculated by specific correlations for laminar flow in square ducts [89]. Model equations, boundary and initial conditions are listed in Table 2.2.

Both homogeneous and heterogeneous kinetic schemes are implemented in the model. Their derivation is reported in Chapter 3 of this work.

Sherwood and Nusselt dimensionless numbers, are evaluated along the dimensionless reactor axial coordinate according to Groppi and Tronconi correlations [90]. Simulations for the adiabatic reactor have been performed with square channel geometry, assuming an asymptotic Sherwood number equal to 2.977.

The model is solved with the methods of lines and it is implemented in a C++ code [91].

Thermodynamic and transport properties were implemented in the OpenSMOKE++ libraries [92].

Table 2.2 Model equations and correlations

Gas Phase

Mass Balance

$$\frac{\delta\omega i}{\delta t} = -\frac{G}{\rho_g\,\varepsilon}\frac{\partial\omega i}{\partial z} - \frac{a_v}{\varepsilon}k_{mat,i}\left(\omega_i - \omega_{wall,i}\right) + \frac{\mathfrak{D}_i}{\varepsilon}\frac{\partial^2\omega i}{\partial z^2} + \frac{1}{\rho_g}\cdot\sum_{j=1}^{NR,\,hom}\upsilon_{i,j}r_j^{hom}MW_i$$

Enthalpy Balance

$$\frac{\partial T_g}{\partial t} = -\frac{G}{\rho_g\,\varepsilon}\frac{\partial T_g}{\partial z} - \frac{a_v}{\varepsilon}\frac{h\left(T_g - T_s\right)}{\rho_g\,\hat{c}_{p,g}} + \frac{1}{\rho_g\,\hat{c}_{p,g}}\cdot\sum_{j=1}^{NR,\,hom}(-\Delta H_{r,j})r_j^{hom}$$

Solid Phase

Mass Balance

$$a_v\,\rho_g\,k_{mat,i}\left(\omega_i - \omega_{wall,i}\right)\cdot\varepsilon + \alpha\cdot\varepsilon\cdot\sum_{j=1}^{NR,\,het}\upsilon_{i,j}r_j^{het}\frac{MW_i}{\hat{S}_{act}} = 0$$

Enthalpy balance

$$\frac{\partial T_s}{\partial t} = a_v h\frac{\left(T_g - T_s\right)}{\rho_s\,\hat{c}_{p,s}(1-\varepsilon)} + \frac{1}{\rho_s\,\hat{c}_{p,s}}\frac{\partial\left(k_{ax}^{eff}\frac{\partial T_s}{\partial z}\right)}{\partial z} + \frac{\alpha}{\rho_s\,\hat{c}_{p,s}\,(1-\varepsilon)}\cdot\sum_{j=1}^{NR,\,het}(-\Delta H_{r,j})r_j^{het}\frac{1}{\hat{S}_{act}}$$

Boundary conditions

Reactor Inlet

$$\omega_i(0,t) = \omega_{feed,i}$$

$$T_g(0,t) = T_{feed}$$

$$\frac{\partial T_s}{\partial z}(0,t) = 0$$

Reactor Outlet

$$\frac{\delta\omega i}{\delta z}(L,t) = 0$$

$$\frac{\delta T_s}{\delta z}(L,t) = 0$$

Initial conditions

$$\omega_i\,(z,0) = 0$$

$$T_g(z,0) = T_{feed}$$

$$T_s(z,0) = T_{0,wall}$$

Volumetric specific surface area	$\alpha = \frac{m_{cat}\cdot\omega_{Rh}\cdot\gamma\cdot\eta}{\Gamma\cdot MW_{Rh}\cdot V_{reactor}}\left[\frac{m_{Rh}^2}{m_{reactor}^3}\right]$
Rhodium surface site density	$\Gamma = 2.49\cdot10^{-5}\left[\frac{mol}{m_{Rh}^2}\right]$
Mass transfer coefficient	$k_{mat,i} = \frac{Sh\cdot\mathfrak{D}_{i,mix}}{D_{channel}}\left[\frac{m}{s}\right]$
Heat transfer coefficient	$h = \frac{Nu\cdot k_{gas}}{D_{channel}}\left[\frac{m}{s}\right]$
Sherwood number	$Sh = Sh_\infty + 6.874\cdot(1000\cdot z^*)^{-0.488}\exp(-57.2\cdot z^*)\ [\text{-}]$
	$z^* = \frac{z - L_{inert}}{D_h\cdot Re\cdot Pr}$
Nusselt number	$Nu = Nu_\infty + 8.827\cdot(1000\cdot z^*)^{-0.545}\exp(-48.2\cdot z^*)\ [\text{-}]$
	$z^* = \frac{z - L_{inert}}{D_h\cdot Re\cdot Sc_i}$

3. Derivation of a concerted hetero-homogeneous kinetic mechanism for ethanol catalytic partial oxidation

Investigating bioethanol as a renewable energy source holds significative importance in the context of H_2-based economy. Ethanol partial oxidation and steam reforming on Rh/Al_2O_3 represent promising processes that have already proved to be highly tangled reacting systems.

In view of a dedicated modelling analysis for the optimization of H_2 production from ethanol in an autothermal reformer (see Chapter 4), the necessity to combine the description of both solid and gas phase reactivities appears essential, being the latter of utmost importance in the typical operating temperatures of the fuel processor [24].

In this chapter, the development of an engineering tool that can capture all the relevant features of the process is presented: a combined homo-heterogeneous kinetic scheme is developed and validated against experimental data, informative of the catalytic and thermal activation of the C_2-alcohol [87].

3.1 Development of a reduced homogeneous kinetic model

The background on homogeneous chemistry of ethanol pyrolysis and oxidation is reported by Ranzi et al. [93]. This mechanism has been updated and is included in a comprehensive C1-C3 high temperature kinetic mechanism (named "CRECK_2003_C1_C3_HT"), that was developed following a hierarchical methodology: the core C0-C2 subset, including ethanol, was taken from the ARAMCO mechanism of Metcalfe et al. [94], while C3 chemistry was taken from Burke et al. [95]. Thermodynamic properties were accounted for from the database of Burcat and Ruscic [96]. The final mechanism includes 114 species and 1999 reactions, and it is available with thermodynamic and transport properties [97].

In this section, a 36-species reduced homogeneous scheme is developed, able to catch monitored patterns with a limited computational load.

3.1.1 Homogeneous kinetics: complete scheme reduction

In this work, the detailed mechanism has been reduced in order to be flexibly applied to simulation of catalytic processes operating under fuel rich oxidation conditions. To this purpose, the methodology described in [98] was employed, as incorporated in the DoctorSMOKE++ tool. The Directed Relation Graph with Error Propagation (DRGEP) [99] was thus coupled to sensitivity analysis on species [100]. A maximum 10% error on ignition delay time was set as target of

accuracy, and 1D homogeneous reactors were used to sample reaction states. The obtained skeletal mechanism included 51 species and 613 reactions. This reduced mechanism was validated against a wide range of existing experimental datasets (jet-stirred reactors, flow reactors, ignition delay times and laminar flame speeds) in order to test the accuracy of the reduction method.

As an example, Figure 3.1 shows the effect of model reduction in the simulation of the data by Alzueta et al. [101], who studied the oxidation of ethanol in presence of H_2O in an atmospheric laminar flow reactor in the temperature range 700-1500 K ($\lambda = 1.13$). [101]

The reduced model (solid lines) fully replicates the response of the detailed model (dotted lines); both models predict the conversion of ethanol satisfactorily, while underestimate the initial formation of CO and CO_2 and show a delay of about 50 K. This reactor was simulated using a plug flow model, i.e. neglecting the possible effect of diffusion on the reactivity of the system. Adopting a plug flow model to simulate a laminar reactor might lead to an underestimation of the reactivity of the order of 25-75 K, as highlighted by Stagni et al. [102] who compared a 2D CFD modelling with a plug flow assumption for the oxidation of DME in a laminar flow reactor. Such a complex modelling activity is outside the scope of this work.
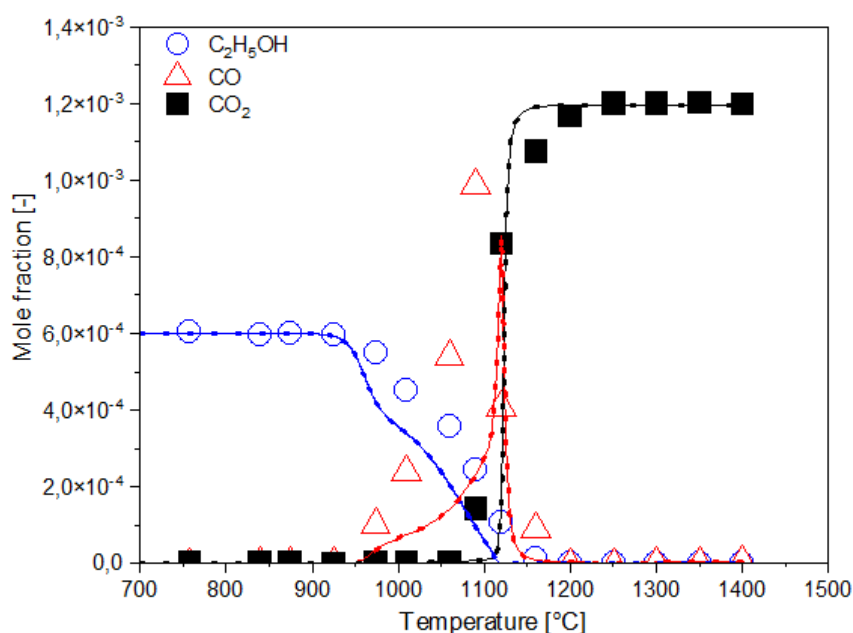
Figure 3.1 Oxidation of ethanol in atmospheric flow reactor at $\lambda = 1.13$. [112] Comparison between experimental data (symbols), complete model predictions (dotted lines) and 51 species reduced model predictions (solid lines).

The reduced mechanism could be further reduced to 36 species and 400 reactions (available as supplementary material in .zip package), focusing on the low pressure and high dilution conditions of interest for the simulation of the present catalytic and homogeneous tests.

3.1.2 Ethanol gas-phase oxidation mechanism

The gas phase oxidation of ethanol is initiated mainly by reaction with OH radicals, even though the interaction with H, HO_2 and CH_3 is also significant. According to the gas-phase mechanism in Figure 3.2 - with the depth of the arrows showing the relative importance of the different reaction paths -, ethanol is initially consumed via H-abstraction reactions forming mostly the secondary radical (CH_3CHOH) which leads to the production of acetaldehyde. The formation of the primary ethanol radical is significant but less important and leads to the formation of ethylene. Finally, the alcoxy radical is formed in lower amounts and supports the formation of CH_2O. The role of molecular dehydration of ethanol to form ethylene is quite small in these conditions. The main homogeneous consumption route of ethanol is thus the following: $C_2H_5OH \rightarrow CH_3CHOH \rightarrow CH_3CHO \rightarrow \ldots \rightarrow CO \rightarrow CO_2$. Acetaldehyde is the primary intermediate species, which at higher temperatures is consumed to form CO and CH_3 (via acetyl radical CH_3CO). CO is subsequently oxidized to CO_2 by OH radicals. Molecular hydrogen is formed by H-abstraction reactions of H radicals.
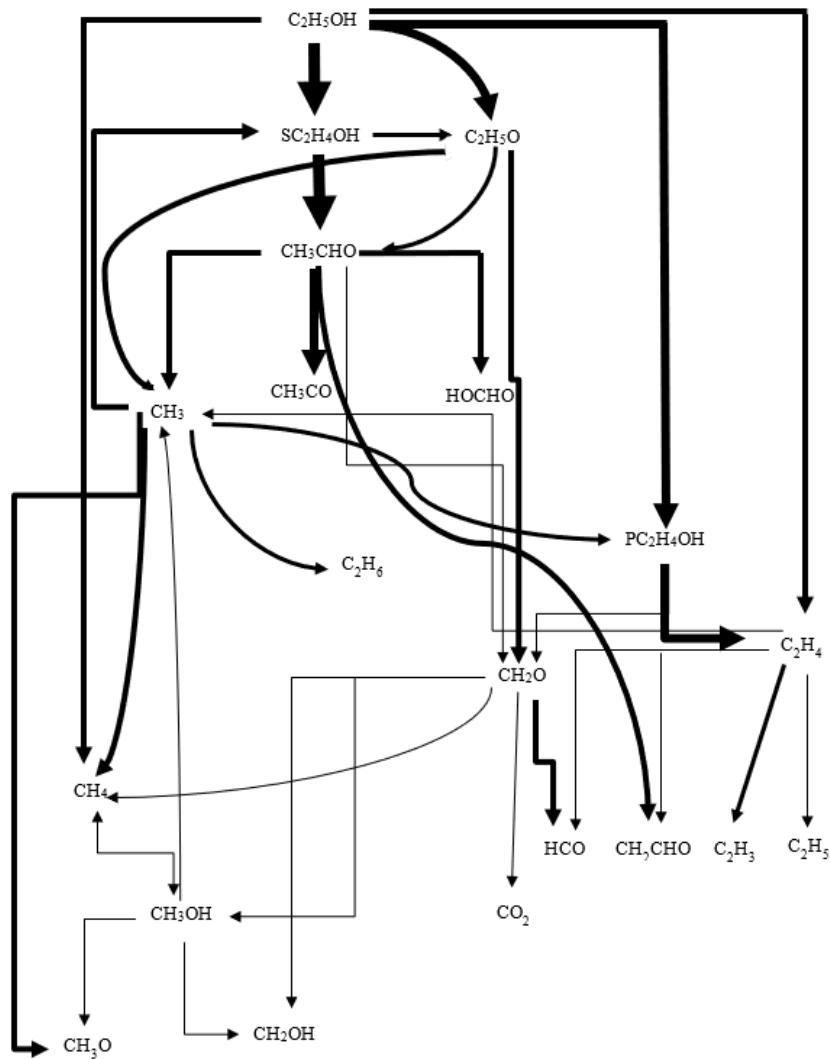
Figure 3.2 Reaction flux analysis for ethanol oxidation using the reduced 36 species mechanism. Operating conditions: C_2H_5OH = 1.5 %, O_2 = 1.68%, N_2 to balance. Flowrate = 812 Nml/min (τ = 0.05 s); Temperature = 1023 K; Pressure = 1 atm.

3.1.3 Validation of the reduced homogeneous kinetic scheme

In this work, the gas phase reactivity of ethanol/O_2/N_2 mixtures was studied by performing tests at 1.5% ethanol, 1.68% O_2 and N_2 to balance, by varying inlet flowrate between 225 and 1334 Nml/min in the temperature range 400 - 850 °C.

Figure 3.3 shows the experimental results (symbols) as well as the predictions of the reduced (solid lines) versus complete (dashed lines) homogeneous mechanism.
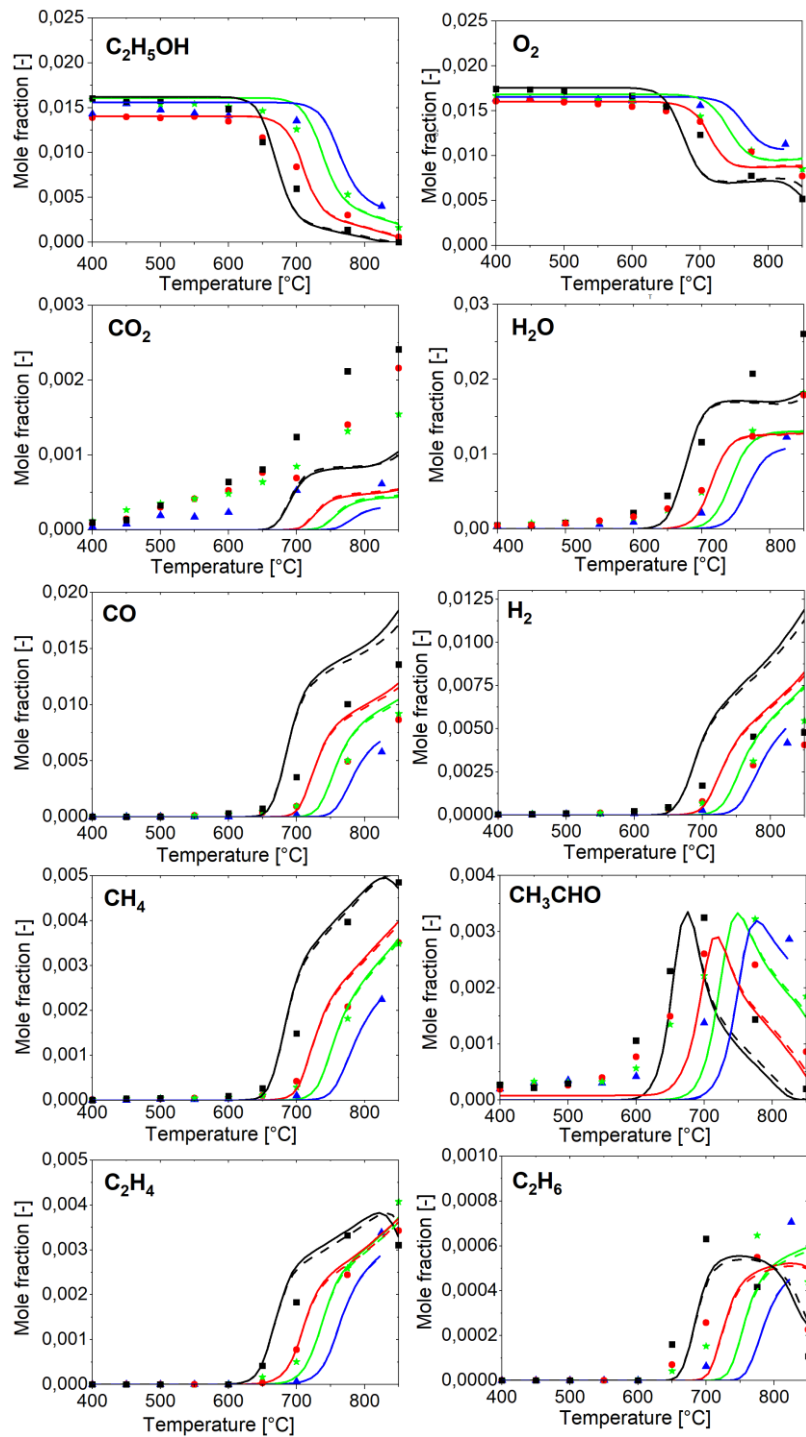
Figure 3.3 Effect of flowrate on homogeneous ethanol oxidation. Experimental data (symbols), complete model predictions (dashed lines) and 36 species reduced model predictions (solid lines) are reported. Operating conditions: $C_2H_5OH = 1.5\%$, $O_2 = 1.68\%$, N_2 to balance. Black-squares: flowrate = 225 Nml/min ($\tau = 0.19$ s); Red-circles: flowrate = 451 Nml/min ($\tau = 0.09$ s); Green-stars: flowrate = 812 Nml/min ($\tau = 0.05$ s); Blue-triangles: flowrate = 1334 Nml/min ($\tau = 0.03$ s).

In the absence of the catalyst, ethanol conversion starts at 600 °C or even higher temperatures for shorter residence times, thus excluding the influence of homogenous reactions in the low temperature region in the conditions mostly investigated experimentally.

The model predictions describe in a satisfactory way the general trends and provide a key for the

29

interpretation of results.

Experimental results show that H_2 and CO were mainly formed at 700-750 °C, while minor amounts of CO_2, and C_2 species (ethane and ethylene) were also detected. At decreasing flow rate, the conversion was progressively anticipated, and the production of all terminal species grew. The observed trends of acetaldehyde confirmed the character of intermediate species.

Notably, the model predictions tend to partly overestimate syngas production while the concentration of CO_2 is underestimated. This has been interpreted as a residual catalytic effect of the inner surfaces of the reactor. Despite of these deviations, the agreement between experimental measurements and the model predictions is in general satisfactory, since the effect of both temperature and flowrate (i.e. residence time τ in the reactor) is well predicted by the model.

In order to investigate the existence of possible cracking reactions contextually to ethanol oxidation, an experimental test of ethanol pyrolysis was performed in homogeneous phase.

The experiment was carried out for a given ethanol concentration of 1 % and temperatures in the range of interest (400 – 850 °C), at a fixed total flow rate (including diluent nitrogen) of 400 Nml/min.

The experimental results obtained are plotted in Figure 3.4 as symbols, together with simulations represented with lines.
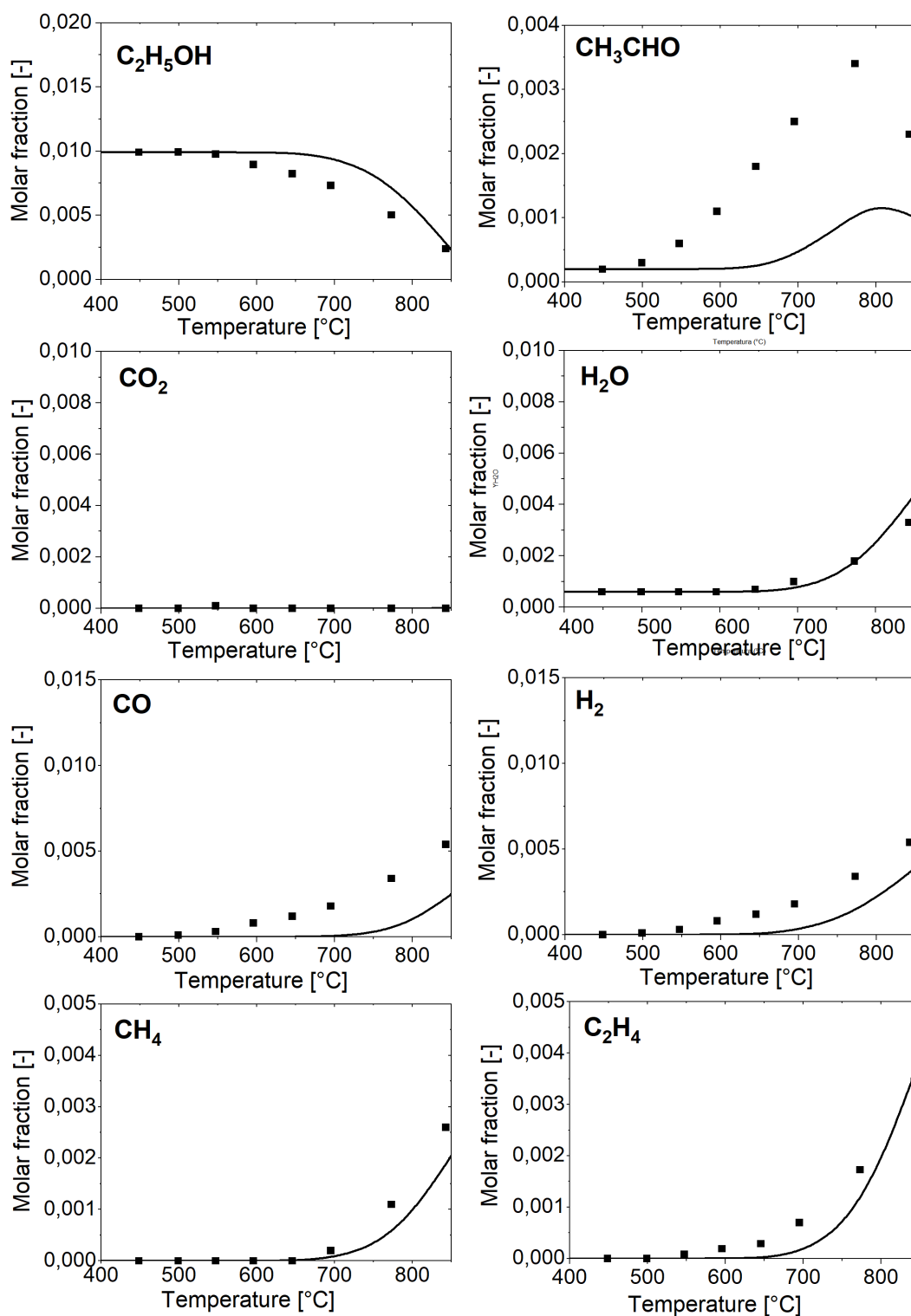
Figure 3.4 Homogeneous pyrolysis of ethanol. Experimental data (symbols) and 36 species model predictions (lines) are reported. Operating conditions: $C_2H_5OH = 1\%$, N_2 to balance; Flow rate = 400 Nml/min ($\tau = 0.10$ s)

As already observed for homogeneous oxidation, activation of ethanol in absence of catalyst is possible only above 600 °C. The presence of oxygen in the structure of the fuel allows the observation of CO in the gas outlet stream. As it concerns CO_2, it would be necessary to reach temperatures higher than 1000 °C in order to see its concentration considerably increasing [103].

Among the most important detected products, only acetaldehyde shows a behavior through a maximum, and its onset consumption could be explained through a route to methane and CO [104]. Ethylene and methane concentrations increase with temperature, but no decrement is highlighted, since their further consumption to produce polycyclic aromatic hydrocarbons only occurs at higher temperatures [103].

It is noticeable a satisfactory agreement between experimental results and calculations for the modeled species, even though the reduced mechanism adopted only takes into account gas-phase processes. This does not affect the quality of the predictions since the formation of soot is typically observed above 1000 °C [103], out of the range of our experimental conditions. Discrepancies in acetaldehyde fitting could be justified also in this case as a residual catalytic fouling.

These achievements confirm the reliability of the skeletal reduction process and allows for the extension of the experimental database for ethanol oxidation and pyrolysis already available in literature [105].

The comparison also shows that the predictions of the complete and reduced mechanisms are virtually identical, thus enabling the adoption of the reduced mechanism in coupled homogeneous/heterogeneous simulations of a catalytic reactor with a significant reduction of the computational effort.

These results confirm that in a catalytic ethanol-to-H_2 system, not only heterogeneous reactions, but also homogeneous oxidation and thermal cracking can play a role in the formation of products at temperatures higher than 600 °C.

3.2 Development of a heterogenous kinetic scheme

In this section a macro-kinetic heterogeneous scheme with six molecular reactions (ethanol oxidative dehydrogenation, total oxidation, decomposition, dehydrogenation, steam reforming and acetaldehyde post-reforming) is tuned to accurately describe ethanol/O_2 and ethanol/H_2O reacting systems.

The reactivity of ethanol on Rh/Al_2O_3 catalyst was described by following the same lumped approach adopted for developing the kinetics of CH_4 [80], formic acid [106] and C_{2+} hydrocarbons [107], [108]. This consists of building a kinetic scheme that incorporates all the stoichiometries that are necessary to reproduce the speciation of the reacting system and formulating for each reaction an analytic expression that reflects the dominant kinetic dependences from gas-phase species. In this way a subsystem is created, that can be coupled with existing subsystems that cover the C_1-C_8 partial oxidation and steam reforming systems [80], [107]. The reaction rates of this macro-kinetic

scheme are expressed per unit mass of the catalyst Rh/Al$_2$O$_3$ (g$_{cat}$).

Catalytic tests were performed to collect the necessary data sets, build the kinetic model and fit the parameters through the mathematical model accurately described elsewhere [87]. While data and their analysis are discussed in the following, the final scheme is reported in Table 3.1. It includes reactions and rate expressions for oxidation and steam reforming of ethanol, along the lines of the previous experience on hydrocarbons CPO over Rh-alumina catalyst; besides, it incorporates oxidative dehydrogenation, dehydrogenation and decomposition reactions that are specific of the C$_2$-alcohol. The complete ethanol scheme includes as relevant subsystem the pre-existing C$_1$ sub-scheme, comprising CH$_4$ total oxidation and SR, WGS (modified by C-poisoning term) and rev-WGS, H$_2$ and CO oxidation, whose rate expressions and parameters were maintained from the original sources [80].

As a consolidated procedure, tests of CH$_4$ CPO were used as benchmark to evaluate the consistency between the pre-existing C$_1$ kinetic scheme and the behaviour of newly prepared catalytic reactors.

Table 3.1 Reaction scheme of ethanol reactivity on Rh/Al$_2$O$_3$.

Reaction	Rate equation [mol/(g$_{cat}$ s)]	$k_{rif,j}^{873K}$ [mol/(atm g$_{cat}$ s)]	E_{act} [kJ/mol]
C$_2$H$_5$OH oxidative dehydrogenation $C_2H_5OH + 0.5\ O_2 \rightarrow CH_3CHO + H_2O$	$r_{ODH} = k_{ODH} \cdot P_{O_2}$	3.97×10^{-1}	50
C$_2$H$_5$OH dehydrogenation $C_2H_5OH \rightarrow CH_3CHO + H_2$	$r_{deH} = k_{deH} \cdot P_{C_2H_5OH} \cdot \sigma_{O_2}$	3.84×10^{-2}	40
C$_2$H$_5$OH total oxidation $C_2H_5OH + 3\ O_2 \rightarrow 2CO_2 + 3H_2O$	$r_{TO} = \dfrac{k_{TO} \cdot P_{O_2}}{\left(1 + K_1 \cdot \frac{P_{O_2}}{P_{C_2H_5OH}}\right)^2}$	3.209×10^{1} [108]	54 [108]
C$_2$H$_5$OH decomposition $C_2H_5OH \rightarrow CH_4 + CO + H_2$	$r_{DEC} = k_{DEC} \cdot P_{C_2H_5OH} \cdot \sigma_{O_2}$	7.935×10^{-2}	50
C$_2$H$_5$OH steam reforming $C_2H_5OH + H_2O \leftrightarrow 2CO + 4H_2$	$r_{SR,C_2H_5OH} = \dfrac{k_{SR_{C_2H_5OH}} \cdot P_{C_2H_5OH} \cdot (1 - \eta_{SR})}{1 + \frac{K_C \cdot P_{C_2H_5OH}}{P_{H_2O}}}$	4×10^{-2}	90
CH$_3$CHO steam reforming $CH_3CHO + H_2O \leftrightarrow 2CO + 3H_2$	$r_{SR,CH_3CHO} = \dfrac{k_{SR,CH_3CHO} \cdot P_{CH_3CHO} \cdot (1 - \eta_{SR})}{1 + \frac{K_C \cdot P_{C_2H_5OH}}{P_{H_2O}}}$	1.2×10^{-1}	30
WGS $CO + H_2O \leftrightarrow CO_2 + H_2$	$r_{WGS} = \dfrac{k_{WGS} \cdot P_{H_2O} \cdot (1 - \eta_{WGS})}{1 + \frac{K_C \cdot P_{C_2H_5OH}}{P_{H_2O}}} \cdot \sigma_{CO}$	6.831×10^{-3} [107]	75 [107]

Where $K_1 = 1.4 \exp\left[\frac{22}{R} \cdot \left(\frac{1}{T} - \frac{1}{T_0}\right)\right]$ [108] and $K_C = 11.98 \exp\left[\frac{50}{R} \cdot \left(\frac{1}{T} - \frac{1}{T_0}\right)\right]$

Temperature dependence of kinetic constants was expressed with a modified Arrhenius form: $k(T) = k(T_{ref}) \cdot \exp\left(-E_{act}/R(1/T - 1/T_{ref})\right)$. Terms $(1 - \eta_j)$ indicate equilibrium constraints, where η_j represents the ratio of

the experimental reaction quotient $K_{p,j}$ and the thermodynamic equilibrium constant $K_{eq,j}$. Coefficients σ_i are needed to account for the extinction of the co-reactant: $\sigma_i = P_i/(P_i + 10^{-6})$.

$\sigma_i = P_i/(P_i + 10^{-6})$.

3.2.1 Steam reforming

Tests of ethanol SR were carried out at 1.5% ethanol and 3-3.8% H_2O feed contents, at varying GHSV (0.9 and $1.5 \cdot 10^6$ NL/kg_{cat}/h). Experimental results are shown in Figure 3.5, where ethanol conversion and outlet molar fractions are plotted against the average catalytic bed temperature.

The onset of ethanol conversion is seen at temperatures higher than 500 °C, accompanied by H_2O consumption. The major products are CO and H_2, and their molar fractions increase with temperature while approaching equilibrium concentrations. In addition, CO_2 is also observed among products; its production can be explained by the onset of the water gas shift reaction. The stoichiometries of steam reforming and WGS can thus explain most of the product composition. At this stage, it is observed that traces of ethylene (maximum 500 ppm), acetaldehyde (maximum 250 ppm) and CH_4 (maximum 400 ppm) are also detected among the products; their formation is discussed below.

In a previous study [25], the reactivity of the ethanol/H_2O reacting system on Rh was analyzed by combined activity tests, Raman spectra, *operando* FTIR and TPO measurements. Based on these results, the high-temperature onset of the steam reforming reaction (consistent with an apparent activation energy as high as 180 kJ/mol) has been associated to the hindering effect of adsorbed C_2 oxygenated species (including acetaldehyde, acetates, ethoxy species). In turn, such species are believed responsible for C-C coupling reactions eventually leading to the formation of disordered and graphitic C-structures, visible by Raman. Consistently, TPO measurements on spent catalysts allowed to quantify C-deposits and revealed the co-presence of different types of structures, with diverse O-content and interaction with catalytic surface. At higher temperature, though, gasification reactions would consume such species, favouring the full availability of the surface active sites.

This complex picture of C-poisoning can be rendered in kinetic terms by assuming a dynamic equilibrium between formation and consumption of surface C-species, such that the rate of formation depends on the gas-phase concentration of ethanol and the coverage of free sites θ (3.1):

$$r_{C-formation} = k_{C,f} \cdot P_{C_2H_5OH} \cdot \theta \tag{3.1}$$

and the rate of C-consumption depends on the gas-phase concentration of H_2O (the gasification medium) and the surface coverage of C-species θ_C (3.2):

$$r_{C-consumption} = k_{C,c} \cdot P_{H_2O} \cdot \theta_C \tag{3.2}$$

The beneficial effect of H_2O for Rh-based catalysts stability in ethanol-to-H_2 processes is widely explained in the literature ([109], [110]).

By assuming steady state conditions, and thus equalling the rates of formation $r_{C-formation}$ and consumption $r_{C-consumption}$, the following relationship is obtained between the coverage of free

sites and the coverage of C-poisoned sites (3.3):

$$\frac{\theta_C}{\theta} = \frac{k_{C,f}}{k_{C,c}} \cdot \frac{P_{C_2H_5OH}}{P_{H_2O}}$$

(3. 3)

By additionally assuming that C-poisoned sites are the MASI, such that the site balance reduces to (3.4):

$$\theta + \theta_c = 1$$

(3. 4)

the following expression is obtained (3.5):

$$\theta = 1 - \theta_c = \left(1 + \frac{K_C \cdot P_{C_2H_5OH}}{P_{H_2O}}\right)^{-1}$$

(3. 5)

where K_C is the lumped parameter, corresponding to the ratio between rate constant of formation $k_{C,f}$ and rate constant of gasification of C-species $k_{C,c}$.

The rate expression of the forward steam reforming was thus obtained by assuming that it is proportional to the partial pressure of ethanol and the surface concentration of free sites, which brings to the following (3.6):

$$r_{SR,C_2H_5OH} = k_{SR_{C_2H_5OH}} \cdot P_{C_2H_5OH} \cdot (1 - \theta_c) \cdot (1 - \eta_{SR})$$

(3. 6)

as reported in Table 3.1.

The term $(1 - \eta_{SR})$ accounts for the approach to equilibrium and conveys thermodynamic consistency.

Notably, the same phenomenology was observed in the study of propylene steam reforming, where the same formalism was successfully adopted [108]. Indeed, it has been verified that under the investigated operative conditions CO-poisoning has not a relevant contribution, differently from what was observed by some of the authors for a cleaner fuel as methane [111].

The kinetic parameters of rate expression (Eq.6) were adapted to the steam reforming data, accounting also for the WGS reaction. An activation energy of 90 kJ/mol was estimated for the intrinsic rate constant, a value that is comparable with the estimated energy barriers for several fuels so far studied and is considerably lower than the apparent activation energy that emerges when C-poisoning term is not considered [25]. It results higher than the activation energy of propylene, but very similar to that of CH$_4$ and propane SR reactions [80], [107], [108].

Figure 3.5 reports the comparison between model fit (solid lines = incorporation of the heterogeneous scheme) and experimental data, and a very satisfactory description of system composition is observed.

It is also observed that, although not discussed in detail, the model predictions account for a minor formation of CH$_4$ and acetaldehyde in the very intermediate temperature region where these trace species were observed. The simulations were obtained by applying the entire kinetic scheme

reported in Table 3.1, thus including also the O-dependent reactions; indeed, as explained in the experimental methods in Section 2, the H_2O feed to the annular reactor was obtained by a dedicated upstream unit, consisting of Pt-containing packed bed reactor fed by slightly over stoichiometric H_2/O_2 mixtures. A minor slip of O_2 (about 50 ppm) was detected by GC analysis from the Pt reactor; by accounting for such small amount of O_2 in the SR feed, a little contribution from oxidative reactions was predicted leading to the formation of CH_4 (via ethanol oxidative decomposition) and acetaldehyde (via oxidative dehydrogenation).

The Figure 3.5 also reports the simulations obtained by combining the homogeneous and the heterogeneous scheme (dotted lines = incorporation of both kinetic schemes). Apparently, gas-phase reactions had a negligible impact; however, interestingly, homogenous reactions can explain the very high temperature formation of traces of acetaldehyde and methane. Also traces of ethylene were predicted at high temperature, although not detected in the reactor outlet.

As a further support to the SR kinetics, it is mentioned that additional data of ethanol steam reforming were simulated, including tests at lower H_2O content where C-poisoning was emphasized and tests that were performed in rapidly descending ramps from high temperatures, in the attempt to contrast the formation of C-species.

Finally, it is worth emphasizing that, consistently with the SR kinetics, a correction by surface C-poisoning was applied to the water gas shift reaction (as shown in Table 3.1). Indeed, the productivity of CO_2 herein observed was largely lower than expected based on the original studies by Donazzi et al. [80] and Pagani et al. [107]. Instead, as shown by the solid lines in Figure 3.5, a very satisfactory description was obtained by assuming that the same hindering effect of C-forming reactions similarly reduces the available sites for the WGS reaction, whose rate equation and intrinsic parameters were maintained unchanged.
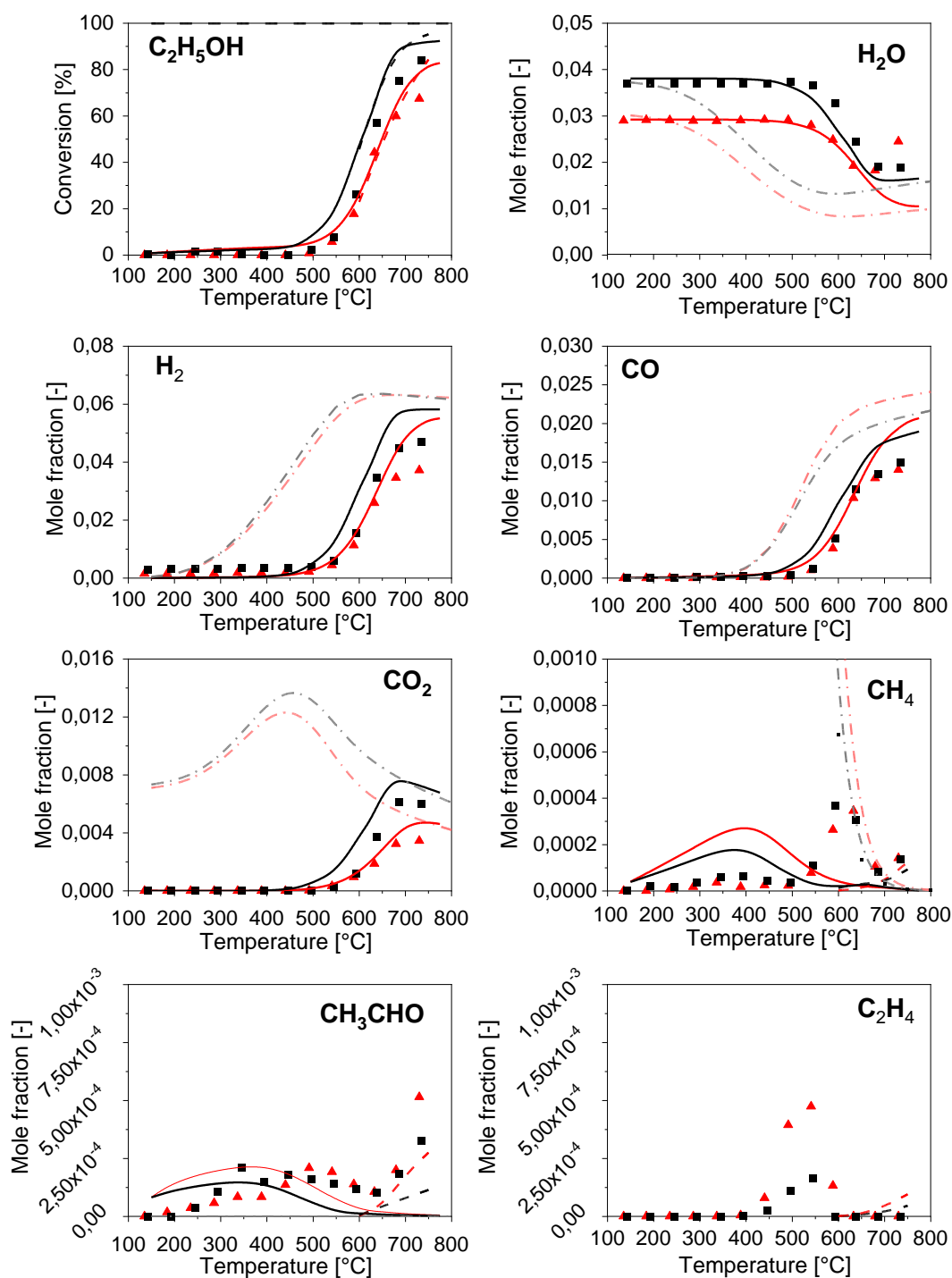
Figure 3.5 Ethanol SR tests. Experimental data (symbols), heterogeneous model predictions (solid lines), homo/heterogeneous model predictions (dashed lines) and equilibrium compositions (dot-dashed lines) are reported. Operating conditions: $C_2H_5OH = 1.5$ %, N_2 to balance. Black-squares: GHSV $= 0.9 \cdot 10^6$ NL/kg$_{cat}$/h, $H_2O = 3.8$%; Red-triangles: GHSV $= 1.5 \cdot 10^6$ NL/kg$_{cat}$/h, $H_2O = 3$%.

3.2.2 Catalytic Partial Oxidation

An extensive discussion on the multiple reaction pathways observed in ethanol CPO has been addressed in [25], and is here briefly summarized. Reference CPO data (with ethanol and O_2 feed content of 1.5% and 1.68%, respectively, and GHSV of 5 and $9 \cdot 10^5$ NL/kg$_{cat}$/h) are reported in Figure 3.6, in terms of ethanol and oxygen conversion and molar fractions of the reaction products. In the low temperature range (T < 200 °C) ethanol oxidative dehydrogenation to acetaldehyde is responsible for the initial conversion of reactants; the remarkable feature revealed by the tests in annular reactor at high space velocity is that this reaction extinguishes at increasing temperature, since acetaldehyde concentration and ethanol conversion pass through maxima.

Ethanol total oxidation to CO_2 and H_2O and ethanol oxidative decomposition to CH_4, CO and H_2 are instead activated above 250 °C. As long as O_2 is present on the surface, these species are subjected to post-oxidation reactions; CH_4 formation likely contributes to the medium temperature production of H_2 and CO, via consecutive steam reforming (that according to our previous studies is active only if O_2 is consumed [80]).

Still in the intermediate temperature range a secondary formation of acetaldehyde is observed, likely associated to a dehydrogenation route possibly occurring on the support. Other experiments prove that the importance of this reactivity is strictly related to the γ-Al_2O_3 batch utilized for catalyst preparation; in this respect, Le Valant and co-workers in [112] state that this reactivity is correlated to the basicity of the support.

In line with ethanol SR experiments, the onset of ethanol reforming (with important production of CO and H_2, together with ethanol and water consumption increase) is delayed at temperatures higher than 500 °C. The two runs reported in Figure 3.6 show that in the intermediate T-range, in between 300 and 500 °C, ethanol conversion presents a sort of "plateau-like" behaviour which is in line with the hypothesis that once O_2 is fully consumed, a C-poisoned regime similar to SR system causes the delayed ignition of ethanol reforming. At the maximum temperature of 775°C – for the highest GHSV of $9 \cdot 10^5$ NL/kg$_{cat}$/h – the observed C selectivity to CO and H selectivity to H_2 are around 78%, with a total ethanol conversion of 100%.

All these stoichiometries were incorporated in the kinetic scheme of Table 3.1 and kinetic dependences were formulated based on an extensive experimental campaign of ethanol CPO tests at varying feed composition and space velocity. Similarly to steam reforming, the proposed rate expressions respect the analogy with the kinetics of other fuels studied in the past as well as the search for simple analytic expressions.
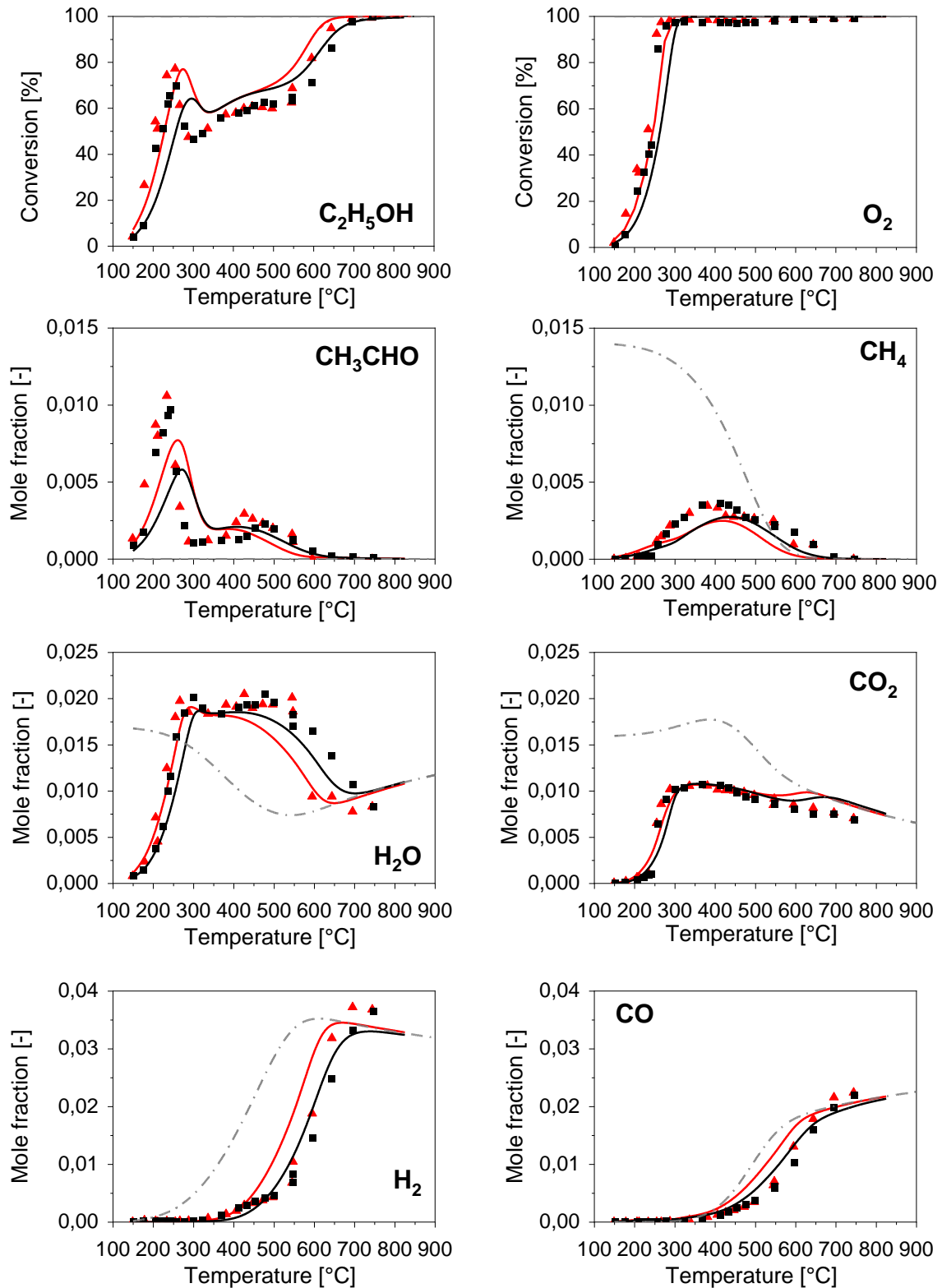
Figure 3.6 Ethanol CPO tests. Experimental data (symbols), heterogeneous model predictions (solid lines) and equilibrium compositions (dot-dashed lines) are reported. Operating conditions: $C_2H_5OH = 1.5$ %, $O_2 = 1.68$%, N_2 to balance. Black-squares: GHSV = $9\cdot10^5$ $NL/kg_{cat}/h$; Red-triangles: GHSV = $5\cdot10^5$ $NL/kg_{cat}/h$.

The kinetics of the low temperature oxidative dehydrogenation to acetaldehyde and water was described by assuming a direct dependence on the gas-phase concentration of O_2. Indeed, on the

one side this unique route is observed only in O_2 co-feed tests, on the other side the "extinction" above 200 °C can be explained by the rapid depletion of O_2, due to the onset of deep oxidation. The following kinetic expression has been introduced to describe acetaldehyde "peak" (3.7):

$$r_{ODH} = k_{ODH} \cdot P_{O_2} \qquad (3.7)$$

where it is assumed that ethanol oxidative dehydrogenation is not impacted by ethanol concentration, which presumably reaches a saturation value on the surface, but rather by O_2 partial pressure.

The key role of surface O_2 availability on oxidative dehydrogenation reaction together with the limited influence of GHSV on acetaldehyde production suggest that the reaction is associated with a specific nature of adsorbed oxygen, possibly undissociated Rh-O_2, from which RhO* sites (typically involved in the deep oxidation activity) originate. Such Rh-O_2 sites might be present on the catalytic surface in limited amount (e.g., on Rh/support interface) and characterized by a vivid H-abstraction activity. It is also suggested that ethanol oxidative dehydrogenation requires the vicinal interaction of both O_2 and ethanol molecules on the surface, i.e. the presence of vicinal Rh-O_2 and C_2H_5OH*.

By virtue of the similar consumption trend of ethanol compared to propylene, the same reaction rate expression was chosen to describe ethanol total oxidation over Rh catalysts, here reported in (3.8) [108]:

$$r_{TO} = \frac{k_{TO} \cdot P_{O2}}{\left(1 + K_1 \cdot \dfrac{P_{O2}}{P_{C_2H_5OH}}\right)^2} \qquad (3.8)$$

A negative dependence on O_2 and a second order dependence on the fuel partial pressure were thus assumed. In analogy with the case of propylene, the macro-kinetic dependencies in Eq.8 can be estimated by assuming a kinetic regime similar to the one proposed by Iglesia and co-authors in [113]–[115]: the rate determining step in the activation of the fuel is assumed as the dissociative adsorption on the pair Rh-RhO* sites, being the adsorbed molecular oxygen irreversibly dissociated into atomic O*; due to the very high reactivity of the fuel, the surface concentration of O* species would result from the dynamic equilibrium between O_2 adsorption and surface oxygen consumption by deep oxidation. Indeed, the pre-exponential factor and the activation energy of k_{TO}, the parameter representative of O_2 activation, were kept equal to the values proposed in [108], with a pre-exponential factor of 32.1 mol/(atm· g_{cat} ·s) at 873 K and an activation energy of 54 kJ/mol. The global parameter K_1 at the denominator is instead the ratio between k_{TO} and the rate constant of O* consumption. Also the parameters for the evaluation of this term were mantained the same as those of propylene [108], showing to be more dependent on the process of O_2 activation rather than the fuel nature.

In order to account for the formation of methane observed in the intermediate temperature range, a catalytic decomposition of ethanol was introduced. As shown in the proposed reaction rate for decomposition (3.9), a simple first order dependence on fuel partial pressure was chosen.

$$r_{DEC} = k_{DEC} \cdot P_{C_2H_5OH} \cdot \sigma_{O2}$$ (3. 9)

A value of activation energy of 50 kJ/mol was estimated, as reported in Table 3.1. This reaction route was also observed by A. Cifuentes et al. [116] in the low temperature range over Rh-Pd/CeO$_2$ catalyst, where a higher activation energy was evaluated (87 kJ/mol). Plots of methane concentration in Figure 3.6 show a trend through a maximum peak: C-C bond breaking to methane rate becomes null when oxygen is fully consumed in the system, thus a term σ_{O_2} was introduced to guarantee a numerical dependence on O$_2$ partial pressure. In fact, ethanol decomposition to methane was identified as a more intensive phenomenon with O$_2$ in the reacting mixture, while the production of methane was observed in trace amounts in the steam reforming tests. Indeed, as shown in [25], *operando* IR analyses in ethanol CPO clearly showed the C-C bond cleavage is significantly more favoured in the presence of O$_2$ co-feed rather than H$_2$O co-feed. The presence of a maximum of methane concentration at increasing temperature can be partly explained also by the onset of consecutive reactions (namely oxidation and steam reforming); this is the reason why the ethanol scheme needs a close integration with the C$_1$-scheme, which also involves all the reactions related to the syngas chemistry (water gas shift, reverse water gas shift, methanation), all of them described by reversible rate equations to respect the thermodynamic consistency.

Also, a minor formation of acetaldehyde was observed in the middle temperatures range, whose formation was accounted for through a dehydrogenation reaction of ethanol. Data analysis showed a dependence on ethanol inlet partial pressure, thus leading to the reaction rate expression reported in the following (3.10), where a simple first order dependence on ethanol partial pressure is proposed:

$$r_{deH} = k_{deH} \cdot P_{C_2H_5OH} \cdot \sigma_{O_2}$$ (3. 10)

Differently from the low-temperature formation of acetaldehyde, the bulk of experiments seems to suggest that this secondary contribution of formation is more influenced by the residual concentration of ethanol. As already discussed for decomposition reaction, σ_{O_2} term was introduced to make the reactivity null when oxygen is completely depleted. Indeed, ethanol SR experiments showed that ethanol dehydrogenation is not significantly active in the absence of O$_2$.

High-temperature behaviour of ethanol in CPO is explained by the onset of ethanol steam reforming, which justifies the observed consumption of H$_2$O and residual ethanol. The ethanol reforming reactivity previously presented was hence introduced in the complete kinetic scheme for ethanol CPO, maintaining the same rate expression with C-poisoning. Indeed, as in the case of

ethanol SR system, also in CPO the onset of reforming takes place at temperatures much higher than O_2 consumption. An equivalent state of surface coverages is then expected for both ethanol CPO and SR [106].

In analogy with ethanol steam reforming kinetic, a reaction of acetaldehyde steam reforming was introduced (3.11):

$$r_{SR,CH_3CHO} = \frac{k_{SR\,CH_3CHO} \cdot P_{CH_3CHO} \cdot (1-\eta_{SR})}{1+\frac{K_c \cdot P_{C_2H_5OH}}{P_{H2O}}} \qquad (3.\,11)$$

All the newly introduced kinetic parameters were estimated by fitting the whole population of SR and CPO data. Figure 3.5 and 3.6 show the satisfactory description obtained by the model in solid lines.

Similarly to the case of SR, also the CPO data were simulated with and without inclusion of the homogeneous scheme; no appreciable contribution from the thermal conversion of ethanol was appreciated, and for this reason homo/heterogeneous model predictions were not reported in the plots. Indeed, even if in Section 3.2 it was shown a role of gas phase reactions above 600 °C, in the presence of the catalytic phase they are significantly hindered because of the fast oxygen depletion.

4. Distributed hydrogen production via bioethanol autothermal reforming on structured catalysts

On-board production of H_2 from liquid fuels represents a valuable solution to enhance the vehicle energy efficiency and solves the several issues (safety, energy density) related to hydrogen storage. In view of zero-emission strategies, bio-ethanol represents a promising model fuel as its combustion does not increase the net amount of greenhouse gas emissions.

Catalytic partial Oxidation (CPO) on Rh-catalysts is an attractive technology for the on-board H_2 production. By working in excess of oxygen with respect to the stoichiometry of ethanol partial oxidation, because of the high exothermicity of the process, the reaction can be conveniently carried out in adiabatic reactors of compact size and fast response to variable loads. Steam reforming of ethanol and water gas shift are also relevant reactions to be considered in the global process of ethanol conversion.

This chapter focuses on the analysis of experimental data collected in a quasi-adiabatic rig equipped for spatially resolved measurements of temperature and concentration profiles by means of a mathematical model able to predict the behaviour of an autothermal ethanol reformer through the implementation of the gas and solid phase reactivity schemes derived in Chapter 3.

4.1 Experimental campaign

The experiments reported in this thesis were taken from a recent work of our group [24] where H_2O co-feed in ethanol CPO was explored as a potential strategy for contrasting C-deposition phenomena, recognized to be a major source of activity loss and thermal drift of the reactor. For the sake of clarity, a description of the experimental data is reported in the following taken for reference [24].

Ethanol CPO tests were conducted in a lab-scale autothermal reformer according to the description given in Chapter 2 (section 2.2.2): experiments were performed at atmospheric pressure, with an inlet flow rate of 10 Nl/min, with C/O ratio of 0.65 and 11.2 mol% C_2H_5OH concentration, changing the water molar fraction in the feed ($Y_{H_2O} = 0 - 0.1$).

The C/O ratio was defined following the same definition presented in [23], being the molar flow of carbon of ethanol divided by the molar flow of oxygen in both ethanol and air:

$$C/O = \frac{2 n C_2H_5OH}{n C_2H_5OH + 2 n O_2} \qquad (4.1)$$

The reacting mixture was preheated at 100°C and fed to an adiabatic reactor, equipped with a 2 wt.% Rh/α-Al$_2$O$_3$ catalyst supported onto 400 CPSI cordierite honeycomb monolith. Adiabatic conditions were obtained by proper axial (inert monoliths) and radial insulation. The spatially resolved sampling technique was applied to acquire temperature and concentration profiles along the axis of the reactor. Experimental data were collected at steady-state conditions. As the oxygen consumption in CPO is assumed to be governed by mass transfer limitations [84], a comparison of its experimental profile with calculated trends proved the reliability of the sampling technique.

Successive temperature and concentration ethanol CPO tests were performed alternatively with the same feeding conditions separated by a characterization methane temperature test. A standard CPO methane test, C/O = 0.9, was used to evaluate the stability of the catalysts in relation to deactivation. In fact, methane oxidation reaction is under mass transfer regime, while steam reforming reaction is under a mixed chemical-diffusive control [117]. Catalyst deactivation has no effect on methane oxidation reaction, given its degree of mass transfer control, while it limits only the CH$_4$ steam reforming reaction rate, hence the rate of heat consumption. In this way, hot spot temperature is a function of catalyst deactivation. A higher hot spot means a higher catalyst deactivation.

A thermodynamic analysis of the system C$_2$H$_5$OH/O$_2$/H$_2$O/N$_2$ was performed to determine the effect of feed composition, thus a parametric analysis on the effect of the C/O ratio and the ratio R (defined by Eq. 2) was performed. Notably, the definition of R is such that H$_2$O was treated as a complementary gas, added to the air/ethanol feed, similarly to the extra N$_2$ feed.

$$R = \frac{n_{N_2\ (complement)} + n_{H_2O}}{n_{air} + n_{C_2H5_{OH}}} \qquad (4.\ 2)$$

This reflects the method of the catalytic testing where various H$_2$O feed content were explored by keeping constant the ethanol and air flows, as well as the total flow rate; thus, water co-feed was always associated with an equal decrease of the dilution N$_2$ feed.

The working conditions of the study were selected in order to keep the reaction system far from the conditions that thermodynamically favours coke formation, and to obtain a trade-off between maximization of syngas production and minimization of hot-spot temperatures while keeping the temperature high enough to relieve the kinetic burden; thus, the effect of H$_2$O co-feed was studied by keeping the R ratio equal to 0.5 and the C/O ratio equal to 0.65.

Fig. 4.1 displays the spatially resolved temperature profiles from the experiments. The temperature profiles for the dry ethanol catalytic partial oxidation (CPO) were consistent with prior research findings [23]. In this case, the introduction of H_2O did not appear to have a significant impact on the thermal behaviour. The intensity and location of the temperature hotspot were similar to those in the absence of H_2O. Furthermore, the temperatures measured at the end of the catalytic layer closely matched the adiabatic equilibrium values derived from thermodynamic calculations.
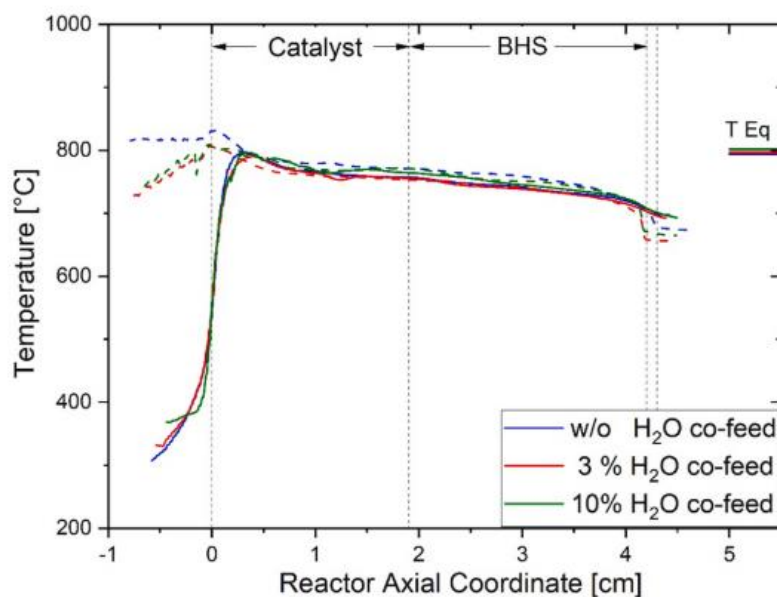
Figure 4.1 Temperature profiles for the CPO of C_2H_5OH with H_2O co-feed; C_2H_5OH = 11.2 %, C/O = 0.65, T_{in} = 100 ∘C, flow rate = 10NL/min [24].

The axial concentration profiles of the reactants and the main products that were measured in the dedicated experiments are plotted in Fig. 4.2 in terms of molar fraction of all the detected gas-phase species.

The consumption of ethanol occurs over a span of approximately 10 mm, resulting from a combination of complete oxidation and steam reforming. It is important to highlight that under O_2 mass transfer limitation, the concentration of O_2 at the interface between the gas and solid phases drops to zero. This enables steam reforming reaction to take place, yielding CO and H_2 even in the presence of O_2 in the bulk phase. At the catalyst entrance, oxidation reactions involving H_2, CO, and ethanol contribute to the observed peak in H_2O concentration and the step increase in CO_2 concentration. Additionally, the sudden rise in H_2 and CO concentrations is related to reforming reactions right at the catalyst entrance. In addition to the primary products of the process, acetaldehyde, ethylene, methane, and to a lesser extent, ethane, were also detected. These findings are detailed in Figure 4.3.
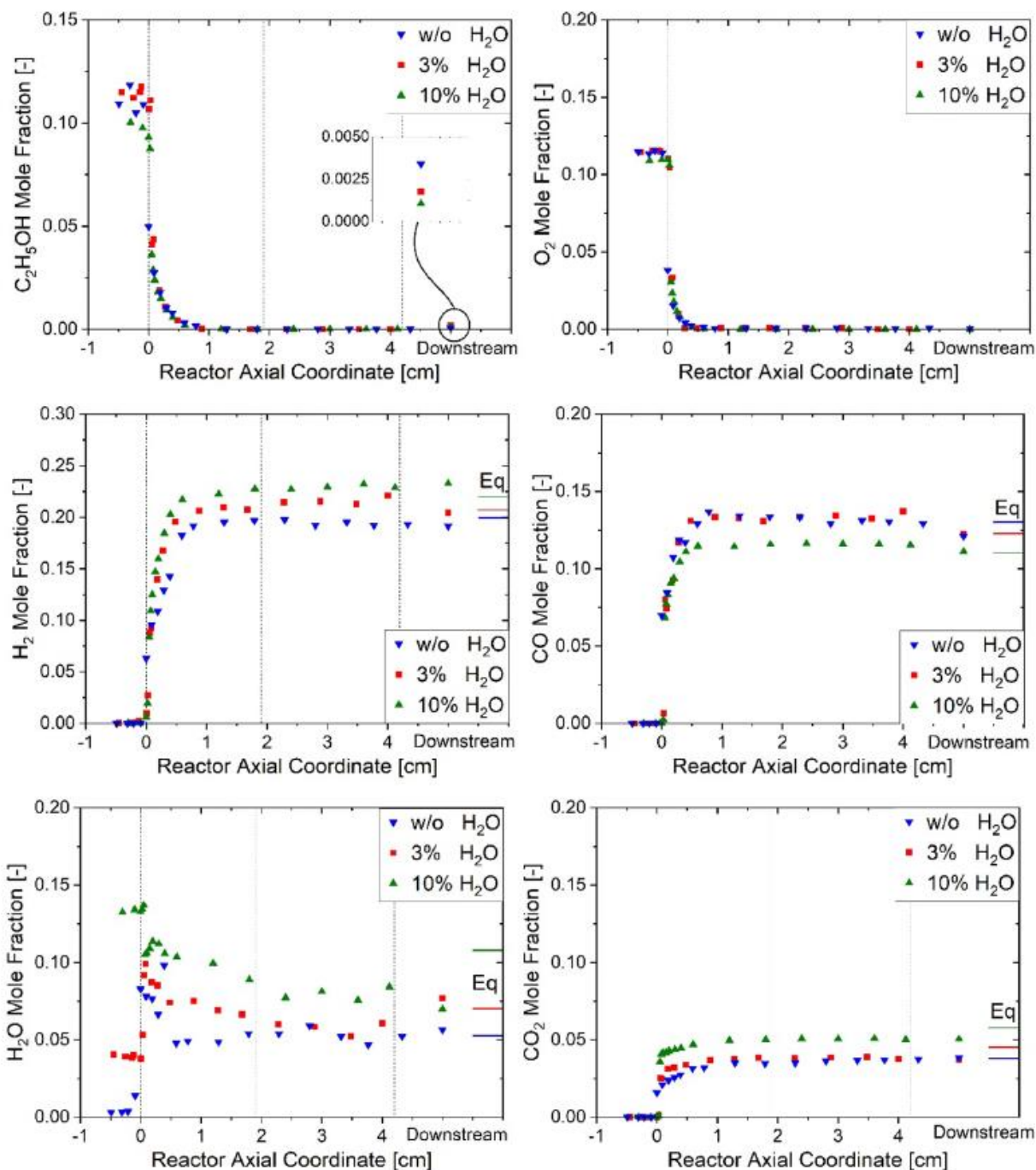
Figure 4.2 Concentration profiles for the CPO of C_2H_5OH with H_2O co-feed; C2H5OH = 11.2 %, C/O = 0.65, Tin = 100 °C, flow rate = 10NL/min [24].

In all cases, a notable concentration peak was observed at the initial part of the monolith channel, indicating the formation of by-products at the inlet of the reactor, which were subsequently rapidly consumed. This behaviour was reminiscent of findings from prior studies on propane, n-octane, and iso-octane catalytic partial oxidation. In those studies, the formation of hydrocarbon by-products was attributed to homogeneous reactions triggered by local temperature increases, followed by swift consumption via steam reforming on the catalyst surface. The present observations align closely

with this phenomenon and are consistent with previous research that associated the formation of these by-products with homogeneous reactions, although contributions from surface chemistry were not ruled out.

The production of acetaldehyde, methane, ethylene, and minor amounts of ethane during ethanol CPO can be attributed to noncatalytic oxidation and pyrolysis of ethanol. Additionally, the oxidative and acidic properties of the Rh/Al_2O_3 catalyst may contribute to the formation of by-products. For example, oxidative dehydrogenation might be responsible for acetaldehyde production, while the acidity of the Al_2O_3 support may catalyse ethanol dehydration, contributing to ethylene formation. Methane may arise in the first millimeters of the monolith through homogeneous cracking reactions of ethanol and acetaldehyde. Although the exact kinetic scheme and the relative roles of homogeneous and heterogeneous reactions are not fully understood, it is evident that all these species are rapidly consumed through steam reforming on the catalyst surface, ultimately converting into syngas. In the case of methane, the additional contribution of methanation reactions likely explains the non-zero concentrations measured at the end of the catalytic channel, consistent with previous studies involving other fuels.

Regarding the impact of water co-feed, as shown in Figure 4.2, it seems to have no significant effect on the molar fraction profiles of reactants C_2H_5OH and O_2. However, as the water concentration in the feed increases, there is a notable rise in H_2 concentration and a reduction in CO concentration. This change is likely associated with an increased extent of the water gas shift reaction, resulting in higher CO_2 concentration. Spatial profiles for H_2O reveal initial production in the oxidation zone, followed by gradual consumption downstream, leading to net H_2O production. However, in the case of a 10% H_2O co-feed, net consumption was observed.

The introduction of water co-feed appeared to limit the formation of certain by-products, potentially due to water ability to quench gas-phase reactions, reducing the production of these species, or promoting local reaction rates favouring syngas formation. While these species had only brief existence, their presence might influence the formation of carbon-containing species on the catalyst surface.
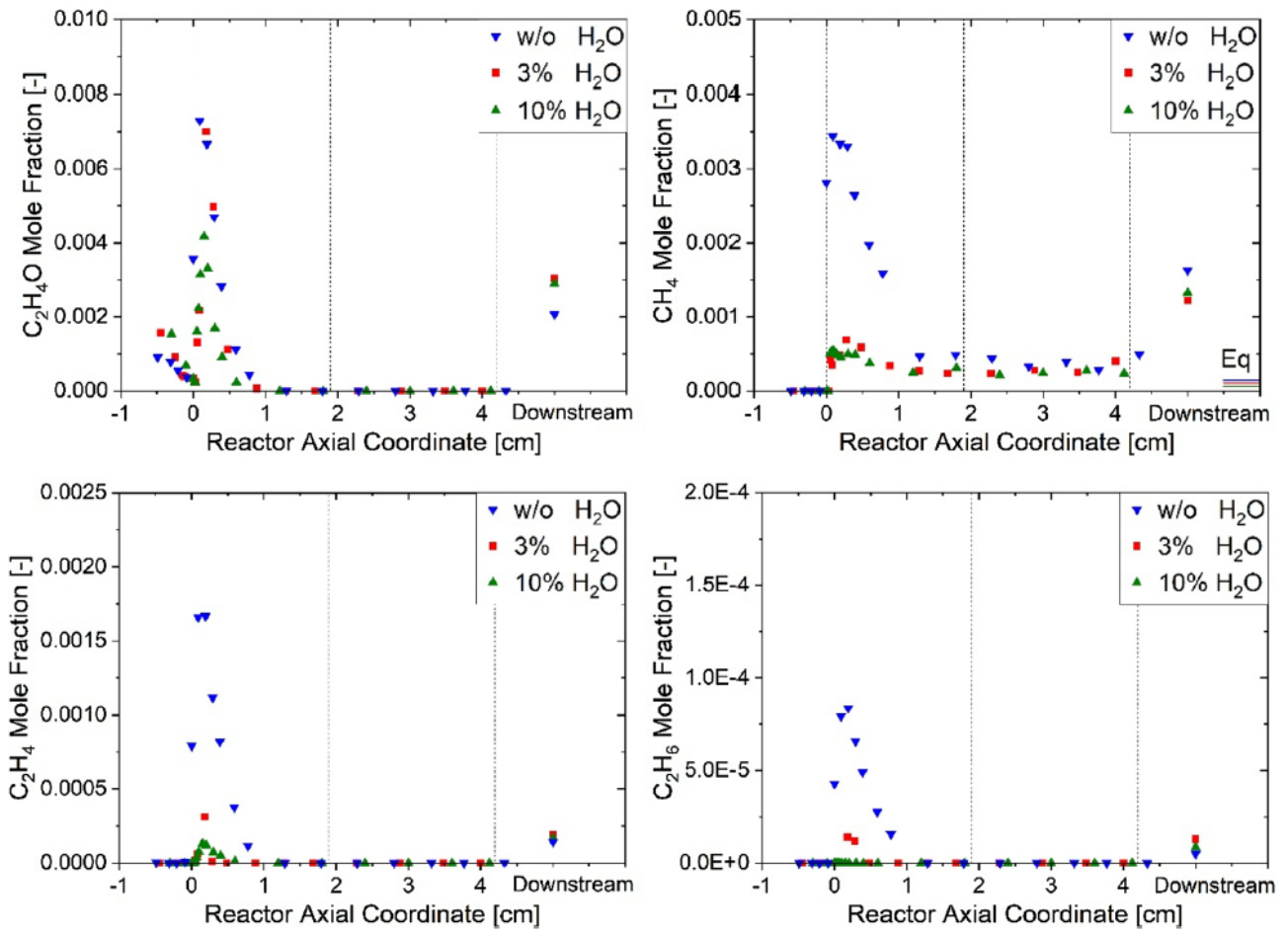
Figure 4.3 Concentration profiles for the CPO of C_2H_5OH with H_2O co-feed – Acetaldehyde and light hydrocarbons; C_2H_5OH = 11.2 %, C/O = 0.65, T_{in} = 100 °C, flow rate = 10NL/min [24].

4.2 Mathematical model

The features of the model, together with its equations and coefficients are presented in Chapter 2. This section focuses on the preliminary parametric analysis and the implementation of the hetero-homogeneous scheme - derived in Chapter 3 - prior to model validation.

4.2.1 Implementation of the hetero-homogeneous mechanism in the reactor model

In this section, the results of the comparison between data from an experimental campaign and the ones from simulations are reported, in order to validate the simulation tool.

As a first attempt, the heterogeneous and homogeneous schemes derived in Chapter 3 were implemented in the reactor model described in Section 2.3 in order to compare simulated results with experimental data.

The introduction of homogeneous kinetics into the model, as aforementioned, has been crucial to compare the cracking species that are formed and consumed during the reaction.

To check the impact of gas-phase reactivity, simulations by switching on and off the homogeneous scheme have been performed. Figure 4.4 shows the concentration profiles of the main reactants and products, with (solid lines) and without (dashed lines) homogeneous reactivity contribution, for a standard dry ethanol CPO test. The input conditions are here summarized:

- Pression: 1 atm;
- $T_{in, gas} = 100°C$;
- Feed concentrations: 11.2% of ethanol, C/O=0.65.

It is noticeable that by activating the homogeneous pathway, there is a faster consumption of ethanol (a), which is confirmed by a more rapid formation of CO (c) and H_2 (d). The trend for oxygen (b) is identical. Regarding CO_2 (e) and H_2O (f), the behaviour is consistent with that of the syngas products.

The model analysis reveals that gas-phase activation of ethanol is responsible for the formation of the hydrocarbon by-products (g-j) observed at the reactor inlet: they are formed in correspondence of the highest hot spot temperature and then show a plateau behaviour.
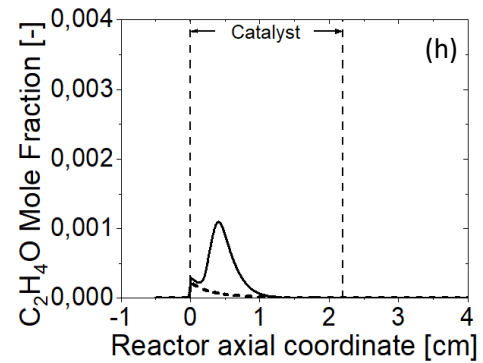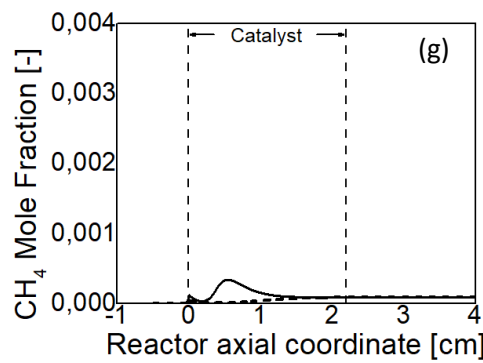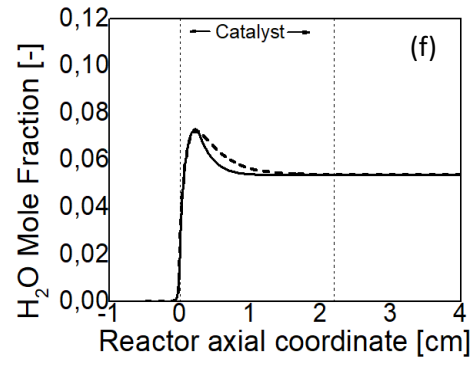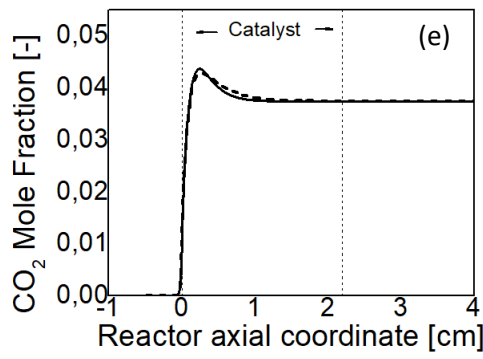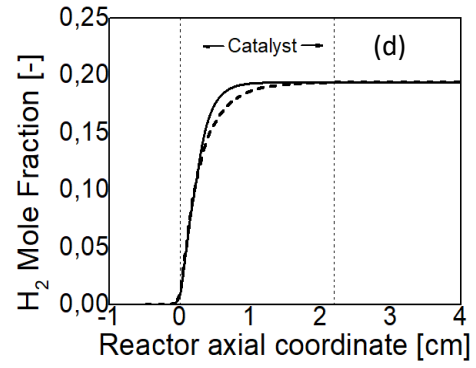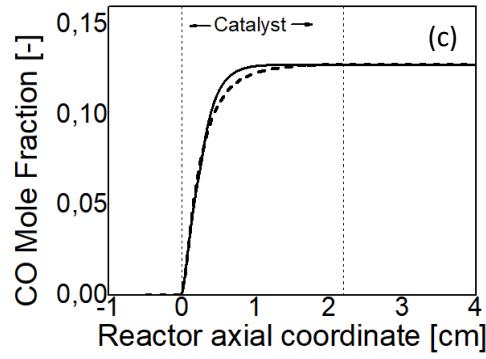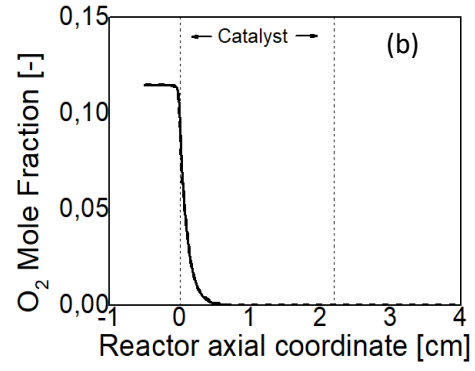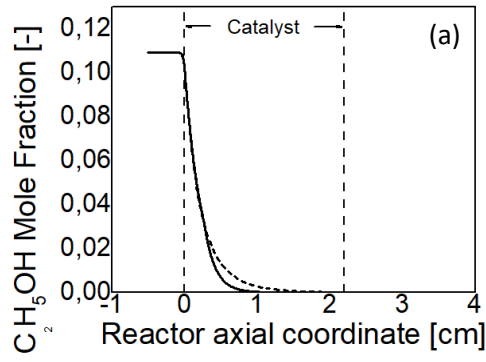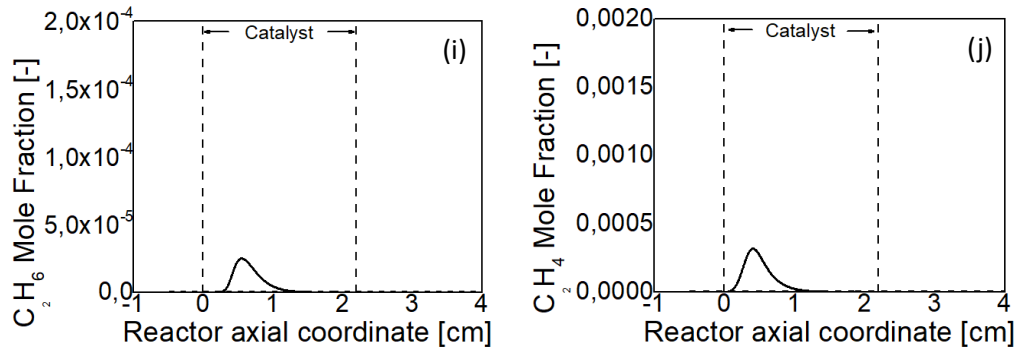
Figure 4.4 Concentration profiles for the CPO of C_2H_5OH without H_2O co-feed ; $C_2H_5OH = 11.2$ %, C/O = 0.65, $T_{in} = 100$ °C, flow rate = 10NL/min, with exclusion of homogeneous kinetics (dashed curve) and with inclusion of homogeneous kinetics (solid curve).

In order to account for the consumption observed experimentally in Figure 4.3 for ethane and ethylene - those species which present the maximum of mass fraction along the reactor axial coordinate higher than 10^{-3} when simulated with the original mechanism – the introduction of a catalytic consumption pathway via steam reforming was necessary, confirming a strong interplay between gas and solid phase reactivities.

As reported in Table 4.1, the rate laws introduced for the reforming of cracking species were formally alike that of ethanol steam reforming along the lines of [19]. It can be noticed that the rate law of methane steam reforming was homogenised to the other by-products with respect to the expression showed in Chapter 3.

Table 4.1 Heterogeneous reaction mechanism implemented in the model for cracking species

Reaction	Reaction rate r $[mol/g_{cat} \, s]$	$k_i^{873 \, K}$ $[mol/atm \, g_{cat} \, s]$	$E_{att}[kJ/mol]$
$C_xH_y + x \, H_2O \leftrightarrow x \, CO + (x + y/2) \, H_2$	$r_{SR_{C_xH_y}} = \dfrac{k_{SR_{C_xH_y}}P_{C_xH_y}(1 - \eta_{SR})}{1 + \dfrac{k_c P_{EtOH}}{P_{H2O}}}$	$4 \cdot 10^{-2}$	90
$CH_4 + H_2O \leftrightarrow CO + 3H_2$	r_{SR,CH_4} $= \dfrac{k_{SR,CH_4}P_{CH_4}\left(1 - \eta_{SR,CH_4}\right)}{1 + \dfrac{k_c P_{EtOH}}{P_{H2O}}}\sigma_{H_2O}$	$1.027 \cdot 10^{-1}$	92

where $K_c = 11.98 \exp\left[\frac{50}{R} \cdot \left(\frac{1}{T} - \frac{1}{T_0}\right)\right]$; x = 2; y = 4,6

Temperature dependence of kinetic constants was expressed with a modified Arrhenius form: $k(T) = k(T_{ref})\exp(-E_{act}/R(1/T - 1/T_{ref}))$. Terms $(1 - \eta_j)$ indicate equilibrium constraints, where η_j represents the ratio of the experimental reaction quotient $K_{p,j}$ and the thermodynamic equilibrium constant $K_{eq,j}$. Coefficients σ_i are needed to account for the extinction of the co-reactant: $\sigma_i = P_i/(P_i + 10^{-6})$.

4.2.2 Parametric analysis

Before addressing the analysis of the model results, it is important to note that the incorporation of the heterogeneous kinetics (referred to the Rhodium active surface) in the monolith model requires the introduction of a correcting factor, named α. In fact, the mass balances on the solid are related to the volume unit of the catalyst, while the net production rate of the i^{-th} species present in the mixture($\sum_{j=1}^{NR, \, het}\left(-\Delta H_{r,j}\right)r_j^{het}$) is referenced to the active Rh surface. It is therefore necessary to multiply the net production rate of the i^{-th} species by the parameter α, whose definition is reported in Table 2.2 of Chapter 2. This coefficient represents the active Rh surface per unit volume of the honeycomb monolith [m_{Rh}^2/m^3], and while converting the net production rate of the i^{-th} species into kmol/m^3/s, it also represents the theoretical activity of the catalyst. The parameter can be in principle estimated, based on geometrical and physico-chemical parameters of the washcoat (e.g., Rh dispersion); however, changes during the reactor operation cannot be excluded.

It is known that the high temperatures reached at the hot spot during tests of liquid fuel CPO are responsible for the catalyst activity loss due to sintering or the coalescence of Rh particles dispersed on the support [23]. Additionally, condensation/dehydrogenation reactions of adsorbed hydrocarbon species can lead to the formation of aromatic compounds and subsequent growth of carbon layers on the catalyst surface; olefins, in particular, are known to be precursors of coke. Homogeneous phase reactions can also lead to the formation of cracking species that result in soot formation, which can physically accumulate on the catalyst surface. All these phenomena described above may lead to catalyst deactivation, thus reducing the value of α.

For this reason, within this parameter, a multiplication factor, the activity coefficient η - dimensionless coefficient ranging from 0 to 1 - is added. The η allows adjusting the catalytic activity to simulate temperature and concentration profiles as the catalyst activity decreases due to deactivation phenomena.

A model analysis based on the tuning of the dispersion of the active phase γ - incorporated in the parameter α - was done. In Figure 4.5 the effect of the parametric analysis is observed on the thermal behaviour of the reactor: reducing Rh dispersion, steam reforming reactions work worse and slowly and hot spot temperatures increase. Moreover, a shift to right of maximum is visible, due to the superimposition between combustion and steam reforming reactions.
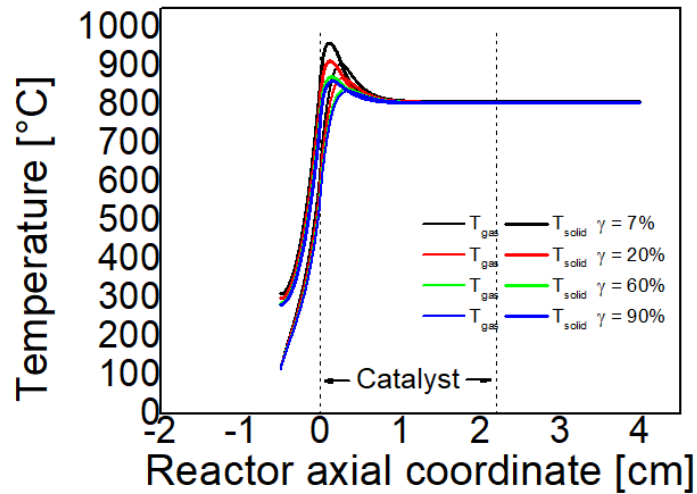
Figure 4.5 Effect of Rh dispersion on solid and gas phase temperature profiles for the CPO of C_2H_5OH without H_2O co-feed; C_2H_5OH = 11.2 %, C/O = 0.65, T_{in} = 100 °C, flow rate = 10NL/min. Thick lines refer to solid temperature, thin lines refer to gas temperature.

Figure 4.6 represents the concentration profiles of the reactants (panel a, b), syngas (c, d), and combustion species (e, f) obtained for the ethanol CPO reference test simulations for different values of dispersion. At decreasing Rh dispersion in the catalyst, the ethanol (panel a) is consumed less rapidly due to slower fuel conversion. Notice that the conversion of O_2 is not influenced by the Rh dispersion or temperature profile developed on the catalyst and it is complete after 0.6 cm. This happens because the rate of the combustion reaction is limited by O_2 external mass transfer.

The concentration profiles of CO and H_2 (panel c,d) reflect the effect of dispersion on the rate of fuel consumption: at reducing dispersion, steam reforming works worse and so there is less syngas produced at the same coordinate (reaction is faster).

By diminishing Rh dispersion, the concentration of CO_2 (panel e) reaches the thermodynamic equilibrium at a higher axial coordinate, due to the slower reaction rates involved in the process.

H_2O concentration profile (panel f) presents a maximum - due mainly to hydrogen combustion – that increases by reducing the Rh dispersion.
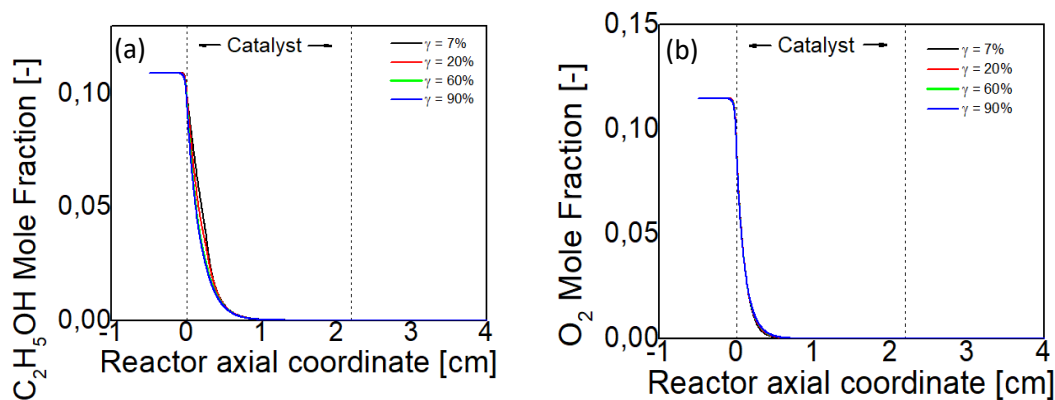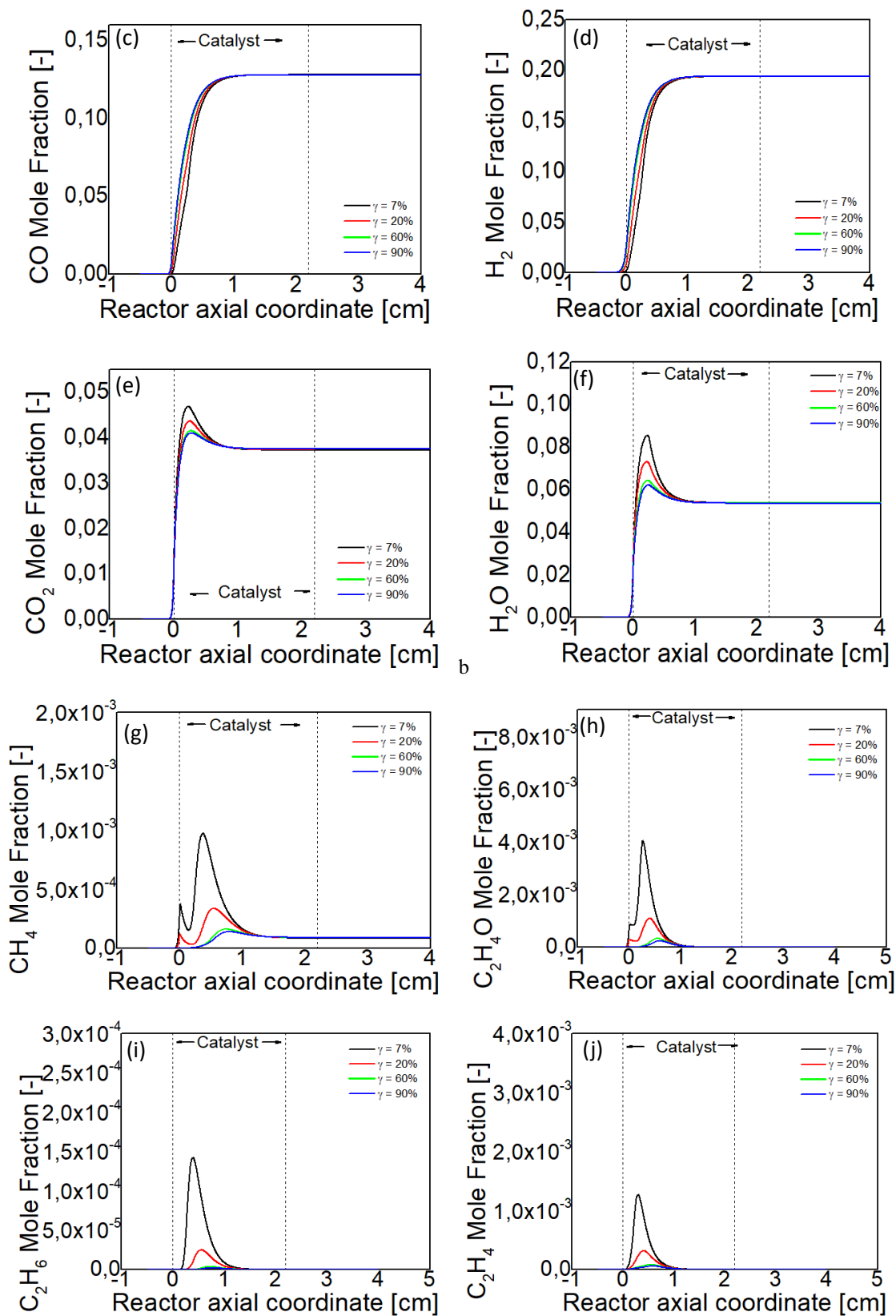
Figure 4.6 Effect of Rh dispersion on the concentration profiles for the CPO of C_2H_5OH without H_2O co-feed; C_2H_5OH = 11.2 %, C/O = 0.65, T_{in} = 100 °C, flow rate = 10NL/min.

During the course of the experimental campaign conducted on the catalytic monolith, clear evidence of catalyst deactivation phenomena was observed. As a consequence, performing intermediary methane CPO tests represented a recommended approach to monitor the catalyst activity and deduce a deactivation factor, which is directly incorporated in the volumetric specific surface area α in the model equations. In the endeavour to attain a match between the observed thermal profiles and the calculated ones for CH_4 CPO, an attenuation of catalyst activity by adjustment of activity factors was indispensable. In particular, the presence of two activity factors for each test was highlighted, attributable to the portioning of the catalyst in two zones: one dedicated to oxy-reforming (initial 5 mm) and the other to reforming [23], each of which subjected to different deactivation phenomena.

In the tuning of the modelling parameters, an optimal compromise was obtained by introducing activity factors in a ratio 0.2 between the primary and the secondary section of the monolith.

4.3 Reactor simulation

In this section, the comparison of the model prediction against the experimental data of a reference dry ethanol CPO test is reported. The strategy of a different activity factor in the oxy-reforming and in the reforming section was adopted.

4.3.1 Thermal behaviour of ethanol CPO

In figure 4.7, temperature profiles simulated with the model (panel a) and the experimental ones (panel b) obtained in the same operative conditions are reported.
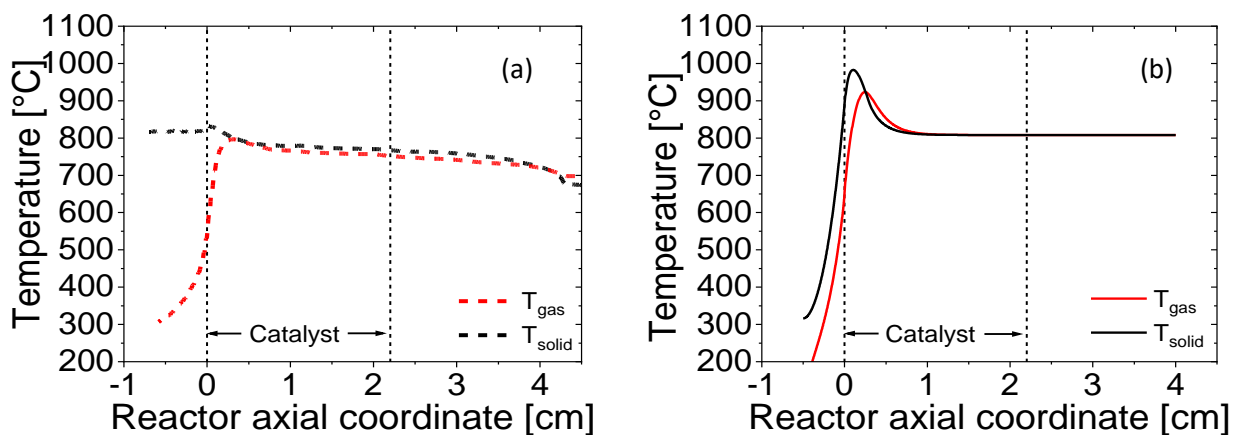
Figure 4.7 Panels (a) and (b) represent gas-phase and solid-phase temperatures as a function of the axial coordinate. Dashed lines indicate experimental results, lines represent model simulations.

It is observed how the temperature values of the gas phase and the solid phase, exiting the monolith, are practically identical, showing that the model follows thermodynamic equilibrium and that the experimental test considered is close to this result.

Experimental data (panel a) and calculated (panel b) temperature profiles show some lack of agreement that can be attributed to the not perfect adiabaticity of the lab-scale reactor; on purpose, axial thermal dispersion is allowed at the beginning of the catalyst in order to prevent the overheating and thus limit the deactivation. Nevertheless, for the surface temperature a hot spot can be detected at the catalyst entrance (axial coordinate ≈ 5 mm).

In conclusion, it is found that the model used is an acceptable predictive tool for experimental thermal behaviour. This is a starting point for subsequently comparing the concentration profiles of different species.

4.3.2 Axial evolution of the reacting species

The peak in the temperature profile noticed at the catalyst entrance corresponds to the fast consumption of oxygen that occurs under full mass transfer control, as showed in Figure 4.2 (a) by the model wall concentration dropping to zero at beginning of the monolith.

Ethanol consumption – reported in Figure 4.8 (a) as well, proceeds instead by combination of total oxidation and steam reforming, along a more extended length (about 10 mm), the oxy-reforming zone. Figure 4.8 (b) shows the axial profiles of the main products: the oxidative reactions involving ethanol, H_2 and CO are responsible for the observed peak of H_2O and the step increase of CO_2 concentration, while the onset of reforming reactions at the very catalyst entrance justifies the sudden increase of H_2 and CO concentration. Downstream in the catalytic bed, where oxygen is totally converted, reforming reactions contribute to lower the temperature and increase syngas productivity.
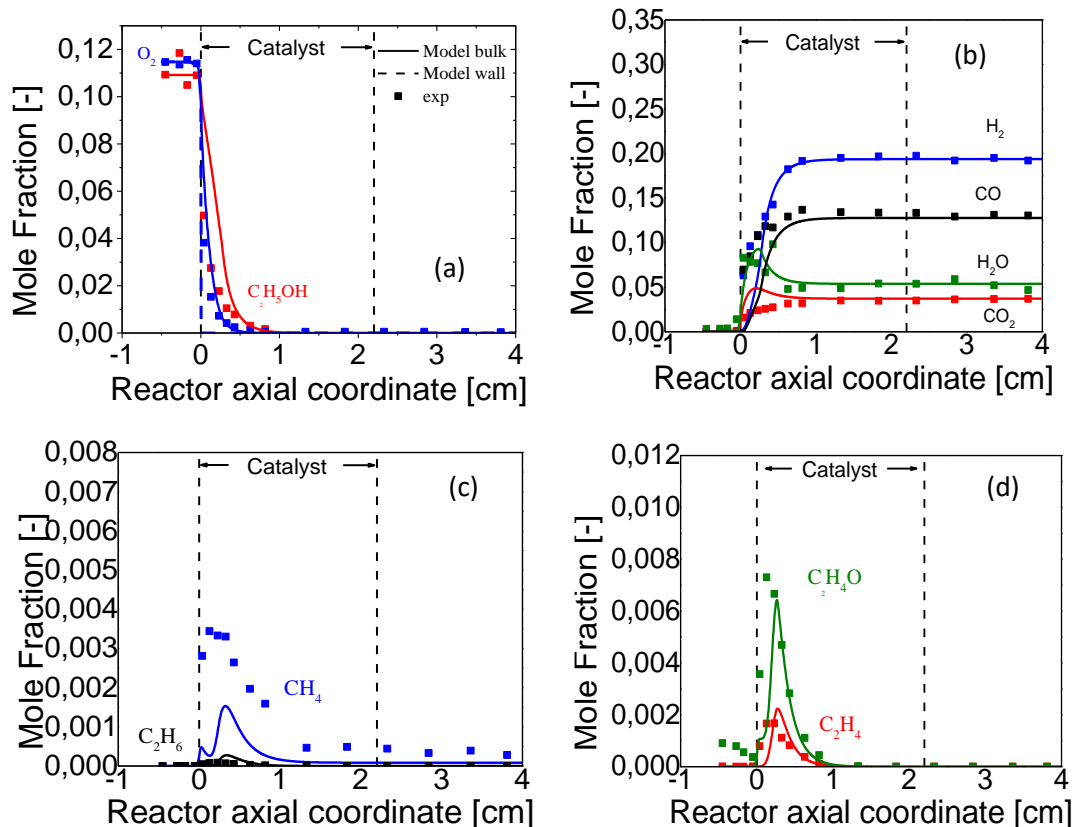
Figure 4.8 Panels a to d illustrate reactants (a) and main products (b-d) mole fractions along the axis of the reactor. Experiments are expressed in symbols, modelling results are represented by lines.

The axial profiles of molar fractions of the by-products of cracking reactions are displayed in figure 4.2 (c) –(d).

All the by-products are present in small concentrations and show a complex evolution.

The formation of methane starts at the beginning of the catalyst, passing through a maximum within the first millimiters of the catalytic channel, followed by a drop in molar fraction and another rise. A similar formation pattern for methane was observed for the CPO of propane [118], characterised by gas-phase formation, heterogeneous consumption by steam reforming and subsequent formation by solid-phase ethanol decomposition. Ethylene molar fraction increases inside the catalytic channel by following the gas-phase dehydration of the main reactant. After reaching the maximum, its consumption is well-described through the introduction of the aforementioned steam reforming pathway, resulting in no detection of the species among the products.

The trend of acetaldehyde is predicted by the model as a result of formation through oxidative dehydrogenation of ethanol and consumption through solid phase steam reforming.

4.4 Effect of water

The model simulation tool was adopted to predict the effect of water co-feed on ethanol CPO: simulations were performed at the same operating conditions of the experiments presented in section 4.1:

C_2H_5OH = 11.2%, C/O=0.65, H_2O co-feed (0-3-10 %), N_2 to balance, T_{in}=100 °C, flow rate =10 Nl/min.
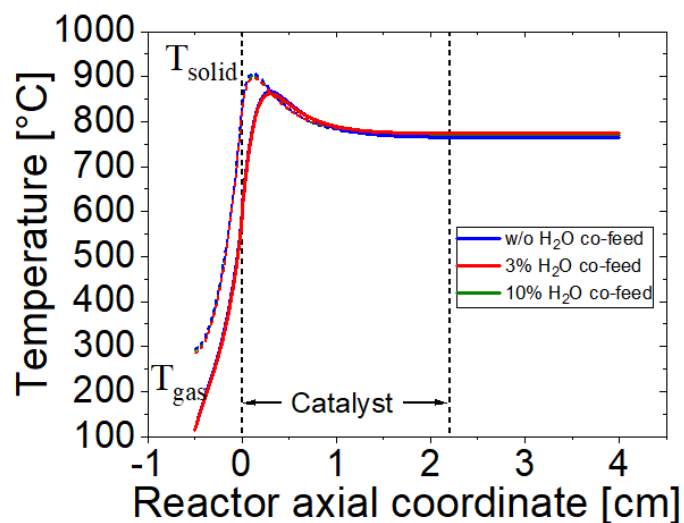
Figure 4.9 Temperature profiles for the CPO of C_2H_5OH with H_2O co-feed; C_2H_5OH = 11.2 %, C/O = 0.65, T_{in} = 100 °C, flow rate = 10NL/min.

The trends of the thermal profiles predicted by the model are in agreement with the experimental observations reported in Section 4.1: no effect of water is highlighted and the profiles of both solid ang gas phase temperatures completely overlap.

In Figure 4.10 the calculated concentration profiles of the species considered in the homo-heterogeneous scheme are plotted.
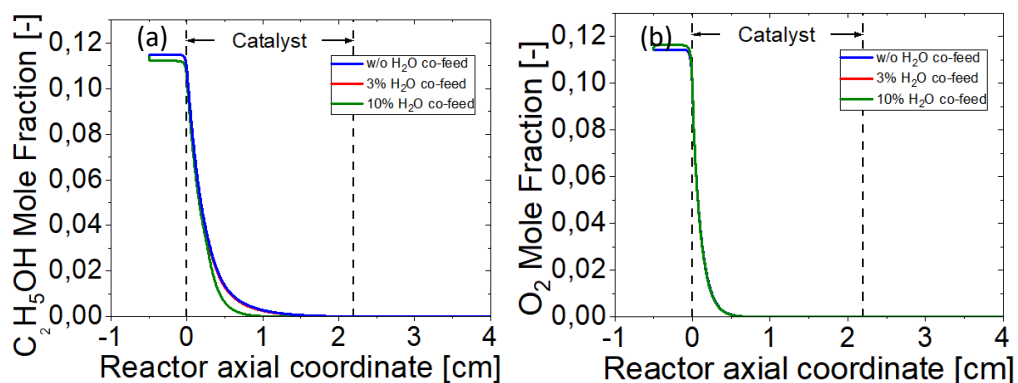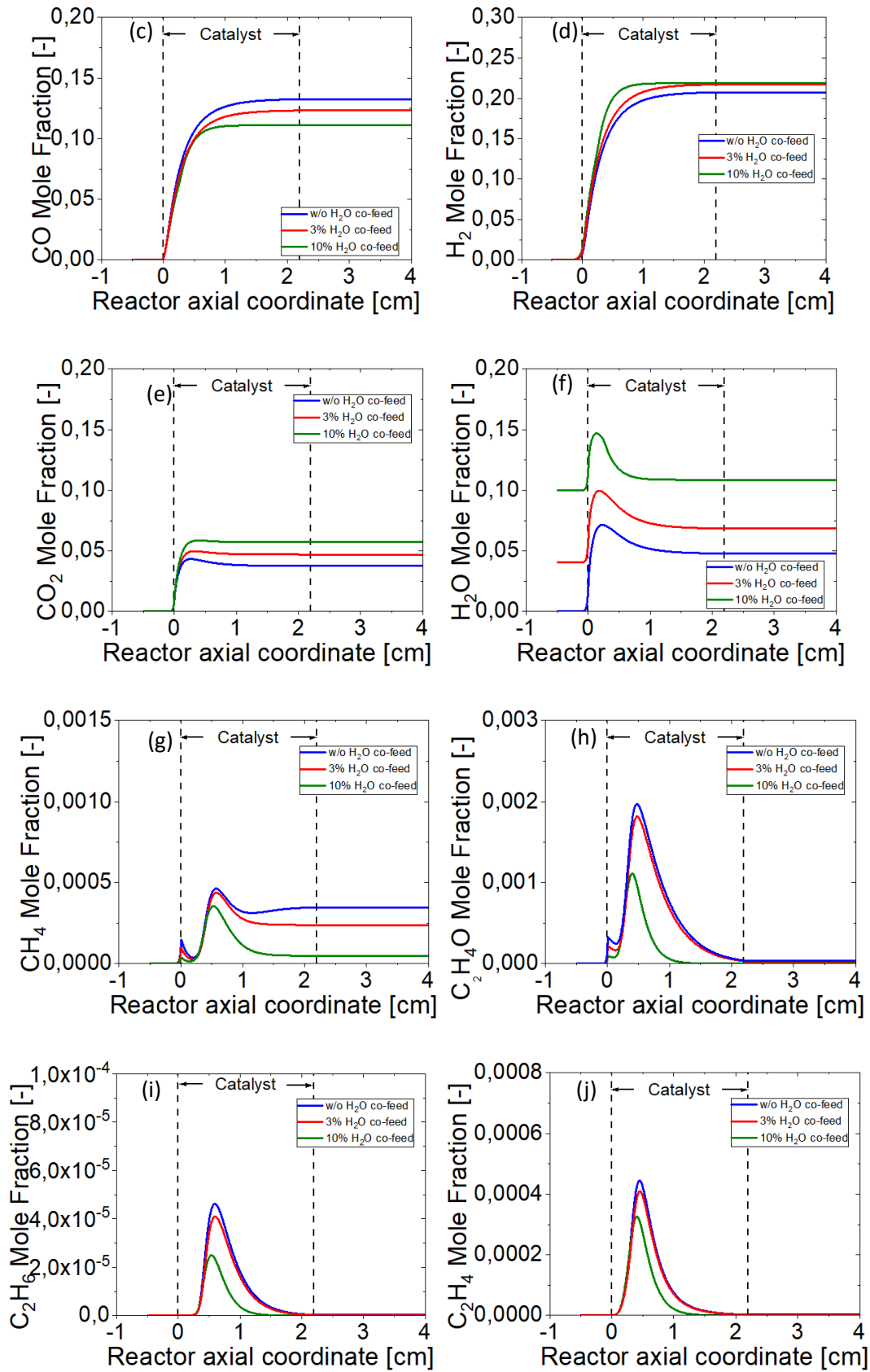
Figure 4.10 Concentration profiles for the CPO of C_2H_5OH with H_2O co-feed; C_2H_5OH = 11.2 %, C/O = 0.65, T_{in} = 100 °C, flow rate = 10NL/min.

Also in this case, simulations are coherent with the results of the experimental campaign: the water co-feed enhances hydrogen production and discourages the production of coke precursors. With respect to these, it can be noticed that the model predicts a less pronounced effect between dry conditions and those with 3% water co-feed.

To sum up, the study reported in this chapter lends robustness to a modelling tool capable to describe simultaneously transport phenomena, gas-phase reactivity, and solid-phase reactivity for ethanol catalytic partial oxidation. It is plausible that the complexity of the experimental activity and the reactivity framework may have hindered a deep understanding of certain phenomenological details that require further investigations in the future.

5. Low temperature oxidation of methane over Pd-based catalysts: new insights on the axial evolution of methane consumption rate through the spatially-resolved sampling technique

The use of bio- and e-CH_4 as transportation fuel can contribute to the decarbonization of the heavy-duty transportation sector. However, the presence of unburnt CH_4 in the exhaust is highly undesired due to its powerful greenhouse gas effect. Three-way-catalysts with Pd/PdO are needed to remove the highly polluting CH_4 emissions [43], [44], [46]. It has been reported that working in slight defect of oxygen brings to optimal performance for simultaneous CO and CH_4 conversion in NG three-way catalysts (TWC) operations. Moreover, dithering operations exhibit higher CH_4 conversion and more stable performances compared to constant lambda operations [49]. These results have been justified with the presence of a more active metallic Pd/PdO state [52]. However, the catalytic CH_4 oxidation mechanism and kinetics on supported Pd are complex and still under debate. In this study, $CH_4/CO/H_2$ oxidation was studied over a commercial monolithic catalyst and insight was gained in the kinetics of CH_4 oxidation over Pd/PdO using the axially resolved sampling technique.

5.1 Catalyst pretreatment

Prior to the experimental campaign, each monolithic sample underwent a degreening treatment in a stoichiometric flow mixture ($\lambda = 1$, $O_2 = 0.65$ %) at 600 °C for 5 hours. After degreening, the catalyst underwent a conditioning treatment with the purpose to activate and stabilize the honeycomb methane conversion performances. The treatment consisted in periodically switching the feed from a lean ($\lambda = 1.02$, $O_2 = 1.03$%) to a rich condition ($\lambda = 0.98$, $O_2 = 0.26$ %) at $T_{oven} = 450$ °C - so to force palladium undergoing to reduction/re-oxidation cycles [54].

By means of continuous mass spectrometer analyses of the outlet gas composition CH_4 conversion increased from 35% to 95% upon 15 rich/lean cycles. Such a marked enhancement of the pulses on catalyst activity could be attributed to the weakening of the Pd-support interactions, which are likely to stabilize the oxidized Pd particles against reduction[119].

5.2 Catalyst stability

As a preliminary effect, the stability of the catalyst performance was investigated. Stability is in fact a prerequisite to obtaining kinetically informative data from the axially resolved sampling

technique. Integral conversion measurements were monitored during a time span of 6 hours, representative of the time required for collecting a fully resolved axial concentration profile, at three different lambda values; the results are reported in Figure 5.1(a). At λ=0.99, the monolith performance was stable; at λ=0.9975 (when the O_2 content was slightly below the stoichiometric value) a moderate deactivation was observed. At $\lambda = 1.02$ (thus in lean conditions, with inlet O_2 content of 1.03 %), a strong decline of methane conversion was visible; during the activity decay, an axial measurement of composition was taken, and the results are reported in Figure 5.1 (c).

A periodic rich pulse technique developed in previous studies [54], [119] was then introduced with the aim of maintaining a stable CH_4 downstream conversion throughout the test duration: specifically, periodic 40-second-long rich pulses ($\lambda = 0.98$, $O_2 = 0.26$ %) were performed every 12 minutes, i.e., right before each step movement of the capillary probe. During such rich pulses palladium underwent a quick reduction, followed by reoxidation occurring when lean conditions were restored.

A more detailed description of the phenomena observed during a rich pulse is given in Appendix, section A.2.

The periodical redox cycle of palladium particles resulted in a stable downstream methane conversion, as clearly demonstrated by the outlet conversion measurements in Figure 5.1(b). During this experiment, the reacting mixture was sampled from the back to the inlet of the monolith channel and the measured axial conversion profile is reported in panel 5.1(c). The comparison between data collected with and without periodic pulses allows to appreciate the effect of the decaying activity in the absence of periodic regeneration pulses; in particular, considering the backward direction of the axial sampling procedure, deactivation resulted in progressively diverging conversions from the back end to the front end of the catalyst [120].
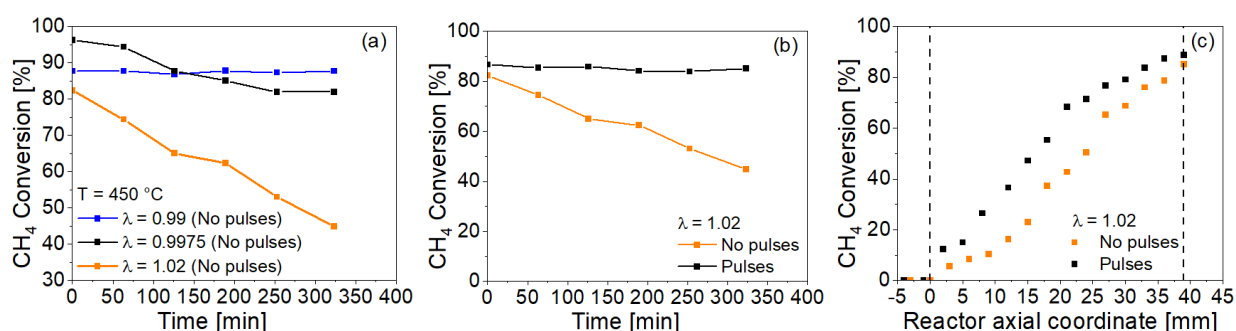
Figure 5.1 (a) CH_4 downstream conversion for $\lambda = 0.99$ (blue symbols and line) and $\lambda = 1.02$ (orange symbols and line) without pulses; (b) Downstream time evolution and (c) axially resolved profiles of CH_4 conversion for $\lambda = 1.02$ with periodic pulses (black symbols and line) and under conditions of progressive activity decay (orange symbols and line) at T 450 °C.

In the literature there is a certain degree of agreement on the predominant role of water in Pd-based

catalysts deactivation [50], [51], [53]. However, various possible explanations for activity losses under lean conditions have been suggested, like the formation of stable palladium hydroxide [121] or a decrease of active surface due to PdO layers smoothening [122]. Since activity losses are recovered after a reducing pulse and the subsequent reoxidation, sintering phenomena could be ruled out.

A detailed description of the experimental methods, catalyst features and operating conditions is given in Chapter 2 (section 2.2.3), while Table 5.1 shows the feeding conditions of every test reported in this chapter.

Table 5.1 Testing conditions of the experiments.

λ	S					y_i [vol. %]					
		T [°C]	CH_4	H_2	CO	H_2O	O_2	CO_2	N_2	Pulses
1.02	1.57	450	0.15	0.1	0.6	10	1.03	10.7	Balance	YES
1	1	450	0.15	0.1	0.6	10	0.65	10.7	Balance	YES
1.01	1.29	450	0.15	0.1	0.6	10	0.84	10.7	Balance	YES
0.9963	0.89	450	0.15	0.1	0.6	10	0.58	10.7	Balance	YES
0.99	0.71	450	0.15	0.1	0.6	10	0.46	10.7	Balance	NO
0.9925	0.78	450	0.15	0.1	0.6	10	0.51	10.7	Balance	NO
0.9975	0.93	450	0.15	0.1	0.6	10	0.60	10.7	Balance	YES
0.995	0.85	450	0.15	0.1	0.6	10	0.55	10.7	Balance	NO
1.02	1.57	400	0.15	0.1	0.6	10	1.03	10.7	Balance	YES
1.01	1.29	400	0.15	0.1	0.6	10	0.84	10.7	Balance	YES
1	1	400	0.15	0.1	0.6	10	0.65	10.7	Balance	YES
0.9925	0.78	400	0.15	0.1	0.6	10	0.51	10.7	Balance	NO
0.995	0.85	400	0.15	0.1	0.6	10	0.55	10.7	Balance	NO
0.9975	0.93	400	0.15	0.1	0.6	10	0.60	10.7	Balance	YES
0.9963	0.89	400	0.15	0.1	0.6	10	0.58	10.7	Balance	YES
0.99	0.71	400	0.15	0.1	0.6	10	0.46	10.7	Balance	NO
0.99	0.71	400	0.15	0.1	0.6	2	0.46	10.7	Balance	NO

5.3 Integral effect of lambda

The initial activity data reported in Figure 5.1 (a) show that methane conversion presents a complex dependence on lambda, characterized by the presence of a maximum at $\lambda=0.9975$. The effect of O_2 feed content was investigated more deeply, by performing an extensive characterization of the integral response of the monolith to lambda and by performing axially resolved measurements under selected feed conditions.

Figure 5.2 shows the measured methane conversion and hydrogen outlet concentration during the experimental campaigns at varying λ at $T=400, 425$ and $450°C$.

Both at 425 and 450 °C methane conversion reaches a maximum for slightly rich lambda values ($\lambda=0.9975$). A different trend was found at 400 °C: at decreasing O_2 excess, CH_4 conversion decreases and shows a minimum where the rich window is entered, while an increase is observed when moving further into the rich region. The behaviour observed at 400°C is in good agreement with results reported in [64].

Concerning the product composition, at all the temperatures, the net production of H_2 is null in the lean region, but progressively grows when proceeding in the rich region.
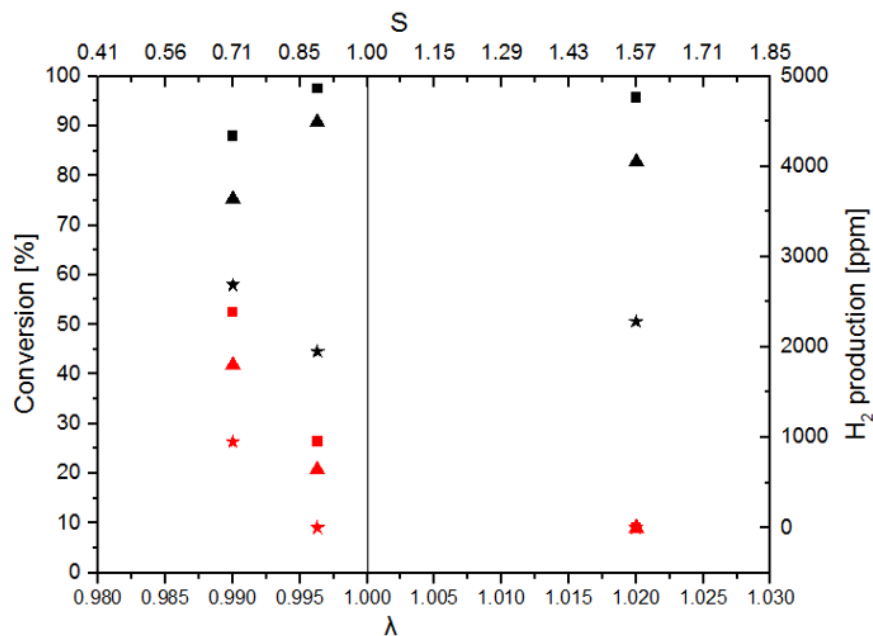
Figure 5.2 CH_4 conversion (black symbols) and H_2 concentration (red symbols) trends for various λ at $T = 450 °C$ (squares), $T = 425°C$ (triangles) and $T = 400 °C$ (stars) under stable downstream conditions.

To gain insight in the effects of temperature and lambda on the evolving kinetic regimes across the monolith and capture with precision the conditions and intensity of phenomena, which can hardly

be inferred only based on integral data, spatially resolved concentration and temperature profiles were collected during working conditions; these were selected based on their representativeness, either for application or for the kinetic relevance.

5.4 Axially resolved effect of lambda

A set of experiments was performed at the furnace temperature of 450°C and at three significative values of lambda: lean (λ =1.02, O_2 =1.03%), rich (λ =0.99, O_2 = 0.46%) and slightly rich (λ = 0.9963, O_2 = 0.58 %). Figure 5.3 reports the measured axial profile concentration of CH_4, O_2, H_2 and CO.

At λ =1.02 all reactants follow a monotonic decreasing trend. However, while H_2 (Panel c) and CO (Panel d) are rapidly consumed in the monolith entry zone reaching complete conversion after 3 mm and 10 mm from the entrance, respectively, CH_4 (panel a) exhibits a more gradual decrease all along the catalyst length reaching about 85% conversion at the catalyst outlet. Simulation results in Figure A.1.1. in Appendix show that the experimental profiles of CO and H_2 are consistent with a complete external mass transfer control of their oxidation kinetics under the investigated conditions. O_2 concentration (panel b) rapidly decreases in the entry region, consistently with H_2 and CO combustion stoichiometry, then declines more gradually due to the slow oxidation of CH_4 across the rest of the monolith length.

Profiles obtained under fully rich conditions (λ = 0.99) show different trends from the lean ones except for the initial decrease of H_2 and CO, which perfectly overlaps the profiles collected at λ =1.02. H_2 reaches complete conversion at 3 mm from the entrance, then its concentration starts increasing from x=5 mm, which is almost coincident with complete O_2 consumption occurring at x=6 mm. At this position also CO molar fraction trend starts deviating from the one obtained under lean conditions, never reaching complete conversion and slightly increasing in the following part of the honeycomb catalyst. The observed trends are consistent with the onset of steam reforming and water gas shift reactions upon complete O_2 consumption, the presence of H_2 slightly upstream O_2 depletion being likely due to back-diffusion phenomena. Noteworthy in the entry region before complete O_2 consumption the CH_4 consumption rate is markedly higher than that observed under lean conditions. Such a rate enhancement is responsible for the rapid achievement of full O_2 consumption, H_2 and CO oxidation being stoichiometrically responsible for a maximum 76% O_2 conversion at λ =0.99. Downstream the complete O_2 depletion, CH_4 is further consumed at gradually decreasing rate due to steam reforming, reaching almost 90% conversion at the reactor

outlet. It is worth remarking that the presence of H_2 in the downstream region clearly indicates that therein Pd is in the reduced state since temperature is well above the threshold reported for PdO reduction in H_2 containing atmosphere [123]–[125]. At $\lambda = 0.9963$, while H_2 and CO profiles in the inlet region perfectly overlap those obtained at $\lambda = 1.02$, spatially resolved data highlight three different regimes of methane consumption rate: i) in the first section of the catalyst, up to x = 16 mm, CH_4 is consumed at a slower rate than that observed at $\lambda = 1.02$, consistently with a slightly positive order of CH_4 oxidation rate with respect to O_2 [126]; ii) from x = 16 mm a sharp increase of CH_4 consumption rate is observed until oxygen is completely consumed at x = 20 mm; iii) downstream complete O_2 depletion methane is further consumed to almost complete conversion due to steam reforming as evidenced by the parallel increase of H_2 concentration.
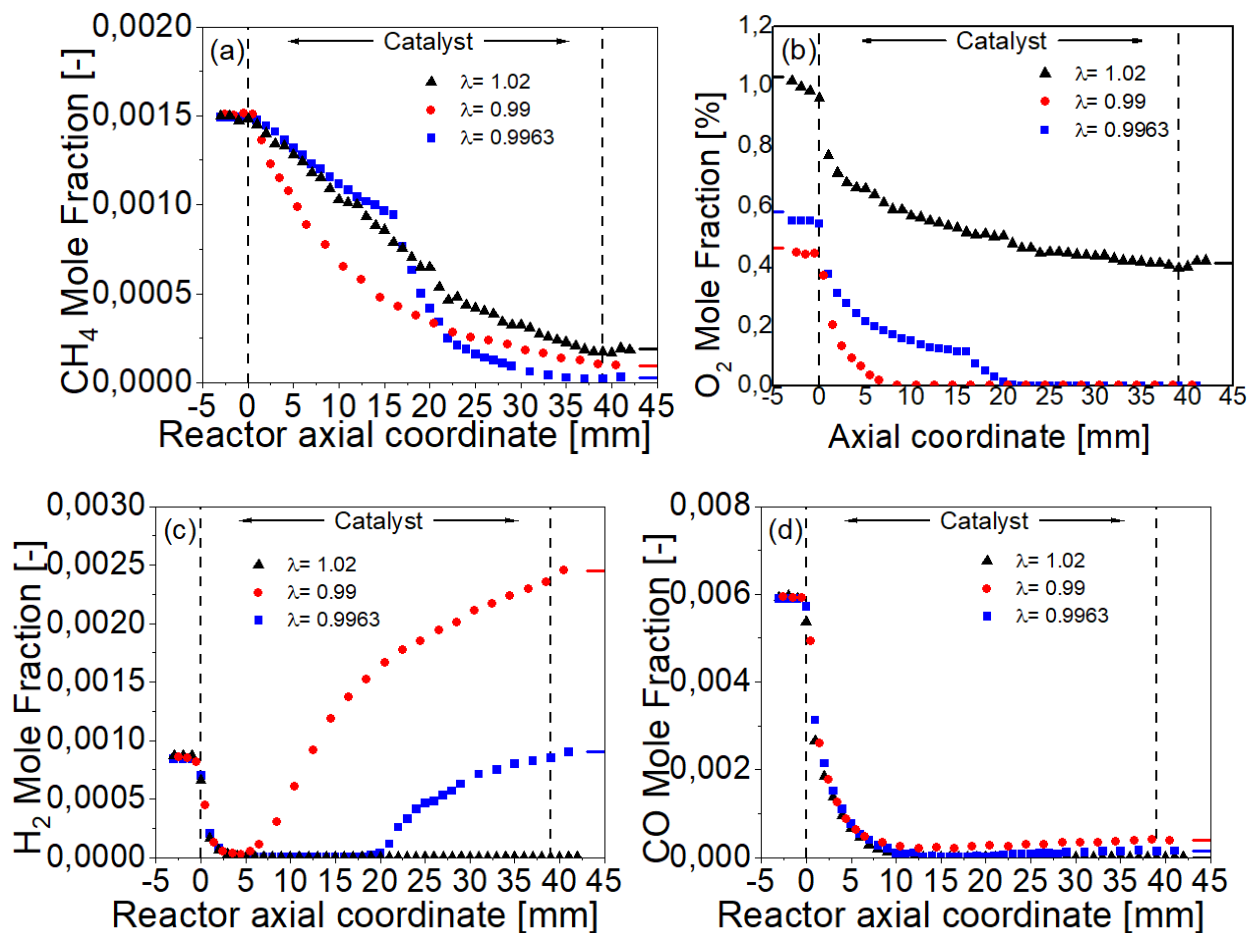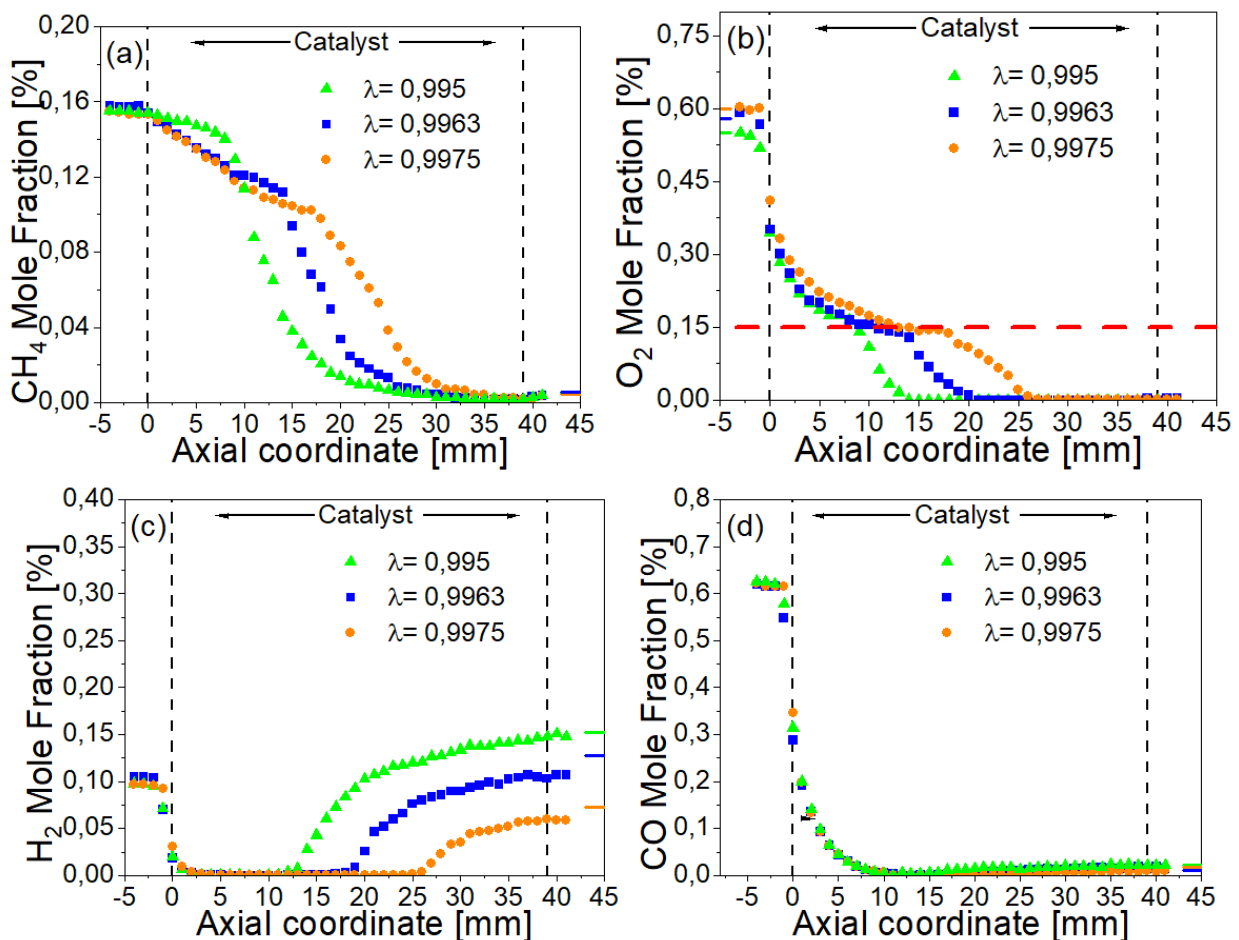

Figure 5.3 Concentration profiles for the oxidation of a mixture of 0.15 vol.% CH_4, 0.6 vol.% CO, 0.1 vol.% H_2, 10.7 vol.% CO_2, 10 vol.% H_2O for different O_2 co-feed (0.46 - 1.03 vol.%); T = 450 °C, GHSV = 50000 h^{-1}.

Figure 5.4 shows the measured temperature profiles under the three reacting conditions. The axial profile measured at the same flow rate with inert N_2 is also reported for the sake of comparison. The thermal behaviour is consistent with the observed concentration profiles. In the very first millimetres of the catalyst, the temperature increases rapidly in all reaction tests mainly due to the

very fast CO and H_2 oxidation. Notably, the combustion of hydrogen and carbon monoxide would result in an adiabatic temperature rise of about 60 °C. This is in quite good agreement with the results obtained and suggests that H_2 and CO oxidations release heat faster than the reactor can dissipate it. After the entrance zone temperature profiles are driven by the balance between thermal effects of CH_4 consumption and heat dissipation from the reactor. As a results temperature keeps almost flat at 460°C in the λ =1.02 test where the heat release due to slow CH_4 oxidation is compensated by heat dissipation. At λ =0.99 temperature gradually decreases down to 445°C due to the onset of endothermic steam reforming. Temperature profile at λ = 0.9963 show an intermediate behaviour with a remarkable bump in correspondence with the zone where the faster CH_4 oxidation is observed.

Finally, it worth nothing that after the initial rise, temperatures keep reasonably close to the nominal value (Toven=450°C). Accordingly major temperature effects on the observed trends of CH_4 consumption rate can be excluded.
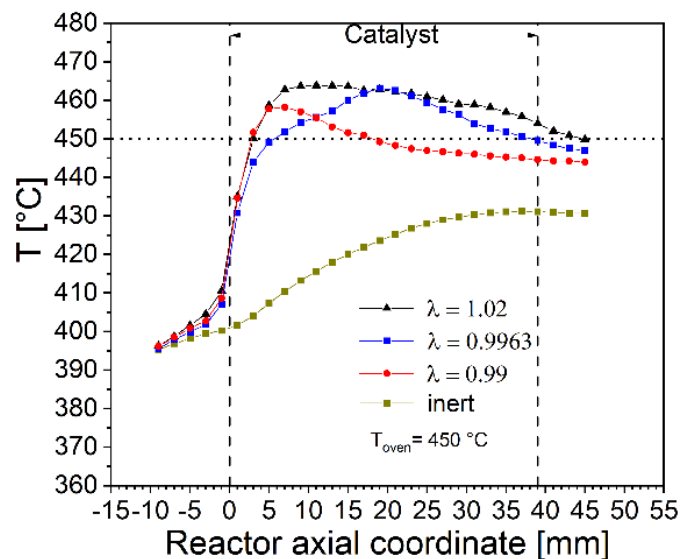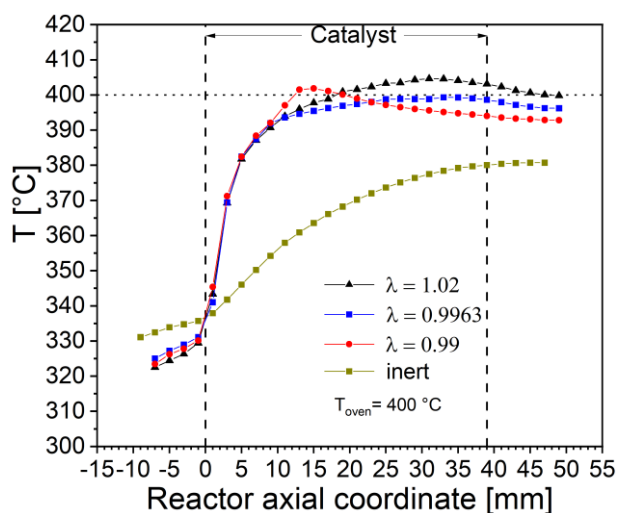

Figure 5.4 Temperature profiles for the oxidation of a mixture of 0.15 vol.% CH_4, 0.6 vol.% CO, 0.1 vol.% H_2, 10.7 vol.% CO_2, 10 vol.% H_2O for different O_2 co-feed (0.46 - 1.03 vol.%); T = 450 °C, GHSV = 50000 h^{-1}.

To gain insight on the peculiar CH_4 oxidation behaviour the spectrum of investigated lambda was then focused to a narrow window of slightly rich conditions: Figure 5.5 shows the comparison between the experimental data collected for λ =0.9963 (O_2=0.58%) with those obtained in the same conditions for slightly leaner (λ =0.9975, O_2=0.6%) and richer (λ =0.995, O_2=0.55%) compositions. The presence of the characteristic three regimes trend of methane consumption (slow oxidation, fast oxidation, steam reforming) is evident for all the investigated conditions. However, while H_2 and CO inlet consumption profiles are perfectly overlapped, the position where transition from slow to fast CH_4 oxidation occurs is rather sensitive to λ, significantly shifting downstream for small

increase of inlet O_2. A careful inspection of O_2 concentration profiles (Figure 5.5 (b)) shows that a common threshold exists at which the rate of oxygen and methane consumption abruptly increases. Such a threshold, graphically represented by a red dashed line in panel 5.5 (b), is at O_2=0.15%. The threshold line inserted at the position where a sort of inflection point of the curve is identified, detected where the computed second derivatives of the curves go to zero.

Since the reactor operates at atmospheric pressure conditions, the corresponding oxygen partial pressure is approximately 1.5 mbar.

It is worth noting that in the test at λ =0.99 (Figure 5.3) such a threshold was immediately achieved at the surface due to H_2 and CO consumption under full external mass transfer control, which is likely the reason for the observed enhancement of CH4 consumption rate at the very inlet of the honeycomb catalyst (Figure 5.5 (a)).

Figure 5.5 Concentration profiles (panels a-d) for the oxidation of a mixture of 0.15 vol.% CH_4, 0.6 vol.% CO, 0.1 vol.% H_2, 10.7 vol.% CO_2, 10 vol.% H_2O for different O_2 co-feed (0.55 - 0.60 vol.%); T = 450 °C, GHSV = 50000 h^{-1}.

To better highlight the axial evolution of methane consumption rate, a simple descriptor can be computed by assuming pseudo-1st-order reaction kinetics with respect to methane, as reported in (5.1):

$$r_{CH_4} = -\frac{dC_{CH_4}}{d\tau} = -k^{app} \cdot C_{CH_4} \qquad\qquad (5.1)$$

where r_{CH_4} = methane conversion rate [mol/m³/s]; C_{CH_4} = methane molar concentration [mol/m³]; C = total molar concentration [mol/m³]; k^{app} = apparent reaction rate constant [1/s]; τ is the residence time, Q/V= volumetric flow rate/catalyst volume [s], v = constant velocity along the catalyst axis [mm/s].

The trend of k^{app}/v along the catalyst axial coordinate is analysed in the following.

As showed in Figure 5.6, for λ =0.9963 at 450 °C, it was found that the methane rate of consumption increases by an order of magnitude at a coordinate x = 16 mm, where O₂ partial pressure drops below 1.5 mbar. Note that such an increase can be significantly hampered by the onset of internal and external mass transfer limitations in the fast oxidation regime.
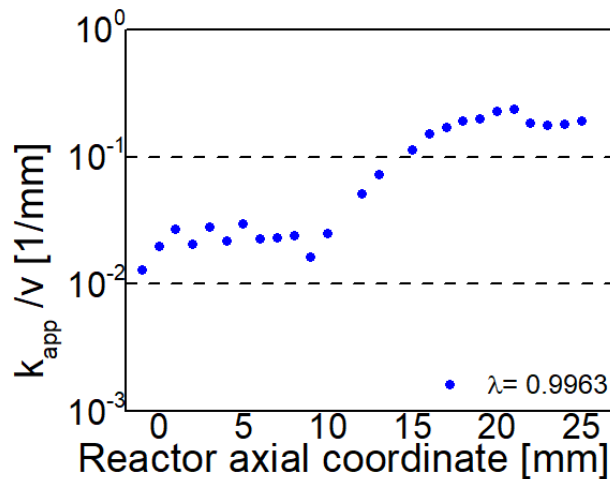
Figure 5.6 Methane consumption rate regimes for λ = 0.9963, at T= 450 °C, 10% of water

5.5 Effect of temperature

In order to study how temperature affects catalyst performances, experiments were made at T = 400 °C in the same window of lambda (λ =1.02, 0.99, 0.9963) explored at 450°C. Axial profiles of concentration and temperature are showed in Figure 5.7 (a)-(f) and Figure 5.8, respectively.
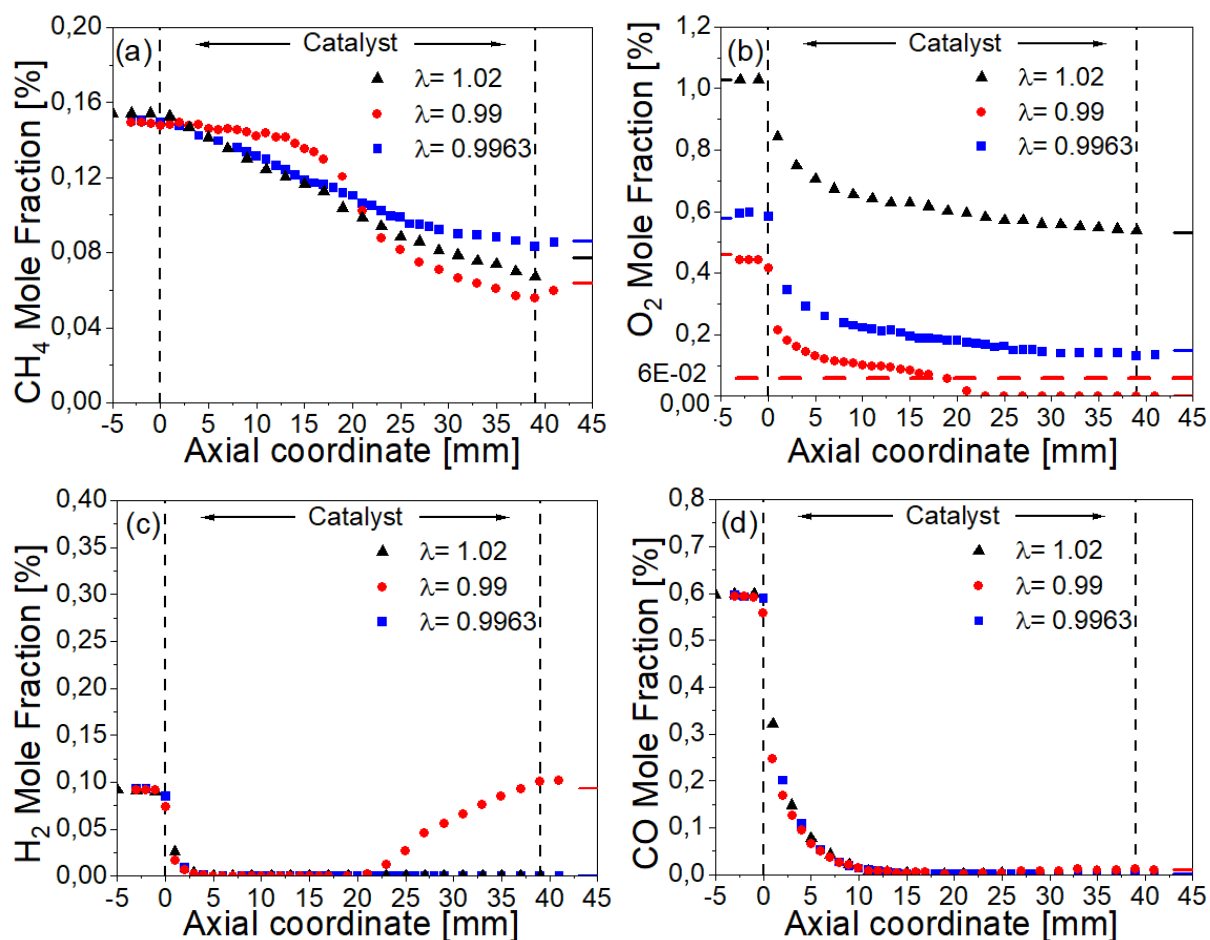
Figure 5.7 Concentration profiles (panels a-d) for the oxidation of a mixture of 0.15 vol.% CH_4, 0.6 vol.% CO, 0.1 vol.% H_2, 10.7 vol.% CO_2, 10 vol.% H_2O for different O_2 co-feed (0.46-1.03 vol.%); T = 400 °C, GHSV = 50000 h^{-1}.
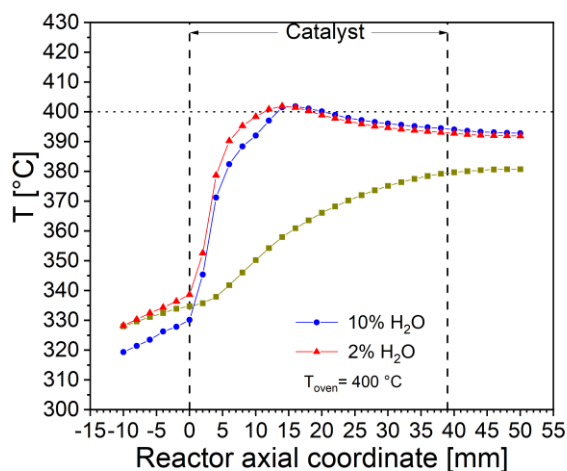

Figure 5.8 Temperature profiles for the oxidation of a mixture of 0.15 vol.% CH_4, 0.6 vol.% CO, 0.1 vol.% H_2, 10.7 vol.% CO_2, 10 vol.% H_2O for different O_2 co-feed (0.46-1.03 vol.%); T = 400 °C, GHSV = 50000 h^{-1}.

Expectedly, methane conversion rates are lower than at 450 °C at all λ values, as the reaction

kinetics are moderated by the temperature decrease. On the other hand, no temperature effects are observed in the consumption profiles of CO and H_2, confirming that oxidation of these species is under external mass transfer control.

Concentration profiles in Figure 5.7 show that at $\lambda = 0.9963$ CH_4 oxidation is not fast enough to achieve neither complete O_2 conversion nor the O_2 threshold where transition from slow to fast CH_4 oxidation regime occur. Accordingly, CH_4 concentration gradually decreases along the axial coordinate and no evidence of steam reforming (H_2 and CO production) is observed, similarly to the trend obtained at $\lambda = 1.02$. The CH_4 consumption rate at $\lambda = 0.9963$ is slightly lower than the one at $\lambda = 1.02$, likely due to the lower O_2 concentration.

Consistently with the concentration trends, temperature profiles in Figure 5.8 show that, after the sudden increase in the inlet region associated with H_2 and CO oxidation, temperature keeps almost constant and reasonably close to the oven temperature along the catalyst. The slightly lower temperature in the $\lambda = 0.9963$ experiment may magnify the kinetic effect of O_2 mentioned above.

Differently from the previous cases, at $\lambda = 0.99$ complete O_2 depletion is achieved at x=22 mm with H_2 and CO concentration increasing just downstream, confirming the onset of steam reforming and WGS reactions. In the upstream region CH_4 concentration first decrease at a slower rate than at higher λ, then starting from about x=15 mm CH_4 oxidation rate progressively increases bringing to complete O_2 consumption. Although the rate change is more gradual than at 450°C a O_2 threshold value for transition from slow to fast oxidation regime can be identified at about $P_{O_2}= 0.6$ mbar.

Following the same pseudo-1st-order reaction kinetics approach, an apparent kinetic constant of CH_4 oxidation rate at $\lambda = 0.99$ and T = 400 °C was computed (Figure 5.9).
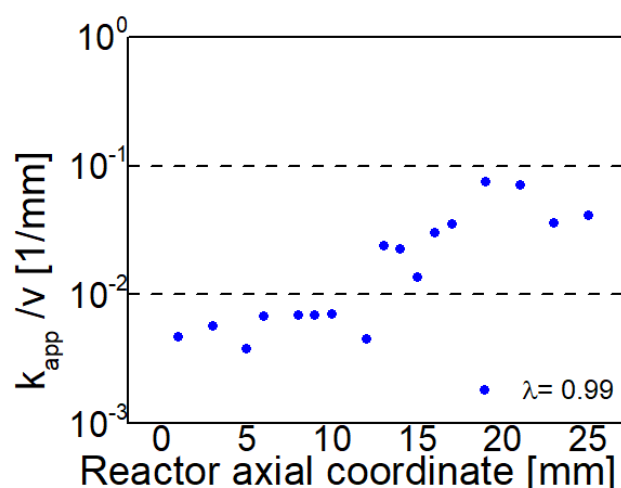
Figure 5.9 Methane consumption rate regimes for $\lambda = 0.99$, at T= 400 °C, 10% of water.

Once again, the apparent reaction rate constant exhibits one order of magnitude increase in the 15-22 mm region, where the oxygen concentration reaches the threshold $P_{O_2}=0.6$ mbar

5.6 Effect of water

As already acknowledged, one of the major hurdles in the use of palladium-based catalysts is the well-known inhibitory effect of water on their activity for methane combustion [127].

In order to investigate the effect of water on the observed kinetic regime transition a test was performed at $\lambda = 0.99$, T=400°C, 2% feed water. Figures 5.10 and 5.11 compare the axial temperature and concentration profiles collected with different water feed concentration (2 and 10 %).

Figure 5.10 Temperature profiles for the oxidation of a mixture of 0.15 vol.% CH_4, 0.46 vol.% O_2, 0.6 vol.% CO, 0.1 vol.% H_2, 10.7 vol.% CO_2, for different H_2O co-feed (2-10 vol.%); T = 400 °C, GHSV = 50000 h^{-1}.
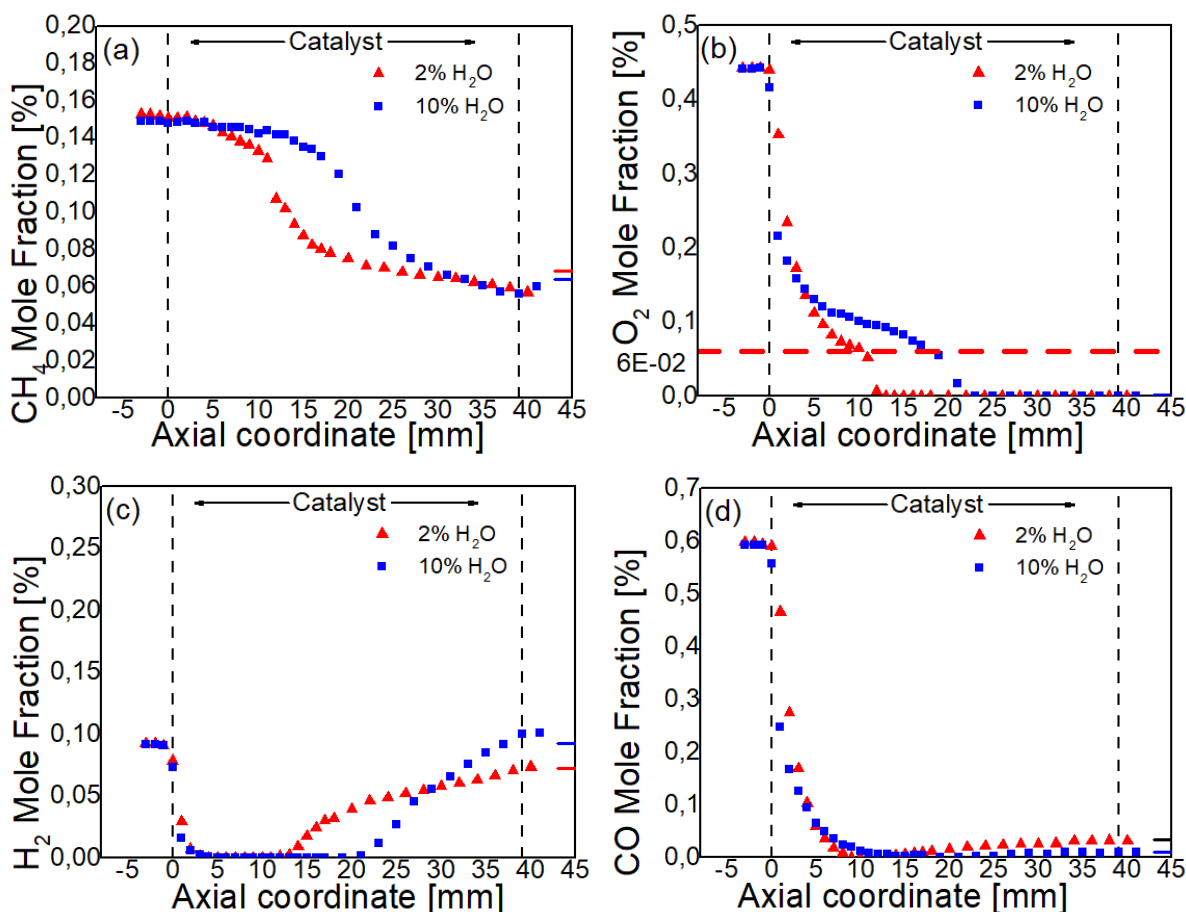
Figure 5.11 Concentration profiles (panels a-d) for the oxidation of a mixture of 0.15 vol.% CH_4, 0.46 vol.% O_2, 0.6 vol.% CO, 0.1 vol.% H_2, 10.7 vol.% CO_2, for different H_2O co-feed (0-2-10 vol.%); T = 400 °C, GHSV = 50000 h^{-1}.

Also in this case, the fast oxidation of H_2 and CO is not influenced by the water content. On the other hand, CH_4 oxidation rate at the inlet significantly increases on decreasing the feed water concentration, which results in an anticipated transition to the fast oxidation regime. Noteworthy the O_2 threshold for kinetic transition is independent of the water feed content.

5.7 Discussion

Spatially resolved profiles provide insight on the effect of oxygen on the integral CH_4 conversion performances, clearly showing that transition from slow to fast CH_4 consumption rate occur at a threshold value of oxygen partial pressure. Such a threshold markedly increases with temperature while is independent of water concentration. A rate enhancement of this kind is apparently due to a change in CH_4 oxidation kinetics. In fact, an alternative explanation assuming fast steam reforming followed by consecutive CO and H_2 oxidation can be ruled out, CH_4 consumption rate slowing down again once O_2 is completely depleted.

It was possible to find a good agreement between the O_2 concentration thresholds at which methane

conversion rate increases and the O_2 partial pressure at which transition metallic palladium – palladium oxide phase occurs as a function of temperature according to Chin et al. [128]. This is graphically illustrated in Figure 5.12: the solid line represents the O_2 pressures required for Pd oxidation in CH_4-O_2 mixtures according to results showed in [128], which the authors attribute to the thermodynamic threshold for Pd/PdO transition, while the symbols correspond to the critical oxygen concentration at which steep changes of methane conversion rate are observed in this work - respectively the red one at 450 °C and the green one at 400 °C.

Such a correspondence suggests that the boost of methane conversion is related to the onset of PdO reduction, possibly resulting in a PdO/Pd mixture with enhanced CH_4 combustion activity.

It is widely agreed that adjusting the oxidation state of the noble metal represents a viable approach to optimize catalyst performance. However, considerable debate has ensued regarding the specific nature of the most active catalyst state.

While the reduced state of palladium downstream complete O_2 consumption can be indirectly inferred from the appearance of H_2 in the concentration profiles, advanced spectroscopic techniques with high spatial resolution would be required to collect information about the actual state of palladium in the upstream region and, particularly, in the zone where the CH_4 oxidation activity occurs.

Examples of studies adopting techniques adapt to satisfy purposes of high spatial resolution are given in the following. In a study performed by Grunwaldt et al. [129], the integration of in situ X-ray absorption spectroscopy, X-ray diffraction, and on-line catalytic data has yielded valuable insights into the structure–performance correlation of a flame-synthesized Pd/ZrO_2 catalyst during the complete oxidation of methane. Upon heating, a rapid reduction, coupled with sintering of the Pd particles, results in a notable reduction in catalytic activity and induces hysteresis during the cooling phase. These investigations yielded additional insights into the significant alterations in the structure of the noble metal particles and their oxidation state during the heating and cooling cycles. Moreover, a dependence of the reactivity on Pd oxide particle size was highlighted by the research group of Ferri et al. [130] by employing X-ray absorption spectroscopy: the behaviour of Pd in Pd/Al_2O_3 during a methane combustion cycle, spanning temperatures from approximately 400 to 1130 K was investigated. The key findings include the identification of Pd oxide species as active sites for methane combustion, especially at temperatures below 950 K. At higher temperatures, reduced Pd was identified to catalyse the reaction, giving further proof of a reaction mechanism sensitive to the form of Pd in the catalyst. Furthermore, the catalyst - both before (fresh) and after the combustion cycle (used) - underwent characterization using HAADF-STEM, in situ EXAFS, and CO chemisorption techniques to investigate the impact of the reaction cycle on Pd dispersion.

Throughout the reaction cycle, restructuring and coalescence of Pd oxide nanoparticles was observed: this phenomenon results in an increase of low-temperature combustion activity in the subsequent run, suggesting that the efficiency of methane combustion, particularly at lower temperatures, is contingent upon the size of Pd oxide particles.
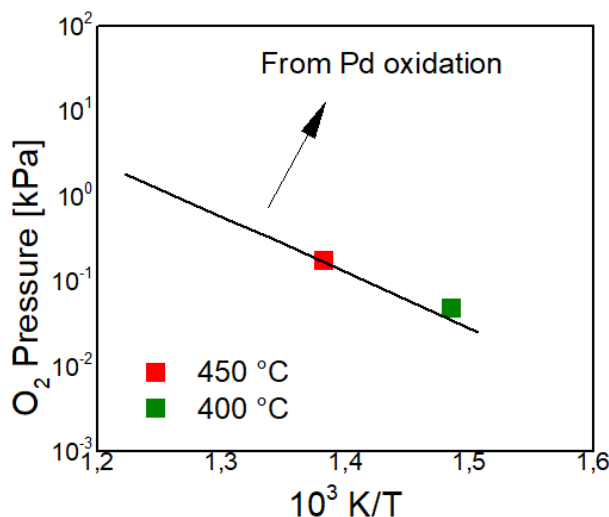
Figure 5.12 Correlation between temperature and critical oxygen partial pressure respectively at T = 450 °C (red square) and T = 400°C (green square) (figure readapted from S.I. [128]).

Finally, a model-based investigation has been performed in partnership with the research group ITCP in Karlsruhe Institute of Technology. A set of well-established microkinetic schemes [131], [132] has been implemented in the simulator tool DETCHEM[CHANNEL][133] to get predictions in the operative conditions of the experimental campaign. The results of the quantitative investigation have showed to be not in agreement with the experimental data collected in this research work showing that kinetic description of the complex PdO/Pd system deserve further investigations.

6 Conclusions

This thesis work focuses on the study of catalytic processes for enhancing the efficiency and emission control of biofuel-driven vehicles. Two model cases were considered, differing for the nature of the fuel: ethanol or methane.

In the case of bioethanol, focus was on the development of on-board bioethanol processor able to generate hydrogen by autothermal reforming of the fuel on a Rh-based catalyst. On board H_2 production would be useful either for reducing the catalytic converter emissions or as a source of power for auxiliary functions.

In the case of bio- or synthetic methane, focus was on the issue of methane emissions that can be abated by using a dedicated aftertreatment unit with Pd-based catalyst.

A central role in both investigations was played by the application of spatially-resolved sampling technique, an experimental methodology that allows to characterize the reactor performance through the measurement of temperature and concentration profiles across the reactor volume during the working conditions. Such a methodology is extremely valuable for collecting highly informative data on the kinetics of catalytic processes; in particular, direct information on the local evolution of the rate of reactions becomes accessible, complementing the information that typically comes from integral measurement of conversion and product distribution and may thus provide valuable data sets for the development and validation of kinetic and reactor models.

We herein briefly summarize the results that were achieved in both research lines.

Ethanol reformer - Bioethanol is a commercial fuel and its on board conversion into a H_2-rich stream can be realized by the CPO (catalytic partial oxidation) process, where the combination of oxidation, cracking and steam reforming reactions can guarantee high conversion and selectivity to syngas in reduced reactor volumes, with contact times of few milliseconds and rapid dynamic response. In this thesis work, a significant step forward has been done with respect to the state of the art towards the development of a complete kinetic model of ethanol CPO that captures all the main kinetic dependences; a combined homogeneous-heterogeneous kinetic scheme has been developed and validated against experimental data in isothermal micro-reactor, informative of the catalytic and thermal activation of the C_2-alcohol.

In fact, starting from a previous experimental investigation in annular microreactor, partial oxidation and steam reforming data were analyzed to derive a comprehensive kinetic scheme of the ethanol activation over Rh. The final kinetic scheme consists of six reactions, whose rate expressions were developed based on the analysis of the effects of the operating parameters

(temperature, contact time, feed composition) on the product distribution. One aspect of complexity was represented by the coking tendency of the reacting system, which required the description of C-poisoning phenomena due to the adsorption of C_2-oxygenated species and responsible for a reduction of the rate of ethanol steam reforming.

Besides, experiments in the empty reactor revealed that gas-phase reactions can affect the product distribution at temperatures higher than 600 °C and are strongly dependent on the concentration of O_2. In this work, a reduced homogeneous scheme, based on 36 reacting species, was developed starting from a state of the art detailed mechanism, which provided a very flexible modeling tool that can reproduce with accuracy the measured trends with a limited computational load.

The combined homogeneous and heterogenous kinetic schemes have been implemented in a mathematical model of a CPO autothermal reformer, based on Rh/Al_2O_3 coated monoliths. The model, incorporating also all the description of the relevant heat and mass transfer phenomena needed to describe the radial gradients between flowing fluid and catalytic walls, was validated against axially-resolved experimental data collected from the lab-scale autothermal reformer present in the LCCP labs.

It was shown that while the catalytic reactions are responsible for the rapid consumption of the reactants within few millimeters from the monolith entrance, with simultaneous formation of syngas, gas phase reactions are responsible for the formation of C_2 species like acetaldehyde and ethylene that can contribute to surface coking. Consecutive steam reforming of these species, however, limits their formation with a positive effect from water co-feed.

CH$_4$ emissions - As an additional strategy to support decarbonisation of transport sector, an experimental study was performed to investigate the performances of a commercial Pd based monolith catalyst in the abatement of methane. Different feed conditions – representative of the exhausts of a NG vehicle – were tested by acquiring concentration and temperature profiles through the spatially resolved technique. Experiments were accomplished in lambda sweep operation mode, by testing feeds with both excess and defect of oxygen. Catalyst stability was guaranteed by setting up a protocol consisting in switching periodically to richer compositions for a defined amount of time, this resulting in an almost constant downstream methane conversion.

The application of this novel technique allowed to capture the details of the kinetic phenomena that accompany the decaying O_2 concentration across the monolith channel, whose effects had been so far monitored only on the basis of integral data.

By comparing the catalyst performances at 450 °C for three significative values of lambda (1.02, lean; 0.9963, slightly rich; 0.99, rich), a sharp increase in methane conversion was observed for λ =

0.9963, corresponding to an increase of methane oxidation rate by one order of magnitude. A correspondent threshold in oxygen partial pressure (P_{O_2}=1.5 mbar) was highlighted as well. When performing the same experiments at 400 °C and 10% water content, the sharp increase in CH_4 consumption rate was detected at richer conditions (λ =0.99). The O_2 partial pressure threshold where the acceleration of CH_4 consumption rate was observed appeared to be shifted towards a lower value (P_{O_2}=0.6 mbar), which was reached only at the richest investigated conditions. This suggests that there is a relationship between the critical oxygen concentration and the reaction temperature, in agreement with literature on PdO/Pd transition.

As it concerns the investigations about water effect, the observed threshold of oxygen partial pressure seemed not to be affected by the variation of water content of the feed.

On the other hand, H_2 and CO oxidation seem not to be affected by the different conditions: they are rapidly oxidized in the first millimeters of the monolith regardless temperature and water concentration, indicating that their consumption rates are under external mass diffusion control.

Appendix

A.1. Evaluation of the invasiveness of the gas sampling probe on composition profiles

The introduction of a probe within the channel of a honeycomb monolith is expected to perturb the local flow field; it is very important that the perturbation is minimized. A verification of the impact of the sampling probes was herein searched by analyzing the consumption trends of CO and H_2, whose oxidation rate is high enough to hypothesize they are under external mass transfer control; thus, they depend only on the local flow dynamics.

In practice, to evaluate the influence of the measurement method, the experimental concentration profiles of hydrogen and carbon monoxide were compared with those calculated by the reactor model, which incorporates well-established mass transfer correlations [20] by assuming infinitely fast reaction rate.

Figure A.1.1 compares the experimental profiles of CO and H_2 consumption in the first section of the catalyst - collected with the 360 μm O.D. capillary - with the calculated trends for a lean test. The simulations were performed by assuming circular channel (due to the "rounding" effect of the washcoat) with hydraulic diameter calculated as the diameter of a circle with the same perimeter of the square channel of the monolith. The asymptotic Sherwood number was thus taken as Sh_{inf} = 2.977 and used in the correlation from Shah and London reported in [88]. A satisfactory agreement was obtained, thus indicating that the probe had a limited influence on the flow field.
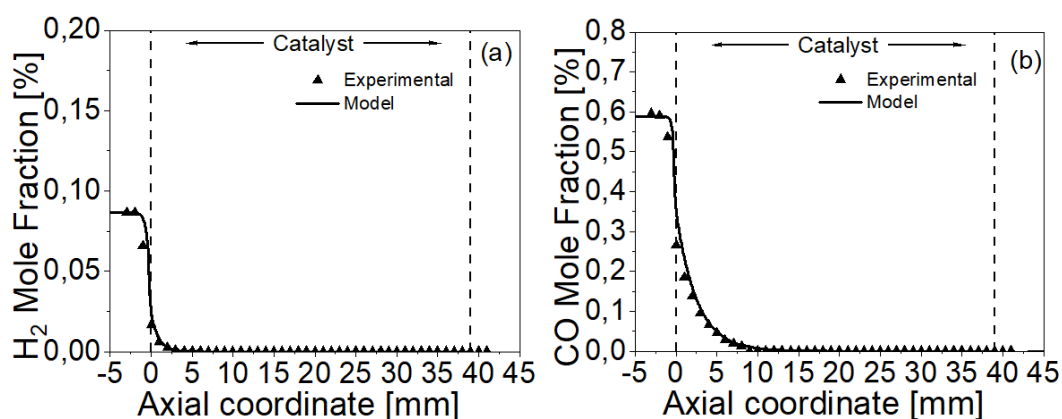
Figure A.1.1 Effect of the probe on the concentration profile of H_2 (a) and CO (b) at the inlet section of the catalyst. Comparison between experimental data (symbols) and model simulations (solid line). Operating conditions: 0.15 vol.% CH_4, 1.02 vol.% O_2, 0.6 vol.% CO, 0.1 vol.% H_2, 10.7 vol.% CO_2, 10 vol.% H_2O; T = 450 °C, GHSV = 50000 h^{-1}.

A.2. Rich pulse phenomenology

In order to provide deeper insight on the phenomena occurring during a rich pulse, the outlet concentration trends for methane, hydrogen, and oxygen are illustrated in Figure A.2.1. The pulse – with an approximative duration of 40 s - is representative of the ones performed during the tests reported in the manuscript.
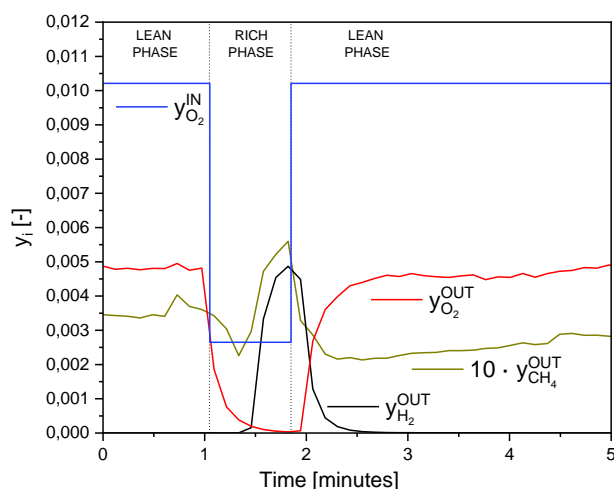
Figure A.2.1 Outlet molar fractions of CH_4 (gold), H_2 (black) and O_2 (red) during a lean-rich switch ($\lambda = 1.02 - 0.98$) detected by mass spectrometer analyses.

Passing from lean to fuel-rich conditions, an increase of methane and hydrogen outlet concentrations can be detected. Both the trends show a delay with respect to the O_2 cut-off which could be explained by considering the role of oxygen buffer from other catalyst components: both palladium and ceria have been proven to undergo catalytic redox processes favoured by the change in atmosphere, in agreement with analysis performed in [134].

Once rich conditions are established, the reactions expressed in Equations (A.2.1) – (A.2.3) lead to palladium oxide reduction:

$$CH_4 + 4\,PdO \rightarrow 4\,Pd + CO_2 + 2H_2O \quad \text{(A.2. 1)}$$

$$H_2 + PdO \rightarrow Pd + H_2O \quad \text{(A.2. 2)}$$

$$CO + PdO \rightarrow Pd + CO_2 \quad \text{(A.2. 3)}$$
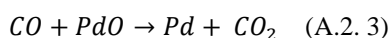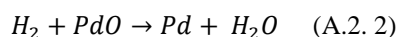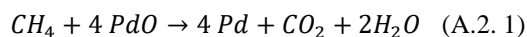
The subsequent methane conversion decline and hydrogen production, matched by the expected drop in O_2 molar fraction, are possibly the result of steam reforming (SR) and water-gas shift (WGS) reactions on metallic Pd (respectively Equations (A.2.4) and (A.2.5)) [120]:

$$CH_4 + H_2O \rightarrow CO + 3H_2 \quad (A.2.4)$$

$$CO + H_2O \rightarrow CO_2 + H_2 \quad (A.2.5)$$
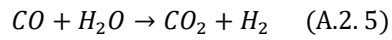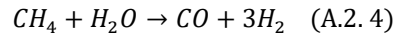
Correspondingly, it can be expected that, once excess oxygen conditions are restored, palladium undergoes oxidation:

$$Pd + \tfrac{1}{2}O_2 \rightarrow PdO \quad (A.2.6)$$
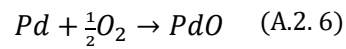
Going back to a lean condition causes a drop in methane concentration, which reaches a lower level than it was before the rich pulse, whereas a slight delay in oxygen molar fraction can be attributed to the stoichiometry in Equation A.2.6.

Notation

C = total molar concentration[mol/m^3]

C_{CH_4} = total molar concentration [mol/m^3]

k^{app} = apparent reaction rate constant [1/s]

r_{CH_4} = methane conversion rate [mol/m^3/s]

S = Catalyst equivalence ratio [-]

v = Constant velocity along the axis [mm/s]

y_i = i-species molar fraction at the ICE outlet [-]

y_{O2}^{st} = stoichiometric catalyst inlet oxygen molar fraction [–]

a_v = specific area per unit volume [1/m]

$\mathfrak{D}_i$ = species diffusivity [m^2/s]

G = superficial mass flow rate [kg/m^{2}s]

h = heat transfer coefficient [W/ m^{2}K]

k_{mat}= mass transfer coefficient [m/s]

L = length [cm]

m = mass [g]

MW = molecular weight [kg/kmol]

r_j^{het} = reaction rate [kmol/kg$_{cat}$s]

r_j^{hom} = reaction rate [kmol/m^{3}s]

$\widehat{S_{act}}$ = weight specific active surface [m^2/kg]

S_{act} = active surface [m^2]

T = temperature [K]

t = washcoat thickness calculated assuming a density of 1.38 g/cm^3

y_i = molar fraction at the ICE outlet (i.e., catalytic converter inlet) [-]

Greek symbols

α = volumetric specific surface area [1/m]

β = thermal efficiency of the adiabatic reactor [-]

γ = Rhodium dispersion [-]

ΔH_r = reaction enthalpy [J/kmol]

ε = void fraction [-]

η = activity factor [-]

λ = equivalence ratio [–]

$\upsilon_{i,j}$= stoichiometric coefficient [-]

ρ = density [kg/m^3]

τ = residence time [s]

Subscripts and superscripts

ad = adiabatic

BHS = Back heat shield

cat = catalyst

eff = effective

exp = experimental

g =gas phase

i = ith species

j =jth reaction

in = inlet of the catalyst

out = outlet of the catalyst

s = solid phase

w = washcoat

List of Figures

List of Tables

Bibliography

[1] European Commission, "Decarbonising our energy system to meet our climate goals," *Fit for 55 factsheets*, no. July, 2021.

[2] M. A. Tamor and E. B. Stechel, "Electrification of transportation means a lot more than a lot more electric vehicles," *iScience*, vol. 25, no. 6, Jun. 2022, doi: 10.1016/j.isci.2022.104376.

[3] F. Ausfelder and K. Wagemann, "Power-to-Fuels: E-Fuels as an Important Option for a Climate-Friendly Mobility of the Future," *Chem Ing Tech*, vol. 92, no. 1–2, pp. 21–30, 2020, doi: 10.1002/cite.201900180.

[4] EC, "Delivering on our targets," 2021.

[5] H. Li, C. Ma, X. Zou, A. Li, Z. Huang, and L. Zhu, "On-board methanol catalytic reforming for hydrogen Production-A review," *Int J Hydrogen Energy*, vol. 46, no. 43, pp. 22303–22327, 2021, doi: 10.1016/j.ijhydene.2021.04.062.

[6] A. Pramuanjaroenkij and S. Kakaç, "The fuel cell electric vehicles: The highlight review," *Int J Hydrogen Energy*, vol. 48, no. 25, pp. 9401–9425, 2023, doi: 10.1016/j.ijhydene.2022.11.103.

[7] Y. Long, G. Li, Z. Zhang, J. Liang, L. Mao, and Y. Li, "Effects of reformed exhaust gas recirculation on the HC and CO emissions of a spark-ignition engine fueled with LNG," *Int J Hydrogen Energy*, vol. 43, no. 45, pp. 21070–21078, 2018, doi: 10.1016/j.ijhydene.2018.09.077.

[8] G. H. Choi, Y. J. Chung, and S. Bin Han, "Performance and emissions characteristics of a hydrogen enriched LPG internal combustion engine at 1400 rpm," *Int J Hydrogen Energy*, vol. 30, no. 1, pp. 77–82, 2005, doi: 10.1016/j.ijhydene.2004.06.009.

[9] S. Woo, S. Baek, and K. Lee, "On-board LPG reforming system for an LPG · hydrogen mixed combustion engine," *Int J Hydrogen Energy*, vol. 45, no. 21, pp. 12203–12215, 2020, doi: 10.1016/j.ijhydene.2020.02.139.

[10] P. Polverino, F. D'Aniello, I. Arsie, and C. Pianese, "Study of the energetic needs for the on-board production of Oxy-Hydrogen as fuel additive in internal combustion engines," *Energy Convers Manag*, vol. 179, no. July 2018, pp. 114–131, 2019, doi: 10.1016/j.enconman.2018.09.082.

[11] I. A. Hassan, H. S. Ramadan, M. A. Saleh, and D. Hissel, "Hydrogen storage technologies for stationary and mobile applications: Review, analysis and perspectives," *Renewable and Sustainable Energy Reviews*, vol. 149, no. May, p. 111311, 2021, doi: 10.1016/j.rser.2021.111311.

[12] L. F. Brown, "A comparative study of fuels for on-board hydrogen production for fuel-cell-powered automobiles," *Int J Hydrogen Energy*, vol. 26, no. 4, pp. 381–397, 2001, doi: 10.1016/S0360-3199(00)00092-6.

[13] D. Pashchenko, "Thermochemical waste-heat recuperation as on-board hydrogen production technology," *Int J Hydrogen Energy*, vol. 46, no. 57, pp. 28961–28968, 2021, doi: 10.1016/j.ijhydene.2020.11.108.

[14] E. Ambroise *et al.*, "Exhaust gas recirculation for on-board hydrogen production by isooctane reforming: Comparison of performances of metal/ceria-zirconia based catalysts prepared through pseudo sol-gel or impregnation methods," *Catal Today*, vol. 154, no. 1–2, pp. 133–141, 2010, doi: 10.1016/j.cattod.2009.12.010.

[15] S. Woo and K. Lee, "Development and feasibility assessment of on-board catalytic reforming system for LPG engine to produce hydrogen in the transient state," *Appl Energy*, vol. 327, no. October, p. 120053, 2022, doi: 10.1016/j.apenergy.2022.120053.

[16] V. Gurau, A. Ogunleke, and F. Strickland, "Design of a methanol reformer for on-board production of hydrogen as fuel for a 3 kW High-Temperature Proton Exchange Membrane Fuel Cell power system," *Int J Hydrogen Energy*, vol. 45, no. 56, pp. 31745–31759, 2020, doi: 10.1016/j.ijhydene.2020.08.179.

[17] P. Purnima and S. Jayanti, "A high-efficiency, auto-thermal system for on-board hydrogen production for low temperature PEM fuel cells using dual reforming of ethanol," *Int J Hydrogen Energy*, vol. 41, no. 31, pp. 13800–13810, 2016, doi: 10.1016/j.ijhydene.2016.01.147.

[18] J. R. Salge, G. A. Deluga, and L. D. Schmidt, "Catalytic partial oxidation of ethanol over noble metal catalysts," *J Catal*, vol. 235, no. 1, pp. 69–78, 2005, doi: 10.1016/j.jcat.2005.07.021.

[19] D. Livio, A. Donazzi, A. Beretta, G. Groppi, and P. Forzatti, "Experimental and modeling analysis of the thermal behavior of an autothermal C 3H 8 catalytic partial oxidation reformer," *Ind Eng Chem Res*, vol. 51, no. 22, pp. 7573–7583, 2012, doi: 10.1021/ie202098q.

[20] R. Batista, A. Carrera, A. Beretta, and G. Groppi, "Thermal deactivation of Rh/α-Al2O3 in the catalytic partial oxidation of iso-octane: Effect of flow rate," *Catalysts*, vol. 9, no. 6, 2019, doi: 10.3390/catal9060532.

[21] A. Carrera, M. Pelucchi, A. Stagni, A. Beretta, and G. Groppi, "Catalytic partial oxidation of n-octane and iso-octane: Experimental and modeling results," *Int J Hydrogen Energy*, vol. 42, no. 39, pp. 24675–24688, 2017, doi: 10.1016/j.ijhydene.2017.08.020.

[22] A. Beretta *et al.*, "Optimal design of a CH4 CPO-reformer with honeycomb catalyst: Combined effect of catalyst load and channel size on the surface temperature profile," *Catal Today*, vol. 171, no. 1, pp. 79–83, 2011, doi: 10.1016/j.cattod.2011.03.081.

[23] D. Livio, C. Diehm, A. Donazzi, A. Beretta, and O. Deutschmann, "Catalytic partial oxidation of ethanol over Rh/Al2O3: Spatially resolved temperature and concentration profiles," *Appl Catal A Gen*, vol. 467, pp. 530–541, 2013, doi: 10.1016/j.apcata.2013.07.054.

[24] A. Mostafa, Y. Uysal, R. B. S. Junior, A. Beretta, and G. Groppi, "Catalytic partial oxidation of ethanol over Rh-coated monoliths investigated by the axially resolved sampling technique: Effect of H2O co-feed," *Catal Today*, vol. 367, no. April 2020, pp. 71–82, 2021, doi: 10.1016/j.cattod.2020.09.030.

[25] V. Piazza *et al.*, "H2 from biofuels and carriers: gas-phase and surface ethanol conversion pathways on Rh/Al2O3 investigated by annular microreactor coupled with Raman and FTIR spectroscopy," *J Catal*, vol. 413, pp. 184–200, 2022, doi: 10.1016/j.jcat.2022.06.012.

[26] C. H. Bartholomew, "Mechanisms of catalyst deactivation," 2001.

[27] P. D. Vaidya and A. E. Rodrigues, "Kinetics of steam reforming of ethanol over a Ru/Al2O 3 catalyst," *Ind Eng Chem Res*, vol. 45, no. 19, pp. 6614–6618, 2006, doi: 10.1021/ie051342m.

[28] O. Görke, P. Pfeifer, and K. Schubert, "Kinetic study of ethanol reforming in a microreactor," *Appl Catal A Gen*, vol. 360, no. 2, pp. 232–241, 2009, doi: 10.1016/j.apcata.2009.03.026.

[29] C. Graschinsky *et al.*, "Ethanol steam reforming over Rh(1%)MgAl2O4/Al 2O3: A kinetic study," *Ind Eng Chem Res*, vol. 49, no. 24, pp. 12383–12389, 2010, doi: 10.1021/ie101284k.

[30]   C. Graschinsky, J. L. Contreras, N. Amadeo, and M. Laborde, "Ethanol Oxidative Steam Reforming over Rh(1%)/MgAl2O4/Al2O3 Catalyst," *Ind Eng Chem Res*, vol. 53, pp. 15348–15356, 2014, doi: 10.31857/s0044457x21080298.

[31]   N. R. Peela and D. Kunzru, "Oxidative steam reforming of ethanol over Rh based catalysts in a micro-channel reactor," *Int J Hydrogen Energy*, vol. 36, no. 5, pp. 3384–3396, Mar. 2011, doi: 10.1016/j.ijhydene.2010.12.091.

[32]   B. Sawatmongkhon, K. Theinnoi, T. Wongchang, C. Haoharn, C. Wongkhorsub, and E. Sukjit, "Modeling of Hydrogen Production from Catalytic Partial Oxidation of Ethanol over a Platinum-Rhodium-Supported Catalyst," *Energy and Fuels*, vol. 35, no. 5, pp. 4404–4417, 2021, doi: 10.1021/acs.energyfuels.0c04125.

[33]   N. Hebben, C. Diehm, and O. Deutschmann, "Catalytic partial oxidation of ethanol on alumina-supported rhodium catalysts: An experimental study," *Appl Catal A Gen*, vol. 388, no. 1–2, pp. 225–231, 2010, doi: 10.1016/j.apcata.2010.08.055.

[34]   C. Diehm, T. Kaltschmitt, and O. Deutschmann, "Hydrogen production by partial oxidation of ethanol/gasoline blends over Rh/Al2O3," *Catal Today*, vol. 197, no. 1, pp. 90–100, Dec. 2012, doi: 10.1016/J.CATTOD.2012.06.032.

[35]   T. Lu and C. K. Law, "Toward accommodating realistic fuel chemistry in large-scale computations," *Prog Energy Combust Sci*, vol. 35, no. 2, pp. 192–215, 2009, doi: 10.1016/j.pecs.2008.10.002.

[36]   A. Cuoci, A. Frassoldati, T. Faravelli, and E. Ranzi, "OpenSMOKE++: An object-oriented framework for the numerical modeling of reactive systems with detailed kinetic mechanisms," *Comput Phys Commun*, vol. 192, pp. 237–264, 2015, doi: 10.1016/j.cpc.2015.02.014.

[37]   G. W. Stewart, "The decompositional approach to matrix computation," *Comput Sci Eng*, vol. 2 (1), pp. 50–59, 2000.

[38]   M. H. M. Ashnani, T. Miremadi, A. Johari, and A. Danekar, "Environmental Impact of Alternative Fuels and Vehicle Technologies: A Life Cycle Assessment Perspective," *Procedia Environ Sci*, vol. 30, pp. 205–210, 2015, doi: 10.1016/j.proenv.2015.10.037.

[39]   O. Hijazi, S. Munro, B. Zerhusen, and M. Effenberger, "Review of life cycle assessment for biogas production in Europe," *Renewable and Sustainable Energy Reviews*, vol. 54, pp. 1291–1300, 2016, doi: 10.1016/j.rser.2015.10.013.

[40]   European Commission, "Promoting the Uptake of Gaseous Vehicle Fuels, Biogas and Natural Gas in Europe - Intelligent Energy Europe - European Commission," 2018, [Online]. Available: https://ec.europa.eu/energy/intelligent/projects/en/projects/gashighway

[41]   Biogasmax, "Biogasmax 2006/2010 the synthesis," *Biogasmax*, p. 43, 2010.

[42]   M. Jarraud and A. Steiner, *Summary for policymakers*, vol. 9781107025. 2012. doi: 10.1017/CBO9781139177245.003.

[43]   P. Lott and O. Deutschmann, "Lean-Burn Natural Gas Engines: Challenges and Concepts for an Efficient Exhaust Gas Aftertreatment System," *Emission Control Science and Technology*, vol. 7, no. 1, pp. 1–6, 2021, doi: 10.1007/s40825-020-00176-w.

[44]   R. Burch, P. K. Loader, and F. J. Urbano, "Some aspects of hydrocarbon activation on platinum group metal combustion catalysts," *Catal Today*, vol. 27, no. 1–2, pp. 243–248, 1996, doi: 10.1016/0920-5861(95)00194-8.

[45] D. Bounechada, G. Groppi, P. Forzatti, K. Kallinen, and T. Kinnunen, "Effect of periodic lean/rich switch on methane conversion over a Ce-Zr promoted Pd-Rh/Al 2O 3 catalyst in the exhausts of natural gas vehicles," *Appl Catal B*, vol. 119–120, pp. 91–99, 2012, doi: 10.1016/j.apcatb.2012.02.025.

[46] J. Gong *et al.*, "O2 dosage as a descriptor of TWC performance under lean/rich dithering in stoichiometric natural gas engines," *Catal Today*, no. February, pp. 1–11, 2020, doi: 10.1016/j.cattod.2020.02.022.

[47] D. Ferri, M. Elsener, and O. Kröcher, "Methane oxidation over a honeycomb Pd-only three-way catalyst under static and periodic operation," *Appl Catal B*, vol. 220, pp. 67–77, 2018, doi: 10.1016/j.apcatb.2017.07.070.

[48] R. Hutter, L. De Libero, P. Elbert, and C. H. Onder, "Catalytic methane oxidation in the exhaust gas aftertreatment of a lean-burn natural gas engine," *Chemical Engineering Journal*, vol. 349, no. May, pp. 156–167, 2018, doi: 10.1016/j.cej.2018.05.054.

[49] M. Wang, P. Dimopoulos Eggenschwiler, D. Ferri, and O. Kröcher, "Experimental and modeling-based analysis of reaction pathways on catalysts for natural gas engines under periodic lean/rich oscillations," *Chemical Engineering Journal*, vol. 430, 2022, doi: 10.1016/j.cej.2021.132848.

[50] S. Colussi, A. Trovarelli, G. Groppi, and J. Llorca, "The effect of CeO2 on the dynamics of Pd-PdO transformation over Pd/Al2O3 combustion catalysts," *Catal Commun*, vol. 8, no. 8, pp. 1263–1266, 2007, doi: 10.1016/j.catcom.2006.11.020.

[51] S. K. Matam, M. H. Aguirre, A. Weidenkaff, and D. Ferri, "Revisiting the problem of active sites for methane combustion on Pd/Al 2O 3 by operando XANES in a lab-scale fixed-bed reactor," *Journal of Physical Chemistry C*, vol. 114, no. 20, pp. 9439–9443, 2010, doi: 10.1021/jp1019697.

[52] Y. H. Chin, C. Buda, M. Neurock, and E. Iglesia, "Consequences of metal-oxide interconversion for C-H bond activation during CH4 reactions on Pd catalysts," *J Am Chem Soc*, vol. 135, no. 41, pp. 15425–15442, 2013, doi: 10.1021/ja405004m.

[53] J. D. Grunwaldt, N. Van Vegten, and A. Baiker, "Insight into the structure of supported palladium catalysts during the total oxidation of methane," *Chemical Communications*, no. 44, pp. 4635–4637, 2007, doi: 10.1039/b710222d.

[54] T. Franken *et al.*, "Effect of Short Reducing Pulses on the Dynamic Structure, Activity, and Stability of Pd/Al2O3for Wet Lean Methane Oxidation," *ACS Catal*, vol. 11, no. 8, pp. 4870–4879, 2021, doi: 10.1021/acscatal.1c00328.

[55] J. Nilsson *et al.*, "Methane oxidation over Pd/Al2O3 under rich/lean cycling followed by operando XAFS and modulation excitation spectroscopy," *J Catal*, vol. 356, pp. 237–245, 2017, doi: 10.1016/j.jcat.2017.10.018.

[56] D. Bounechada, G. Groppi, P. Forzatti, K. Kallinen, and T. Kinnunen, "Enhanced methane conversion under periodic operation over a Pd/Rh based TWC in the exhausts from NGVs," in *Topics in Catalysis*, May 2013, pp. 372–377. doi: 10.1007/s11244-013-9982-8.

[57] R. Gholami, M. Alyani, and K. J. Smith, *Deactivation of Pd catalysts by water during low temperature methane oxidation relevant to natural gas vehicle converters*, vol. 5, no. 2. 2015. doi: 10.3390/catal5020561.

[58]   D. Ciuparu, N. Katsikis, and L. Pfefferle, "Temperature and time dependence of the water inhibition effect on supported palladium catalyst for methane combustion," *Appl Catal A Gen*, vol. 216, no. 1–2, pp. 209–215, 2001, doi: 10.1016/S0926-860X(01)00558-0.

[59]   D. Ciuparu and L. Pfefferle, "Support and water effects on palladium based methane combustion catalysts," *Appl Catal A Gen*, vol. 209, no. 1–2, pp. 415–428, 2001, doi: 10.1016/S0926-860X(00)00783-3.

[60]   R. Burch, F. J. Urbano, and P. K. Loader, "Methane combustion over palladium catalysts: The effect of carbon dioxide and water on activity," *Appl Catal A Gen*, vol. 123, no. 1, pp. 173–184, 1995, doi: 10.1016/0926-860X(94)00251-7.

[61]   W. R. Schwartz and L. D. Pfefferle, "Combustion of methane over palladium-based catalysts: Support interactions," *Journal of Physical Chemistry C*, vol. 116, no. 15, pp. 8571–8578, 2012, doi: 10.1021/jp2119668.

[62]   W. R. Schwartz, D. Ciuparu, and L. D. Pfefferle, "Combustion of methane over palladium-based catalysts: Catalytic deactivation and role of the support," *Journal of Physical Chemistry C*, vol. 116, no. 15, pp. 8587–8593, 2012, doi: 10.1021/jp212236e.

[63]   G. S. Bugosh, V. G. Easterling, I. A. Rusakova, and M. P. Harold, "Anomalous steady-state and spatio-temporal features of methane oxidation on Pt/Pd/Al2O3 monolith spanning lean and rich conditions," *Appl Catal B*, vol. 165, pp. 68–78, 2015, doi: 10.1016/j.apcatb.2014.09.058.

[64]   D. Bounechada, G. Groppi, P. Forzatti, K. Kallinen, and T.-J. Kinnunen, "Enhanced methane conversion under periodic operation over a Pd/Rh based TWC in the exhausts from NGVs," in *CAPoC9*, Brussels.

[65]   K. Morgan *et al.*, "Evolution and Enabling Capabilities of Spatially Resolved Techniques for the Characterization of Heterogeneously Catalyzed Reactions," *ACS Catal*, vol. 6, no. 2, pp. 1356–1381, Aug. 2016, doi: 10.1021/acscatal.5b02602.

[66]   A. Baiker and M. Bergougnan, "Investigation of a Fixed-Bed Pilot Reactor by Dynamic Experimentation. 1. Apparatus and Experimental Results," *Can. J. Chem. Eng.*, vol. 63, pp. 138–145, 1985.

[67]   W. P. Partridge, J. M. E. Storey, S. A. Lewis, R. W. D. G. L. Smithwick, M. J. C. N. V. Cunningham, and T. M. Yonushonis, "Time-Resolved Measurements of Emission Transients By Mass Spectrometry," *SAE Tech. Pap. Ser.*, vol. 2000-01–29, 2000.

[68]   M. J. P. W. P. Currier N. W. Cunningham, J. Storey, and R. W. D. R. W. M. E.; Lewis S. A. Smithwick, "Exhaust Aftertreatment Gas Phase Measurements in situ," in *6th Diesel Engine Emissions Reduction Workshop. DEER*,

[69]   K. Aftab, J. Mandur, H. Budman, N. W. Currier, A. Yezerets, and W. S. Epling, "Spatially-resolved calorimetry: Using IR thermography to measure temperature and trapped NOX distributions on a NOX adsorber catalyst," *Catal Letters*, vol. 125, no. 3–4, pp. 229–235, 2008, doi: 10.1007/s10562-008-9578-2.

[70]   C. Diehm and O. Deutschmann, "Hydrogen production by catalytic partial oxidation of methane over staged Pd/Rh coated monoliths: Spatially resolved concentration and temperature profiles," *Int J Hydrogen Energy*, vol. 39, no. 31, pp. 17998–18004, 2014, doi: 10.1016/j.ijhydene.2014.06.094.

[71]   R. Horn, K. A. Williams, N. J. Degenstein, and L. D. Schmidt, "Syngas by catalytic partial oxidation of methane on rhodium: Mechanistic conclusions from spatially resolved measurements and numerical simulations," *J Catal*, vol. 242, no. 1, pp. 92–102, Aug. 2006, doi: 10.1016/j.jcat.2006.05.008.

[72]   R. Horn, N. J. Degenstein, K. A. Williams, and L. D. Schmidt, "Spatial and temporal profiles in millisecond partial oxidation processes," *Catal Letters*, vol. 110, no. 3–4, pp. 169–178, 2006, doi: 10.1007/s10562-006-0117-8.

[73]   J. Sá *et al.*, "SpaciMS: Spatial and temporal operando resolution of reactions within catalytic monoliths," *Analyst*, vol. 135, no. 9, pp. 2260–2272, 2010, doi: 10.1039/c0an00303d.

[74]   M. Hettel, C. Diehm, B. Torkashvand, and O. Deutschmann, "Critical evaluation of in situ probe techniques for catalytic honeycomb monoliths," in *Catalysis Today*, Nov. 2013, pp. 2–10. doi: 10.1016/j.cattod.2013.05.005.

[75]   M. Hettel, C. Antinori, and O. Deutschmann, "CFD Evaluation of In Situ Probe Techniques for Catalytic Honeycomb Monoliths," *Emission Control Science and Technology*, vol. 2, no. 4, pp. 188–203, Oct. 2016, doi: 10.1007/s40825-016-0043-1.

[76]   J. Choi, W. P. Partridge, W. S. Epling, N. W. Currier, and T. M. Yonushonis, "Intra-channel evolution of carbon monoxide and its implication on the regeneration of a monolithic Pt/K/Al2O3 NOx storage-reduction catalyst," *Catal Today*, vol. 114, no. 1, pp. 102–111, 2006.

[77]   A. Beretta *et al.*, "Development of a mechanistic kinetic model of the higher alcohol synthesis over a Cs-doped Zn/Cr/O catalyst. 1. Model derivation and data fitting," *Ind Eng Chem Res*, vol. 35, no. 7, pp. 2144–2153, 1996, doi: 10.1021/ie9506173.

[78]   A. Beretta, P. Baiardi, D. Prina, and P. Forzatti, *Development of a catalytic reactor with annular configuration*, vol. 118. Elsevier Masson SAS, 1998. doi: 10.1016/s0167-2991(98)80220-6.

[79]   A. Beretta, P. Baiardi, D. Prina, and P. Forzatti, "Analysis of a catalytic annular reactor for very short contact times," *Chem Eng Sci*, vol. 54, no. 6, pp. 765–773, 1999, doi: 10.1016/S0009-2509(98)00261-9.

[80]   A. Donazzi, A. Beretta, G. Groppi, and P. Forzatti, "Catalytic partial oxidation of methane over a 4% Rh/α-Al2O3 catalyst. Part I: Kinetic study in annular reactor," *J Catal*, vol. 255, no. 2, pp. 241–258, 2008, doi: 10.1016/j.jcat.2008.02.009.

[81]   A. Beretta *et al.*, "Testing in annular micro-reactor and characterization of supported Rh nanoparticles for the catalytic partial oxidation of methane: Effect of the preparation procedure," *Appl Catal B*, vol. 83, no. 1–2, pp. 96–109, 2008, doi: 10.1016/j.apcatb.2008.02.007.

[82]   A. Beretta, T. Bruno, G. Groppi, I. Tavazzi, and P. Forzatti, "Conditioning of Rh/α-Al2O3 catalysts for H2 production via CH4 partial oxidation at high space velocity," *Appl Catal B*, vol. 70, no. 1–4, pp. 515–524, 2007, doi: 10.1016/j.apcatb.2006.01.014.

[83]   T. Bruno, A. Beretta, G. Groppi, M. Roderi, and P. Forzatti, "A study of methane partial oxidation in annular reactor: Activity of Rh/α-Al2O3 and Rh/ZrO2 catalysts," *Catal Today*, vol. 99, no. 1–2, pp. 89–98, 2005, doi: 10.1016/j.cattod.2004.09.027.

[84]   A. Beretta, G. Groppi, M. Lualdi, I. Tavazzi, and P. Forzatti, "Experimental and modeling analysis of methane partial oxidation: transient and steady-state behavior of rh-coated honeycomb monoliths," *Ind Eng Chem Res*, vol. 48, no. 8, pp. 3825–3836, 2009, doi: 10.1021/ie8017143.

[85] C. Brinkmeier, "Automotive three way exhaust aftertreatment under transient conditions: measurements, modeling and simulation," *Thesis*, pp. 1–180, 2006, [Online]. Available: http://elib.uni-stuttgart.de/opus/volltexte/2007/2813/

[86] M. Q. Wang and H. S. Huang, "A Full Fuel-Cycle Analysis of Energy and Emissions Impacts of Transportation Fuels Produced from Natural Gas," *U.S. Department of Energy*, vol. ESD, no. 40, p. 88, 1999, [Online]. Available: http://www.doe.gov/bridge

[87] V. Troisi, V. Piazza, A. Stagni, A. Frassoldati, G. Groppi, and A. Beretta, "H2 from biofuels and carriers: A concerted homo-heterogeneous kinetic model of ethanol partial oxidation and steam reforming on Rh/Al2O3," *Int J Hydrogen Energy*, no. xxxx, pp. 1–15, 2023, doi: 10.1016/j.ijhydene.2023.03.178.

[88] M. Maestri, A. Beretta, G. Groppi, E. Tronconi, and P. Forzatti, "Comparison among structured and packed-bed reactors for the catalytic partial oxidation of CH4 at short contact times," *Catal Today*, vol. 105, no. 3–4, pp. 709–717, 2005, doi: 10.1016/j.cattod.2005.06.045.

[89] R. K. Shah and A. L. London, "Laminar Flow Forced Convection in Ducts," in *Academic Press, New York*, 1978.

[90] G. Groppi, A. Belloli, E. Tronconi, and P. Forzatti, "A comparison of lumped and distributed models of monolith catalytic combustors," *Chem Eng Sci*, vol. 50, no. 17, pp. 2705–2715, 1995, doi: 10.1016/0009-2509(95)00099-Q.

[91] S. Rebughini, A. Cuoci, and M. Maestri, "Hierarchical analysis of the gas-to-particle heat and mass transfer in micro packed bed reactors," *Chemical Engineering Journal*, vol. 289, pp. 471–478, Apr. 2016, doi: 10.1016/j.cej.2015.12.089.

[92] A. Cuoci, A. Frassoldati, T. Faravelli, and E. Ranzi, "OpenSMOKE++: An object-oriented framework for the numerical modeling of reactive systems with detailed kinetic mechanisms," *Comput Phys Commun*, vol. 192, pp. 237–264, 2015, doi: 10.1016/j.cpc.2015.02.014.

[93] E. Ranzi, C. Cavallotti, A. Cuoci, A. Frassoldati, M. Pelucchi, and T. Faravelli, "New reaction classes in the kinetic modeling of low temperature oxidation of n-alkanes," *Combust Flame*, vol. 162, no. 5, pp. 1679–1691, 2015, doi: 10.1016/j.combustflame.2014.11.030.

[94] W. K. Metcalfe, S. M. Burke, S. S. Ahmed, and H. J. Curran, "A hierarchical and comparative kinetic modeling study of C1 - C2 hydrocarbon and oxygenated fuels," *Int J Chem Kinet*, vol. 45, no. 10, pp. 638–675, 2013, doi: 10.1002/kin.20802.

[95] S. M. Burke *et al.*, "An experimental and modeling study of propene oxidation. Part 2: Ignition delay time and flame speed measurements," *Combust Flame*, vol. 162, no. 2, pp. 296–314, 2015, doi: 10.1016/j.combustflame.2014.07.032.

[96] A. Burcat and R. Branko, "Third millennium ideal gas and condensed phase thermochemical database for combustion with updates from active thermochemical tables," *Technical Report*, vol. ANL-05/20, no. September, p. ANL-05/20 TAE 960, 2005, doi: 10.2172/925269.

[97] "CreckModeling." [Online]. Available: http://creckmodeling.chem.polimi.it

[98] A. Stagni, "Implementation of detailed chemistry in large-scale combustion computations - PhD Thesis," 2016, doi: 10.1109/IEMBS.2004.1404351.

[99] P. Pepiot-Desjardins and H. Pitsch, "An efficient error-propagation-based reduction method for large chemical kinetic mechanisms," *Combust Flame*, vol. 154, no. 1–2, pp. 67–81, 2008, doi: 10.1016/j.combustflame.2007.10.020.

[100]   K. E. Niemeyer, C. J. Sung, and M. P. Raju, "Skeletal mechanism generation for surrogate fuels using directed relation graph with error propagation and sensitivity analysis," *Combust Flame*, vol. 157, no. 9, pp. 1760–1770, 2010, doi: 10.1016/j.combustflame.2009.12.022.

[101]   M. U. Alzueta and J. M. Hernández, "Ethanol oxidation and its interaction with nitric oxide," *Energy and Fuels*, vol. 16, no. 1, pp. 166–171, 2002, doi: 10.1021/ef010153n.

[102]   A. Stagni, S. Schmitt, M. Pelucchi, A. Frassoldati, K. Kohse-Höinghaus, and T. Faravelli, "Dimethyl ether oxidation analyzed in a given flow reactor: Experimental and modeling uncertainties," *Combust Flame*, vol. 240, Jun. 2022, doi: 10.1016/j.combustflame.2022.111998.

[103]   C. Esarte, M. Peg, M. P. Ruiz, Á. Millera, R. Bilbao, and M. U. Alzueta, "Pyrolysis of ethanol: Gas and soot products formed," *Ind Eng Chem Res*, vol. 50, no. 8, pp. 4412–4419, 2011, doi: 10.1021/ie1022628.

[104]   M. Pelucchi *et al.*, "An experimental and kinetic modeling study of the pyrolysis and oxidation of n-C3C5 aldehydes in shock tubes," *Combust Flame*, vol. 162, no. 2, pp. 265–286, 2015, doi: 10.1016/j.combustflame.2014.07.027.

[105]   A. Frassoldati, A. Cuoci, T. Faravelli, and E. Ranzi, "Kinetic modeling of the oxidation of ethanol and gasoline surrogate mixtures," *Combustion Science and Technology*, vol. 182, no. 7, pp. 653–667, 2010, doi: 10.1080/00102200903466368.

[106]   V. Piazza, R. B. S. Junior, D. Gazzoli, G. Groppi, and A. Beretta, "H2 from biofuels and carriers: A kinetic investigation of formic acid decomposition on Rh/Al2O3 in the annular reactor," *Chemical Engineering Research and Design*, vol. 181, pp. 458–472, 2022, doi: 10.1016/j.cherd.2022.03.048.

[107]   D. Pagani *et al.*, "A kinetic analysis of the partial oxidation of C 3H 8 over a 2% Rh/Al 2O 3 catalyst in annular microreactor," *Catal Today*, vol. 197, no. 1, pp. 265–280, 2012, doi: 10.1016/j.cattod.2012.09.004.

[108]   D. Pagani *et al.*, "A kinetic investigation of the catalytic partial oxidation of propylene over a Rh/Al2O3 catalyst," *Ind Eng Chem Res*, vol. 53, no. 5, pp. 1804–1815, 2014, doi: 10.1021/ie4025352.

[109]   A. M. da Silva, L. v. Mattos, J. Múnera, E. Lombardo, F. B. Noronha, and L. Cornaglia, "Study of the performance of Rh/La2O3-SiO2 and Rh/CeO2 catalysts for SR of ethanol in a conventional fixed-bed reactor and a membrane reactor," *Int J Hydrogen Energy*, vol. 40, no. 11, pp. 4154–4166, Mar. 2015, doi: 10.1016/j.ijhydene.2015.01.106.

[110]   T. S. Moraes, L. E. P. Borges, R. Farrauto, and F. B. Noronha, "Steam reforming of ethanol on Rh/SiCeO2 washcoated monolith catalyst: Stable catalyst performance," *Int J Hydrogen Energy*, vol. 43, no. 1, pp. 115–126, Jan. 2018, doi: 10.1016/j.ijhydene.2017.10.180.

[111]   A. Donazzi, A. Beretta, G. Groppi, and P. Forzatti, "Catalytic partial oxidation of methane over a 4% Rh/α-Al2O3 catalyst Part II: Role of CO2 reforming," *J Catal*, vol. 255, no. 2, pp. 259–268, 2008, doi: 10.1016/j.jcat.2008.02.010.

[112]   A. Le Valant, F. Can, N. Bion, D. Duprez, and F. Epron, "Hydrogen production from raw bioethanol steam reforming : Optimization of catalyst composition with improved stability against various impurities," *Int J Hydrogen Energy*, vol. 35, no. 10, pp. 5015–5020, 2010, doi: 10.1016/j.ijhydene.2009.09.008.

[113] Y. H. Chin, C. Buda, M. Neurock, and E. Iglesia, "Selectivity of chemisorbed oxygen in C-H bond activation and CO oxidation and kinetic consequences for CH4-O2 catalysis on Pt and Rh clusters," *J Catal*, vol. 283, no. 1, pp. 10–24, 2011, doi: 10.1016/j.jcat.2011.06.011.

[114] Y. H. Chin, C. Buda, M. Neurock, and E. Iglesia, "Reactivity of chemisorbed oxygen atoms and their catalytic consequences during CH4-O2 catalysis on supported Pt clusters," *J Am Chem Soc*, vol. 133, no. 40, pp. 15958–15978, 2011, doi: 10.1021/ja202411v.

[115] J. Wei and E. Iglesia, "Structural requirements and reaction pathways in methane activation and chemical conversion catalyzed by rhodium," *J Catal*, vol. 225, no. 1, pp. 116–127, 2004, doi: 10.1016/j.jcat.2003.09.030.

[116] A. Cifuentes, R. Torres, and J. Llorca, "Modelling of the ethanol steam reforming over Rh-Pd/CeO2 catalytic wall reactors," *Int J Hydrogen Energy*, vol. 45, no. 49, pp. 26265–26273, Oct. 2020, doi: 10.1016/j.ijhydene.2019.11.034.

[117] A. Carrera, A. Beretta, and G. Groppi, "Catalytic Partial Oxidation of Iso-octane over Rh/α-Al2O3 in an Adiabatic Reactor: An Experimental and Modeling Study," *Ind Eng Chem Res*, vol. 56, no. 17, pp. 4911–4919, 2017, doi: 10.1021/acs.iecr.7b00255.

[118] A. Donazzi *et al.*, "Synergy of homogeneous and heterogeneous chemistry probed by in situ spatially resolved measurements of temperature and composition," *Angewandte Chemie - International Edition*, vol. 50, no. 17, pp. 3943–3946, 2011, doi: 10.1002/anie.201007346.

[119] F. Arosio, S. Colussi, A. Trovarelli, and G. Groppi, "Effect of alternate CH4-reducing/lean combustion treatments on the reactivity of fresh and S-poisoned Pd/CeO2/Al2O3 catalysts," *Appl Catal B*, vol. 80, no. 3–4, pp. 335–342, 2008, doi: 10.1016/j.apcatb.2007.11.030.

[120] P. Castellazzi, G. Groppi, P. Forzatti, E. Finocchio, and G. Busca, "Activation process of Pd/Al2O3 catalysts for CH 4 combustion by reduction/oxidation cycles in CH4- containing atmosphere," *J Catal*, vol. 275, no. 2, pp. 218–227, 2010, doi: 10.1016/j.jcat.2010.07.028.

[121] C. F. Cullis, T. G. Nevell, and D. L. Trimm, "Role of the catalyst support in the oxidation of methane over palladium," *Journal of the Chemical Society, Faraday Transactions 1: Physical Chemistry in Condensed Phases*, vol. 68, pp. 1406–1412, 1972, doi: 10.1039/F19726801406.

[122] R. S. Monteiro, D. Zemlyanov, J. M. Storey, and F. H. Ribeiro, "Surface area increase on Pd foils after oxidation in excess methane," *J Catal*, vol. 201, no. 1, pp. 37–45, 2001, doi: 10.1006/jcat.2001.3235.

[123] A. Baylet, P. Marécot, D. Duprez, P. Castellazzi, G. Groppi, and P. Forzatti, "In situ Raman and in situ XRD analysis of PdO reduction and Pd° oxidation supported on γ-Al2O3 catalyst under different atmospheres," *Physical Chemistry Chemical Physics*, vol. 13, no. 10, pp. 4607–4613, Mar. 2011, doi: 10.1039/c0cp01331e.

[124] J. B. Miller and M. Malatpure, "Pd catalysts for total oxidation of methane: Support effects," *Appl Catal A Gen*, vol. 495, pp. 54–62, Apr. 2015, doi: 10.1016/j.apcata.2015.01.044.

[125] D. Wang *et al.*, "Distinct reaction pathways of methane oxidation on different oxidation states over Pd-based three-way catalyst (TWC)," *Appl Catal A Gen*, vol. 572, no. August 2018, pp. 44–50, 2019, doi: 10.1016/j.apcata.2018.12.022.

[126] R. E. Hayes, S. T. Kolaczkowski, P. K. C. Li, and S. Awdry, "The palladium catalysed oxidation of methane: Reaction kinetics and the effect of diffusion barriers," *Chem Eng Sci*, vol. 56, no. 16, pp. 4815–4835, 2001, doi: 10.1016/S0009-2509(01)00131-2.

[127] D. Ciuparu and L. Pfefferle, "Contributions of lattice oxygen to the overall oxygen balance during methane combustion over PdO-based catalysts," *Catal Today*, vol. 77, no. 3, pp. 167–179, 2002, doi: 10.1016/S0920-5861(02)00243-2.

[128] Y. H. C. Chin, M. García-Diéguez, and E. Iglesia, "Dynamics and thermodynamics of Pd-PdO phase transitions: Effects of pd cluster size and kinetic implications for catalytic methane combustion," *Journal of Physical Chemistry C*, vol. 120, no. 3, pp. 1446–1460, 2016, doi: 10.1021/acs.jpcc.5b06677.

[129] J. D. Grunwaldt, N. Van Vegten, and A. Baiker, "Insight into the structure of supported palladium catalysts during the total oxidation of methane," *Chemical Communications*, no. 44, pp. 4635–4637, 2007, doi: 10.1039/b710222d.

[130] S. K. Matam, M. H. Aguirre, A. Weidenkaff, and D. Ferri, "Revisiting the problem of active sites for methane combustion on Pd/Al 2O3 by operando XANES in a lab-scale fixed-bed reactor," *Journal of Physical Chemistry C*, vol. 114, no. 20, pp. 9439–9443, May 2010, doi: 10.1021/jp1019697.

[131] H. Stotz, L. Maier, and O. Deutschmann, "Methane Oxidation over Palladium: On the Mechanism in Fuel-Rich Mixtures at High Temperatures," *Top Catal*, vol. 60, no. 1–2, pp. 83–109, Feb. 2017, doi: 10.1007/s11244-016-0717-5.

[132] H. Stotz, L. Maier, A. Boubnov, A. T. Gremminger, J. D. Grunwaldt, and O. Deutschmann, "Surface reaction kinetics of methane oxidation over PdO," *J Catal*, vol. 370, pp. 152–175, Feb. 2019, doi: 10.1016/j.jcat.2018.12.007.

[133] O. Deutschmann *et al.*, "DETCHEM Software package, 2.9 ed., www.detchem.com, Karlsruhe 2022."

[134] P. Castellazzi, G. Groppi, P. Forzatti, A. Baylet, P. Marécot, and D. Duprez, "Role of Pd loading and dispersion on redox behaviour and CH4 combustion activity of Al2O3 supported catalysts," *Catal Today*, vol. 155, no. 1–2, pp. 18–26, 2010, doi: 10.1016/j.cattod.2009.02.029.